Title
An Experimental Based Investigation of Oxycombustion in an SI Engine

Author
Van Blarigan, Andrew Charles

Publication Date
2012

Peer reviewed|Thesis/dissertation

An Experimental Based Investigation of Oxycombustion in an SI Engine

by

Andrew Charles Van Blarigan

A dissertation submitted in partial satisfaction of the
requirements for the degree of
Doctor of Philosophy

in

Engineering - Mechanical Engineering

in the

Graduate Division

of the

University of California, Berkeley

Committee in charge:

Professor Robert W. Dibble, Chair
Professor J.Y. Chen
Professor Stephen Derenzo

Fall 2012

An Experimental Based Investigation of Oxycombustion in an SI Engine

Abstract

An Experimental Based Investigation of Oxycombustion in an SI Engine

by

Andrew Charles Van Blarigan

Doctor of Philosophy in Engineering - Mechanical Engineering

University of California, Berkeley

Professor Robert W. Dibble, Chair

This dissertation represents the culmination of research performed investigating oxycombustion in a spark-ignited (SI), piston engine. Oxycombustion is the process in which nearly pure oxygen and fuel are burned in a diluent of exhaust gas which is recirculated from the exhaust to the intake, referred to as exhaust gas recirculation (EGR). In typical air burning engines, EGR is used to reduce combustion temperatures, thereby reducing the formation of the pollutant nitric oxides (NO_x). Under standard conditions the inclusion of EGR leads to a decreased thermal efficiency due to the lower ratio of specific heat of EGR relative to air, but the penalty is necessary in order to comply with stringent emission regulations. Conversely, the motivation for power generation using oxycombustion with EGR is the ease with which carbon dioxide (CO_2) can be isolated in the exhaust for sequestration through a carbon capture and sequestration (CCS) process. The EGR is necessary in oxycombustion processes for temperature control, but the primary motivation is preventing engine damage from excessively high heat rather than reducing NO_x production. At similar operating points the negative effect of EGR on the thermal efficiency of traditional air engines is magnified in oxycombustion due to the very high EGR levels. Therefore, it is the objective of this study to determine where the operating limits can be extended beyond the normal limits of air systems, regaining lost thermal efficiency. No other experimental research could be found in the literature which operated an internal combustion (IC) engine or a turbine under oxycombustion conditions using EGR diluent, thus this work represents a pioneering effort towards experimentally determining the properties of oxycombustion with EGR working fluid in a compression based power generating system.

As the effects of global climate change become more apparent, there is a pressing need for a reduction in the quantity of CO_2 emissions released into the atmosphere. An ideal solution would be the reduction and eventual elimination of CO_2 production, but such a solution is very challenging and will likely occur slowly over a long period of time. In the short term, a potential alternative is the use of CCS, in which CO_2 is captured and stored rather than released into the atmosphere. Oxycombustion represents one viable method of producing highly concentrated CO_2 which can be easily capture and stored.

Oxycombustion has been widely studied theoretically, and many experimental studies have been performed related to the laminar flame speed and ignition properties, but no publications could be found in which a compression-based power generation system was operated under oxycombustion conditions. The work presented in this thesis originated from funding provided to determine the effect of N_2 concentration on NO_x formation under methane fueled oxycombustion conditions. With the experimental apparatus built and working properly it was possible to study a wide range of properties relating to oxycombustion in an SI engine.

Experiments were carried out a single-cylinder, variable compression ratio CFR engine on which the intake and exhaust systems were redesigned to include a large, steady-state EGR loop. The redesigned system included the ability to operate with true EGR, referred to as 'wet EGR' due to the high water concentration which is not condensed out, with CO_2, referred to as 'dry EGR' since it represents the remained of an EGR stream which has the water condensed out, and with air. The setup provided the ability to vary a large number of parameters, including the working fluid, N_2 concentration, compression ratio, spark-timing, oxygen concentration, intake temperature, and fuel.

Both EGR working fluids are composed of almost entirely CO_2 and water, which are both triatomic species. As such, EGR working fluid has a much higher specific heat and much lower ratio of specific heats than air in addition to negative chemical effects. Predicted laminar flame speeds dropped by a factor of 2 in wet EGR while dry EGR showed a decrease by more than a factor of 4 relative to methane-in-air. The significantly higher laminar flame speeds in wet EGR when compared to dry EGR were found to be the product of water displacing CO_2 from a chemical standpoint, since CO_2 has significant negative chemical iterations where as water is relatively inert, and a thermal standpoint, since water has significantly higher thermal diffusivity than CO_2. Despite the superior properties of the wet EGR working fluid, dry EGR produced superior thermal efficiency for all fuels tested.

Dry EGR has been found to have significantly higher knock resistance than air, allowing operation at higher compression ratios (CR) which can ultimately produce higher thermal efficiencies than air operation when combusting a low octane fuel. In fact, dry EGR produced higher thermal efficiencies when operating with heptane fuel (which has very poor knock resistance) than it did with methane fuel (which has a very high knock resistance). The primary reason for this anomaly was determined to be minor autoignition events, which significantly decrease combustion duration but do not produce significant knock, occurring with the low octane fuel. Under low oxygen concentrations and high compression ratios these minor autoignition events are common enough to result in a significant shortening of the average combustion duration, thus increasing the thermal efficiency in a situation where slow flame propagation would normally prevent a strong combustion event. With methane, which was not knock limited due to the knock resistance of the fuel, no such autoignition events occurred. In order to overcome the lack of autoignition events the oxygen concentration had to be increased to develop strong combustion. Therefore, when operation is limited by engine configuration rather than knocking, as with methane, the performance of dry EGR is very low relative to air, roughly proportional to the decrease in theoretical thermal efficiency due to the decrease in the ratio of specific heats. In order to take advantage of the

improved knock resistance it is necessary to operate in a region with a high enough CR and low enough oxygen concentration that minor autoignition events are common. With high enough CR, such combustion could be possible even with fuels such as methane, allowing dry EGR to produce higher thermal efficeincy than methane-in-air. However, the very high autoignition temperature of methane would require very high in-cylinder temperatures which would produce significant wall and exhaust heat losses. The minimum oxygen concentration is limited by the end of combustion heat release (HR) profile, which becomes increasingly elongated as the oxygen concentration is reduced. Therefore, it is likely that if a high enough CR could be reached a local maximum thermal efficiency with respect to oxygen concentration would exist regardless of the fuel.

Wet EGR produces similar trends as dry EGR, but cannot attain the high CRs which dry EGR operated at due to the elevated intake temperature required to prevent water condensation. Ultimately, despite the chemical and thermal advantages of water compared to CO_2 in regards to laminar flame speeds, wet EGR is not a reasonable choice when operating in an IC engine. Despite its limitations in an IC engine, wet EGR has several advantages which should be carefully considered in applications where high initial temperatures are not propagated negatively.

Contents

List of Figures

List of Tables

List of Notations

α	Thermal diffusivity
η	Efficiency
γ	Ratio of specific heats
C_p	Specific heat
$S/subL$	Laminar Flame Speed
$S/subT$	Turbulent Flame Speed
ATDC	After Top Dead Center
BMEP	Brake Mean Effective Pressure
BTDC	Before Top Dead Center
CAD	Crank Angle Degree
CCS	Carbon Capture and Sequestration
CFR	Cooperative Fuel Research
CoV IMEP	Coefficient of Variation of Indicated Mean Effective Pressure
CR	Compression Ratio
EGR	Exhaust Gas Recirculation
GCF	Gas Correction Factor
HC	Hydrocarbon
HCCI	Homogeneous Charge Compression Ignition
HR	Heat Release
HRR	Heat Release Rate

IC	Internal Combustion
ICRC	Internal Combustion Rankine Cycle
ID	Inner Diameter
IMEP	Indicated Mean Effective Pressure
IMPO	Integral of Modulus of Pressure Oscillation
LPM	Liters Per Minute
MAPO	Maximum Amplitude of Pressure Oscillation
PID	Proportional Integral Derivative
PT	Pressure Transducer
ROHR	Rate of Heat Release
RPM	Rotations Per Minute
SCAQM	South Coast Air Quality Management
SI	Spark Ignition
ST	Spark-Timing
TC	Thermocouple
TDC	Top Dead Center
TFMEP	Total Friction Mean Effective Pressure
THC	Total Hydrocarbons

Acknowledgments

I am eternally grateful to all of my family whose unwavering support made this dissertation possible. Thank you Erin, for all the love, for your understanding, and for all the delicious meals. This dissertation would not have been possible without my parents, who provided my upbringing, giving me a strong foundation, and for their unconditional love. I owe my deepest gratitude to my Grandma, who was always my biggest supporter, and to my Grandpa, who has captured all of my accomplishments on film. I am grateful to my Aunt Sue and Uncle Jim for their generosity, providing me with housing for many years during my studies. And I would like to thank my siblings, whom I have always been able to count on for distractions.

I am indebted to many advisors, mentors, and managers who have supported me during my time. It is an honor for me to thank my head advisor Professor Robert Dibble, who guided me through my PhD. I am grateful to Professor J.Y. Chen who also provided invaluable guidance and advice, and to Professor Stephen Derenzo who read this dissertation and provided valuable feedback. This thesis would not have been possible without the help of Professor Robert Cattolic and Dr. Reinhard Seiser, or the book-keeping genius of MaryAnne Peters. I would like to thank Sandia National Labs for the support and guidance of their staff, including Nicholas Paradiso, my mentor, and Chuck Cadden, who identified my potential and helped support me.

I would like to show my gratitude to my colleagues who have made the last five years enjoyable in spite of everything. I am grateful to Darko Corazak who spent countless hours helping me run the engine and analyze codes, but who always made time for a beer. I would like to thank Philipp Tschann and Wolfgang Hable for all the good times and for the tireless work they put in to refining and improving the engine. It has been an honor to work with Andrew North, with whom I have shared many animated technical discussions. It was my pleasure to study alongside Alex Green, who always encouraged me to get outside. I owe my deepest gratitude to Vi Rapp, Samveg Saxena, Anthony DeFilippo, Ben Wolk, and Bryan Boyce for all of their help and guidance through the years.

Chapter 1

Introduction and Background

This thesis represents the culmination of research performed investigating oxycombustion in a spark-ignited (SI), piston engine. Oxycombustion is the process in which nearly pure oxygen and fuel are burned in a diluent of exhaust gas which is recirculated from the exhaust to the intake, referred to as exhaust gas recirculation (EGR).

In typical air burning engines, EGR is used to reduce combustion temperatures, thereby reducing the formation of the pollutant nitric oxides (NO_x). Under standard conditions the inclusion of EGR leads to a decreased thermal efficiency due to the lower ratio of specific heat of EGR relative to air, but the penalty is necessary in order to comply with stringent emission regulations. The use of EGR as an emission control device in air engines has been widely studied, with massive numbers of papers and reviews on the subject. EGR was first adopted in diesel engines, which utilize non-premixed combustion and therefore have very high combustion temperatures which produce large quantities of NO_x. The addition of EGR to the diesel combustion chamber increases the specific heat of the mixture, thereby decreasing combustion temperatures. Since diesels do no operate with a stoichiometric mixture, but rather meter only the fuel and combust lean, the impact of adding EGR can be gained throughout all operating regions, but all cases are subject to the penalty of reduced thermal efficiency due to the low ratio of specific heat of EGR.

At present time, SI engines operate almost exclusively with a stoichiometric air-fuel mixture. The reason for the stoimetric condition is largely emissions based; it is not possible to spark-ignite a premixed, homogeneous charge engine running on traditional fuels at low enough equivalence ratios to prevent the formation of NO_x, making it necessary to preform after-treatment to remove the pollutants. The most cost-effective and reliable form of exhaust gas after-treatment is the three-way catalyst which requires a stoichiometric exhaust composition to react NO_x. Since SI engines typically cannot operate at conditions which do not produce NO_x, and the three way catalyst requires stoichiometric conditions to be effective, the vast majority of all SI engines run exclusively at a stoichiometric point. With the exhaust after-treatment systems of stoichiometric SI engines, controlling the initial quantity of NO_x formation is therefore not as critical and thus there is no need to accept the penalty of including EGR. However, at low loads, when the engine must throttle the intake air to

reduce the quantity of oxygen, and accordingly reduce the fuel, the throttling losses can be significant. In such situations the additional of EGR can actually help improve the engine performance while reducing NO_x, but the effect is very minor (Wei et al. 2012).

Conversely, the motivation for power generation using oxycombustion with EGR is the ease with which carbon dioxide (CO_2) can be isolated in the exhaust for sequestration through a carbon capture and sequestration (CCS) process. The EGR is necessary in oxycombustion processes for temperature control, but the primary motivation is preventing engine damage from excessively high heat rather than reducing NO_x production. Since in an oxycombustion system both the oxygen and the fuel are paid for (as opposed to a fuel and air system, in which the air is free) it is not logical to operate under any condition other than stoichiometric, which takes full advantage of both the air and the fuel. Diesel cycles, which operate under lean conditions, would waste the expensive oxygen which had to be extracted from the air, and therefore are not a practical solution for oxycombustion. Therefore, a spark-ignited system operating under stoichiometric conditions is the most feasible.

The drawback of any oxycombustion system is that when compared to a traditional air system at similar operating points the negative effect of the low ratio of specific heats of EGR on the thermal efficiency is magnified in oxycombustion due to the very high EGR levels. Therefore, it is the objective of this study to determine where the operating limits can be extended beyond the normal limits of air systems, regaining lost thermal efficiency. No other experimental research could be found in the literature which operated an internal combustion (IC) engine or a turbine under oxycombustion conditions using EGR diluent, thus this work represents a pioneering effort towards experimentally determining the properties of oxycombustion with EGR working fluid in a compression based power generating system.

1.1 Background

Atmospheric CO_2 has been increasing for centuries, and has been strongly correlated to the increasing global temperature. An excerpt from the AR4 IPCC Report 2007 states "There is now very high confidence that the globally averaged net effect of human activities on climate since 1750 has been warming primarily due to emissions from fossil fuel consumption, agriculture and land-use changes." Additionally, the report specifies that the current levels of greenhouse gas in the atmosphere exceed by far the natural range over the last 650,000 years, and that if greenhouse gas emissions are not reduced, an increase of 0.2°C per decade over the next 30 years is *very likely*. The report predicts that continued greenhouse gas emissions at or above current rates would cause further warming of the Earth and induce changes in the global climate system during the 21st century that would *very likely* be greater than those observed during the 20th century. These realizations are not new; similar correlations between CO_2 increase, temperature increase, and human influence have been noted by the IPCC in reports from 2001 and 1995. In fact, Revelle published a paper over 50 years ago identifying the possible buildup of significant CO_2 in the atmosphere due to exponentially increasing fuel combustion (Revelle and Suess 1957).

The reason for the detrimental effect of greenhouse gases in the atmosphere is primarily in the increased radiative forcing, as shown in Fig. 1.1 from the IPCC 2007 Synthesis Report. It is clear that anthropogenic components are dominate, and that CO_2 is the single largest component, with almost double the radiative force as any other component.

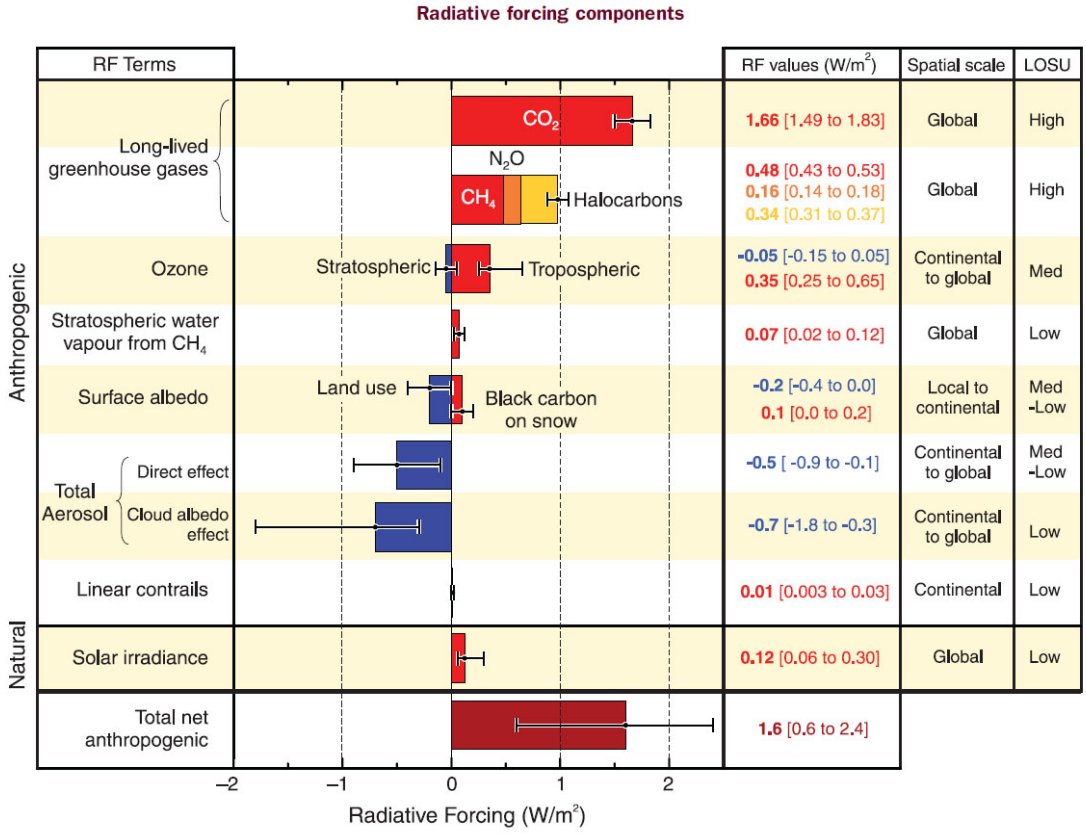

Figure 1.1: Global average radiative forcing (RF) in 2005 (best estimates and 5 to 95% uncertainty ranges) with respect to 1750 for CO_2, CH_4, N_2O and other important agents and mechanisms, together with the typical geographical extent (spatial scale) of the forcing and the assessed level of scientific understanding (LOSU). Aerosols from explosive volcanic eruptions contribute an additional episodic cooling term for a few years following an eruption. The range for linear contrails does not include other possible effects of aviation on cloudiness [AR4 IPCC Report 2007].

Current investigations and predictions related to the emissions of CO_2 have painted a bleak outlook. Solomon predicts that even if CO_2 emissions drop to zero, it will take 1000 years to return to a normal state, as shown in Fig. 1.2 (Solomon et al. 2009). This trend is in agreement with the work presented by Matthews, which shows that CO_2 emissions need to be completely stopped to achieve a stable global temperature (Matthews and Caldeira

2008). Matthew further notes that any future anthropogenic emissions of greenhouse gases will commit the climate system to warming that is essentially irreversible on centennial timescales.

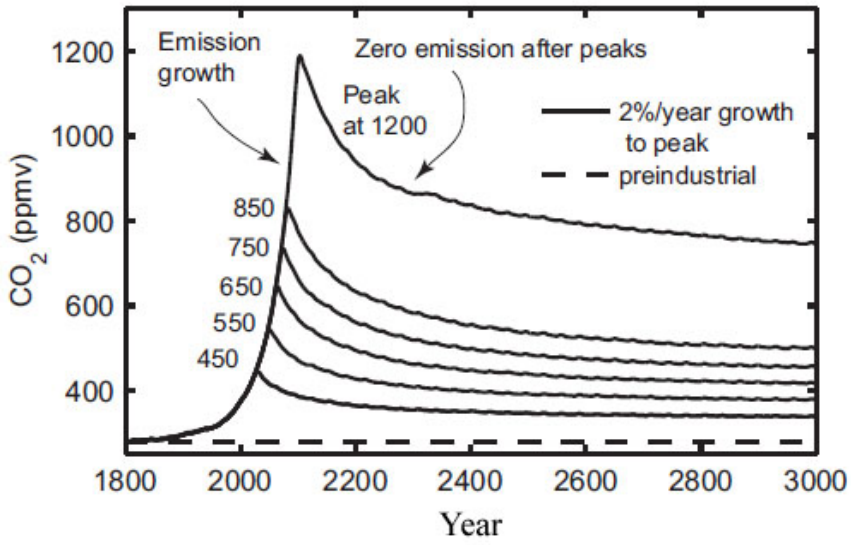

Figure 1.2: Falloff of CO_2 concentrations following zero emissions after the peak (Solomon et al. 2009).

Schmittner has presented simulation results extending out the the year 4000 AD with CO_2 emissions following business-as-usual trends. His results indicate that in this scenario the earth would be subject to an approximate increase in global surface temperatures of 10°C, and a reduction of sea ice to only 10% of its current coverage (Schmittner et al. 2008).

It is easy to conclude that continuing on with business-as-usual is not an acceptable option, and even maintaining current CO_2 emission levels will have a devastating effect on future generations for centuries. CO_2 history and predictions, based on a reference scenario taking policy through 2008 into account, from the International Energy Agency (IEA), indicate that CO_2 levels will continue to increase significantly (Fig. 1.3 (IEA 2008)). IEA predicts the CO_2 level increase will be largely due to non-OECD (Organization for Economic Co-operation and Development) countries, while member countries will maintain current levels, but no significant decrease in CO_2 emissions is predicted for any sector.

Fossil fuels currently supply more than 85% of the energy used worldwide, and are the main cause for the increased concentration of greenhouse gases in the atmosphere (Quintella et al. 2011). Renewable energy sources are the focus of great attention, but IEA predictions indicate that they will continue to represent only a small portion of the total energy production for many decades to come (Fig. 1.4). For the foreseeable future, it will be necessary to

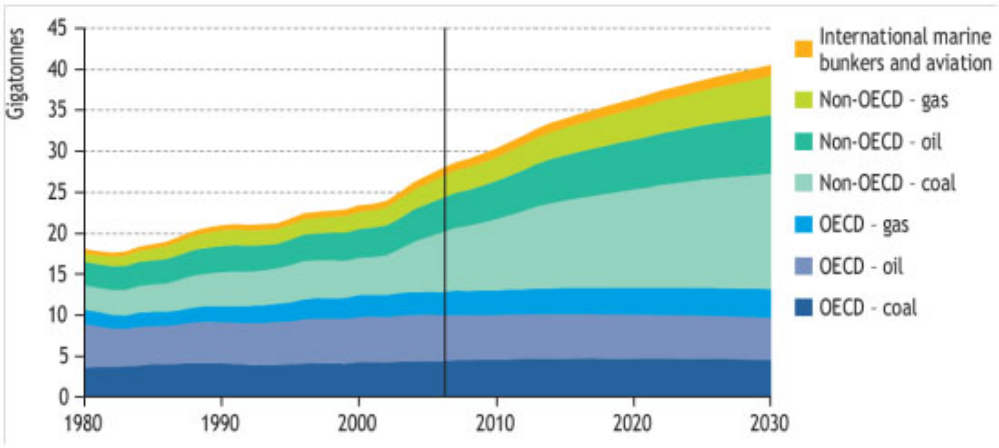

Figure 1.3: Energy-related CO_2 emissions in the Reference Scenario by fuel and region (IEA 2008).

curb CO_2 emissions from all sources of power generation, with one viable component being carbon capture and sequestration (CCS).

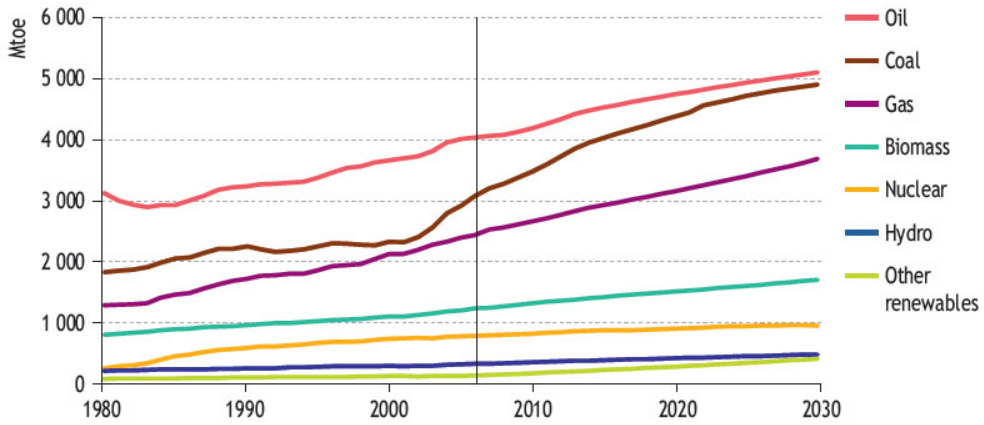

Figure 1.4: World primary energy demand by fuel in the Reference Scenario (IEA 2008).

CCS is a rapidly growing field, as an increasing portion of the world's population recognize the importance of reducing CO_2 emissions. As a general indicator of the growth of the field, Quintella et al. (2011), have compiled an overview of carbon capture patents applied for and articles published. They found a clear increase in the activity of both articles published and patents applied for across all capture technologies, shown in Fig. 1.5 (Quintella et al. 2011).

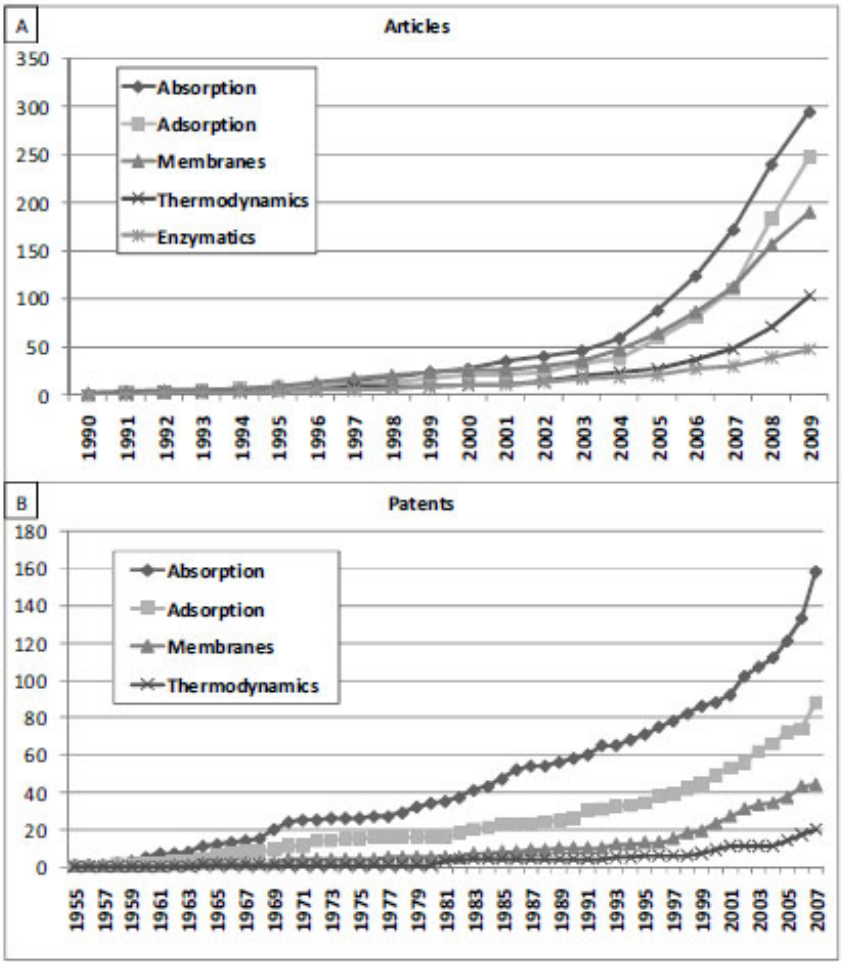

Figure 1.5: Cumulative annual evolution of each capture method for: (A) articles published indexed in Web of Science I. S. I. journals; (B) patent applications. (Quintella et al. 2011)

1.2 Carbon Capture and Sequestration

The capturing of carbon can occur post combustion with membranes, solvents, or liquefaction, or prior to combustion via reforming of hydrocarbons into hydrogen (H_2) and removing carbon dioxide (CO_2) (Metz et al. 2005; Damen et al. 2006). The potential of CO_2 capture has been studied for a variety of power cycles, including gas turbines (Sanz et al. 2008), coal combustion (Scheffknecht et al. 2011), and internal combustion engines (Bilger and Wu 2009). The main focus of carbon capture has been combustion systems in the energy sector, but has also expanded into other sectors such as steel and concrete production (Gielen 2003; Flower and Sanjayan 2007). For all cases, once CO_2 is isolated it can be sequestered in the ocean or deep saline aquifers (Heddle, Herzog, and Klett 2003). A flow chart of the different

approaches which can be undertaken is shown in Fig. 1.6.

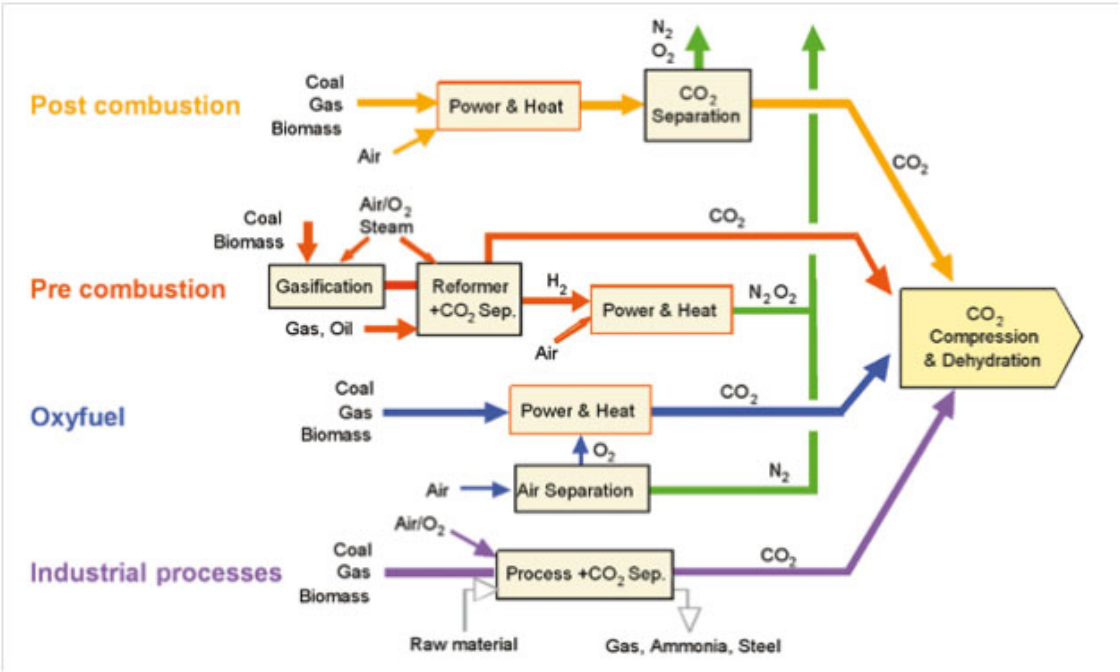

Figure 1.6: A flow chart presenting the techniques available for carbon capture, and at what step in the process they occur.

Oxycombustion, which burns fuel with pure oxygen (O_2) in a diluent of CO_2, water (H_2O), or a combination of the two, is one promising approach to post-combustion carbon capture (Metz et al. 2005; Kanniche et al. 2010).

Carbon Sequestration

Before analyzing the methods of carbon capture, it is logical to investigate and understand the plausibility of sequestering the product. Currently, there exists two main locations for sequestering large quantities of CO_2: 1) burying it in geological reservoirs, and 2) pumping it deep into the ocean (Metz et al. 2005). The different approaches to using both of these techniques will be described in this section.

Geological Reservoirs

When CO_2 is buried at depths below 800m it becomes supercritical and has a liquid-like density that provides the potential for efficient utilization of underground storage space and improves storage security. The result is appropriate saline formations or oil or gas fields are very effective and reliable when they are deep enough. Oil companies could take advantage of

this form of storage by using CO_2 when performing Enhanced Oil Recovery (in which gas is pumped into oil fields to increase the pressure of the reserve and force out more oil) without adding significantly to their costs. An additional form of storage can occur at shallower depths in coal beds. However, this technology is dependent on the absorption of the CO_2 onto the coal, and therefore is strongly a function of the permeability of the coal bed. (Metz et al. 2005)

Ocean Sequestration

There are two main approaches to sequestering CO_2 in the ocean: 1) dissolution, in which the CO_2 disperses into the water and equilibrates, and 2) lake type, where the CO_2 is pooled at a local minimum deep underwater.

Dissolution can occur below 1000m, with the concept being to disperse the CO_2 to the point that it can dissolve into the water. One method of dispersion uses gaseous CO_2 injected deep underwater, creating a 'rising plume' which disperses as it rises and is absorbed prior to reaching the surface. An alternative but similar method is the 'sinking plume' in which liquid CO_2 is injected deep underwater and sinks, thus dispersing. Either method can occur from a fixed pipeline, or from a pipe trailing below a ship which moves as it deposits the CO_2 to enhance the dispersion. (Metz et al. 2005)

Lake type sequestration must occur below 3000m, where the density of the liquid CO_2 is greater than the density of water. Because of the difference in density, if the CO_2 is deposited at a local minimum it will pool and remain relatively stable. Any CO_2 which is moved from the surface due to strong currents should sink and pool elsewhere, or be absorbed into the water. (Metz et al. 2005)

Carbon Capture - Literature Review

A significant amount of research has been conducted on a variety of carbon capture methods and applications. An extensive literature review, including over 100 publications, evaluating the economic feasibility of promising conversion and capture technologies including post-combustion capture, pre-combustion capture, and oxycombustion was produced by Damen et al. (2006). The work evaluates coal and natural gas power systems, based on net efficiency, energy production costs, and CO_2 collection efficiency. In general, the majority of oxycombustion research has been focused on coal power plants, as well as significant theoretical work and some experimental work on turbine oxycombustion. Little work has been performed investigating oxycombustion in a stationary engine, but a few publications were found.

An Overview - Comparison of Technologies

In their investigation of coal fired plants, looking at post-combustion capture and oxycombustion, Damen et al. (2006) found that the two technologies resulted in similar thermal

Table 1.1: Key parameters of PC plants (using bituminous coal) with CO_2 capture from literature review.

CO_2 capture technology	Net electric efficiency (%)	Efficiency penalty (% points)	CO_2 capture efficiency (%)	TCR (Euro/kWe)
Post-combustion (amines)	30-35	8-13	85-90	1720-2490
Oxycombustion (ASU)	33-36	9-12	90-100	1830-2220

efficiency decreases, but oxycombustion techniques were able to capture 90-100% of the CO_2, while post-combustion techniques were limited to 85-90% capture. The leading technology in post-combustion capture was determined to be chemical absorption of the CO_2 using monoethanoloamine (MEA), which is suitable for low CO_2 partial pressures. For this technique it is necessary to remove NO_x and SOx to very low levels, as these components form heat stable salts and thus poison the system over time. The pumping of the CO_2 is accomplished by allowing the CO_2 to react chemically with the amine in the absorption column, and then releasing the CO_2 in the desorber by heating the substrate to 120°C. This heating process is achieved through the use of some of the systems steam, which is the major bottleneck of the technology. Alternative post-combustion capture techniques such as adsorption, low temperature distillation, and membranes are also considered but all have shortcomings and are currently not as viable as MEA. The energy requirements of conventional pressure (and temperature) swing physical adsorption, in which CO_2 binds to a solid surface were found to be prohibitively large.

Coal oxycombustion was considered with (nearly) pure oxygen produced by a cryogenic air separation unit (ASU). New separation technologies such as ion transport membranes (ITM) are also mentioned, but are reported as 'being worked on.' The major advantages found with oxycombustion is the possibility to capture nearly 100% of the CO_2, and the ability to avoid expensive selective catalytic reduction (SCR) and flue gas desulphurisation (FGD) units. It is suggested that NO_x and SO_2 in the gas could possibly be left in the CO_2 for co-storage, or easily separated during the distillation process.

Overall, the authors note that the technologies have similar consequences on efficiency, and cite several papers which make various claims on the issue. The ultimate conclusion drawn is that it is unclear whether oxycombustion proves to be a more cost-effective capture option than post-combustion strategies, and therefore both technologies should be further explored (Table 1.1).

In their investigation of natural gas combined cycle (NGCC) plants, Damen et al. (2006) considered post-combustion capture, pre-combustion capture, and oxycombustion. Post-combustion capture again found that MEA was the preferred technology due to the low CO_2 concentration in the flue gases. Pre-combustion capture considered syngas production by reforming and/or partial oxidation of natural gas, subsequent water gas shift, separation of

Table 1.2: Key parameters of natural gas-fired power plants with CO_2 capture from literature review

Conversion technology	CO_2 capture technology	Net electric efficiency (%)	Efficiency penalty (% points)	CO_2 capture efficiency (%)
Post-combustion capture				
NGCC (F-class)	Chemical absorption	43-50	6-12	85-90
NGCC (G/H--class)	Chemical absorption	48-53	5-11	85-90
NGCC 2020	Improved chemical absorption	55	6	85
Pre-combustion capture				
SMR/POX/ ATR-CC	Chemical/physical absorption	43-50	8-13	85-90
ATR-CC	SEWGS	47-48	9-10	90
MR-CC	Hydrogen membrane	51-53	5-6	100
Oxyfuel combustion				
Graz cycle	ASU	39-45	13-19	100
Water cycle	ASU	40-62	10-13	100
Oxyfuel (Matiant) CC	ASU	44-48	11-13	90-100
AZEP	Oxygen membrane	50-55	2-8	85-100
CLC-CC+CO_2 turbine	Oxygen carrier	51-54	3-5	100
CLC-CC	Oxygen carrier	50-53	3-5	50-100

CO_2 and hydrogen by physical or chemical absorption and combustion of hydrogen in a gas turbine. The authors cite increased NO_x emissions as one of the disadvantages of burning hydrogen in a turbine, but note that the hydrogen stream can be diluted with nitrogen, resolving the issue with no significant loss of efficiency. SCR is suggested as an alternative, but the cost associated with such a unit are considered too high. NGCC oxycombustion using an ASU to produce pure oxygen was investigated for a range of technologies. Due to the nature of turbines, it is necessary to design new combustors and compressors for the CO_2 working fluid, which has an optimal pressure ratio higher than for conventional air turbines. This re-design has resulted in numerous technologies being explored, with various working fluid combinations, turbine designs, and separation techniques. In addition to ASU oxycombustion units, oxygen membrane and oxygen carrier units are considered, and found to promising technologies. However, the concepts are still in early development and are therefore hard to analyze precisely. In conclusion, a wide range of efficiency penalties and CO_2 capture efficiencies were measured, with overlap and uncertainties too large to draw any strong conclusions about which technologies are them most promising (Table 1.2).

In a more recent publication, Kanniche et al. (2010) compares NGCC, pulverized coal power plant (PC), and Integrated Gasification Combined Cycle (IGCC) utilizing pre-combustion, post-combustion, or oxycombustion. For post-combustion capture Kanniche also identifies

MEA as the most practical technology for the near future, though methyldiethenolamine (MDEA) is identified as a better option when the partial pressure of the CO_2 is slightly higher. When considering oxycombustion, the need for high purity CO_2 is noted as the presence of incondensable gases in the CO_2 flow transported by pipeline in the supercritical state can cause vibrations and shock loads in the pipe, which can cause mechanical damage. However, no study was reported which has attempted to specify critical concentrations of these incondensable gases. Kanniche states that all that is agreed upon unanimously is the concentration of water, and most works published on this subject agree upon a fixed limit of 20 ppm by mass (50 ppm by volume). Thus, Kanniche utilized a dehydration system using triethylene glycol (TEG) followed by a cryogenic impurity separation device integrated into the CO_2 compression/liquefaction step. The comparison between the difference technologies, shown in Fig. 1.7, is similar to the results gathered by Damen.

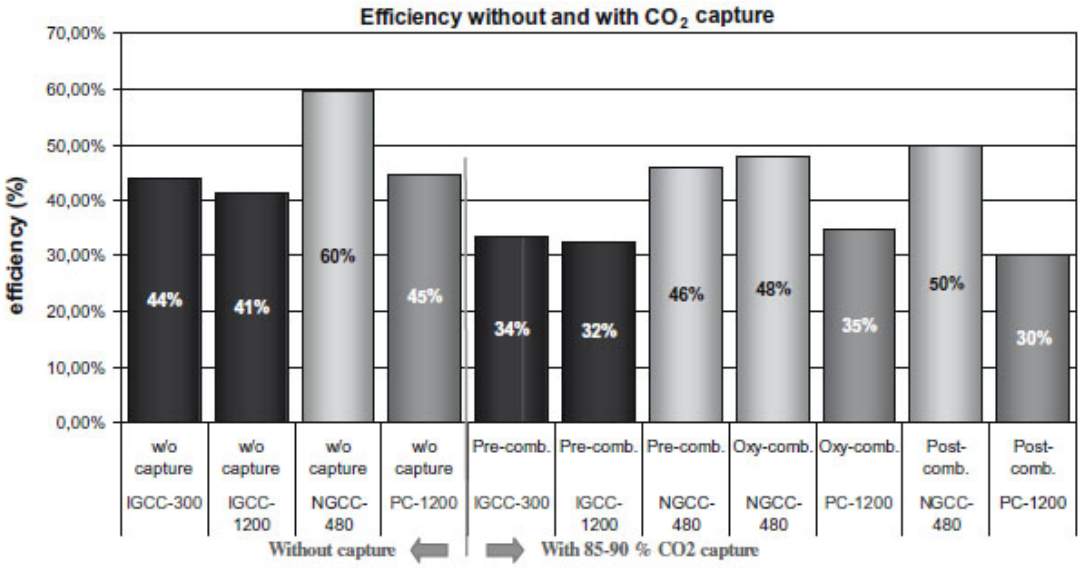

Figure 1.7: Efficiency of the different systems with and without CO_2 capture (Kanniche et al. 2010).

In conclusion, all of the major approaches to carbon capture, including pre-combustion, post-combustion, and oxycombustion, have strengths and weaknesses. Oxycombustion is a technology which is competitive with other carbon capture approaches, and warrants additional research. Though an SI piston engine is not a conventional approach to oxycombustion or electrical power generation, it represents an opportunity to better understand technology, and characterize the performance in a fully functional experiment.

Flame Speeds in CO_2 and H_2O Working Fluid

Many studies have focused on the effect of CO_2 and H_2O on laminar flame speeds, though most are focused on low concentrations of both species in relation to N_2. There is general agreement in the literature that the laminar flame speed of methane in a CO_2 diluent is significantly reduced relative to methane-in-air flame speeds, and that this decrease is a function of both thermal and chemical effects. When water is used as a diluent the flame speed is higher than CO_2 diluents, and the chemical interactions appear to be small, with the exception of a positive chemical effect when combusting fuels with high CO content (such as syngas).

Das, Kumar, and Sung (2011) investigated the laminar flame speed of moist syngas mixtures using a counterflow burner apparatus and a DPIV system. Das found that including water in the fuel mixture actually increased flame speed due to a positive chemical effect. This positive association between water concentration and flame speed ended at a local maximum of roughly 20% water by volume. At this point it was determined that the positive chemical effects of water were dominated by the negative thermal effects.

Richards, Casleton, and Chorpening (2005) investigated the effect of using CO_2 vs. H_2O working fluid for a turbine operating on natural gas under oxycombustion conditions for zero-emission power. The work used a stirred and plug flow reactor network to compare the residence time requirements for combustors using CO_2 versus H_2O diluent. It was found that H_2O was the superior working fluid, with the required residence time being 5-7 times less than when CO_2 was the diluent. A numerical study, with the process being modeled as a PSR, predicted a similar difference in residence time. For both experiment and simulation, the equilibrium CO levels for the CO_2 diluted cycle were higher compared with the H_2O diluted cycle, though both were reasonably low.

Zhu, Egolfopoulos, and Law (1989) experimentally measured the laminar flame speed of mixtures of CO_2, O_2, N_2, and Ar. The experiment involved the establishment of two symmetrical, planar, nearly-adiabatic flames in a nozzle-generated counterflow, and the determination of the axial velocity profile along the centerline of the flow by using laser Doppler velocimetry. Figure 1.8 shows the traditional plot of flame speed S_L^0 versus equivalence ratio (ϕ) for methane/Ar-air, methane/N_2-air, and methane/CO_2-air mixtures at 1 atm pressure. The symbol I-air here, as in Ar-air, designates an air mixture in which all the N_2 has been substituted by Ar.

Liu, Guo, and Smallwood (2003) have performed numerical simulations of the laminar flame speed with CO_2 working fluid based on the data presented by Zhu, Egolfopoulos, and Law (1989) (Fig. 1.8). Liu identifies three mechanisms through which the burning velocity may be affected: i) the variation of the transport and thermal properties of the mixture, ii) the possible direct chemical effect of CO_2, and iii) the enhanced radiation transfer by CO_2. Liu utilized the GRI 3.0 mechanism and was able to closely match the results of Zhu. In addition, Liu ran calculations using chemically inert CO_2 and showed that the flame speed is significantly higher than when chemically active CO_2 is used. A single reaction was isolated as being one of the significant reasons for the negative chemical effect on flame speed, shown

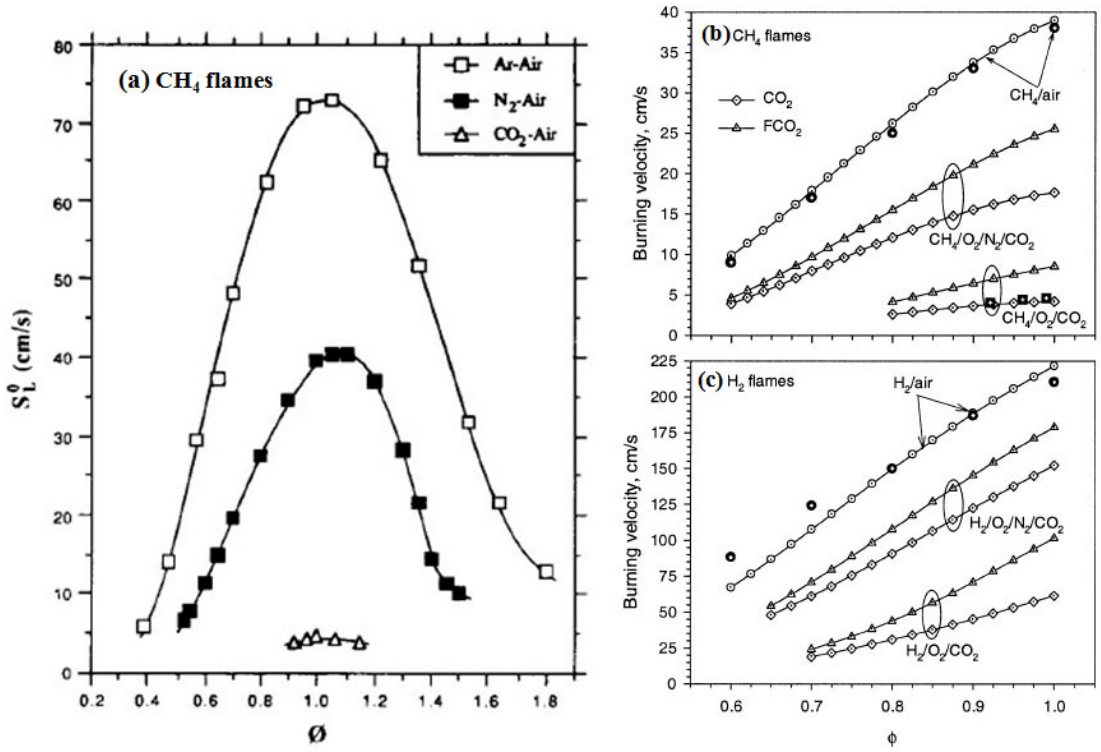

Figure 1.8: (a) Experimental laminar flame speeds S_L^0 (ϕ) for methane/Ar-air, methane/N_2-air, and methane/CO_2-air mixtures, at 1 atm Zhu, Egolfopoulos, and Law (1989). (b) and (c) Liu's computed results versus Zhu's experimentally measured flame speeds for methane and hydrogen flames Liu, Guo, and Smallwood (2003). The FCO_2 curves represent chemically inert CO_2 predictions.

in Eqn. 1.1.

$$CO + OH \leftrightarrow CO_2 + H \tag{1.1}$$

1.3 Oxycombustion in an IC Engine

Very few publications have been found in the literature related to oxycombustion in an IC engine. Bilger and Wu (2009) published the only study found which investigates the use of oxycombustion in an IC engine for the purpose of carbon capture. However, Bilger does not explore the possibility of running a traditional SI engine under oxycombustion conditions, rather he theoretically investigates the use of internal combustion Rankine cycle (ICRC) engines. Salt, Tree, and Kim (2012) have performed related work, researching the effect of using pure oxygen to supplement a diesel engine as the EGR fraction is increased to high

levels, but the objective was not to operate under full oxycombustion conditions and N_2 concentrations remain above 50%. Finally, Killingsworth et al. (2011) performed a study investigating the effect of oxycombustion in an SI engine, but utilizing Ar as the working fluid rather than CO_2 or H_2O.

Bilger and Wu (2009) investigated the competitiveness of an ICRC with other carbon-neutral power sources for use in an automobile. As such, the analysis assumes a vehicle which carries its own supplies of liquid fuel and oxygen, and have the capacity for temporary storage of the CO_2 captured from the engine exhaust. It is stated in the publication that oxy-fuel combustion in reciprocating engines has been used for many years in submarines, and systems are commercially available, however no references are given and no additional information could be found on the subject.

The engine theoretically evaluated by Bilger is 2-stoke, which has fuel and oxygen injected, compresses them with the end gas, then burns while pre-heated water is injected into the cylinder. The ideal cycle is shown in Fig. 1.9. The combustion process is assumed to occur in 2 stages: a brief constant-volume portion, followed by combustion during the expansion stroke with water being injected at a rate such that the in-cylinder pressure remains at a constant level. Once the combustion process has ceased the water inject is stopped and the mixture expands. Water injection is varied in correlation with the intake pressure such that the peak in-cylinder temperature is always on the order of 2700K. When considering only the engine, it was found that at partial loads, the thermal efficiency of the cycle could be as high as 50%, while at maximum load a thermal efficiency of 34% was predicted. Even with all external systems, including storage of the exhaust CO_2, it was concluded that the system could be inherently competitive in a carbon-controlled economy.

Salt, Tree, and Kim (2012) operated a diesel engine with pure oxygen supplement, reaching EGR rates as high as 81% (table 1.3). The EGR percentage is defined as the molar percent of the intake gases. The experiments were run with the intention of keeping the O_2 flow rate through the engine constant. N-EGR refers to run in which no additional oxygen was added, but as EGR was increased the intake pressure was also increases. O-EGR corresponds to runs in which pure O_2 was injected rather than increasing the intake pressure. Note that even when running 81% EGR the mole fraction of N_2 in the intake is still 0.511. Salt reports attempting to run 100% EGR, but being unable to maintain high enough intake temperature for combustion. Water condensation was a concern at higher EGR flow rates, as the EGR and exhaust system was not designed to maintain high temperatures. Runs were reported to be short enough to avoid problems. The design, shown in Fig. 1.10 used a liquid cooled heat exchanger to cool the EGR which condensed out the majority of the water. Salt found that the thermal efficiency of the engine was only slightly reduced as the EGR fraction was increased (Fig. 1.10). The majority of Salt's paper focuses on NO_x, which is reported to be reduced for both N-EGR and O-EGR primarily due to the flame temperature reduction, and particulate matter emissions.

The experiment performed by Killingsworth et al. (2011), while not related to carbon capture, is perhaps the most similar study which could be identified, as it operates an SI engine with a non-N_2 working fluid by utilizing pure O_2. The focus of the paper is on the

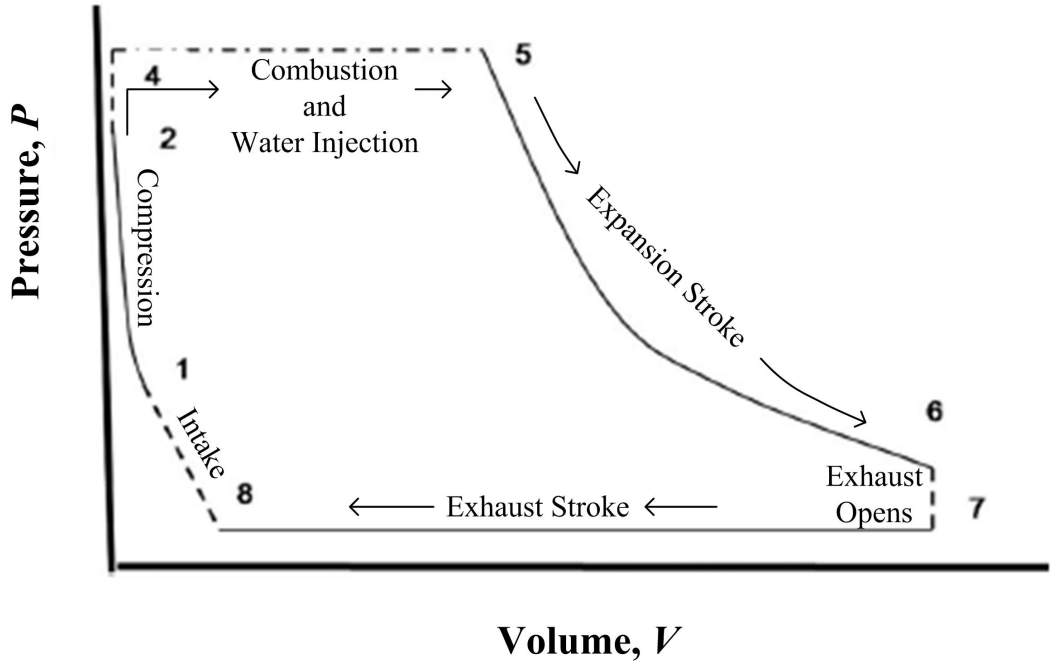

Figure 1.9: Ideal indicator diagram for a specimen ICRC engine.

Table 1.3: Intake gas compositions in mole fraction, N-EGR (ϕ =0.32), O-EGR (ϕ =0.37)

	% EGR	0%	11%	24%	35%	53%
N-EGR	$\mathbf{xN_2}$	0.792	0.794	0.797	0.799	0.804
	$\mathbf{xCO_2}$	0.001	0.006	0.014	0.023	0.041
	$\mathbf{xO_2}$	0.208	0.200	0.189	0.178	0.155
	$\mathbf{xH_2O}$	0.000	0.001	0.002	0.003	0.005
O-EGR	**%EGR**	**0%**	**47%**	**66%**	**74%**	**81%**
	$\mathbf{xN_2}$	0.792	0.738	0.650	0.583	0.511
	$\mathbf{xCO_2}$	0.000	0.049	0.096	0.134	0.174
	$\mathbf{xO_2}$	0.207	0.209	0.197	0.188	0.182
	$\mathbf{xH_2O}$	0.000	0.004	0.060	0.105	0.152

thermal efficiency advantages of operating an engine with Ar working fluid, which has a much higher ratio of specific heats than air. Note that the research concept was not original, but rather a continuation of an old concept. Laumann and Reynolds (1978) filed a patent on the concept, and Boer and Hulet (1980) and Ikegami, Miwa, and Shioji (1982) performed experiments and published papers on the subject, however, the work of Killingsworth is the most similar to the experiments in this thesis, and were performed on the same engine, and

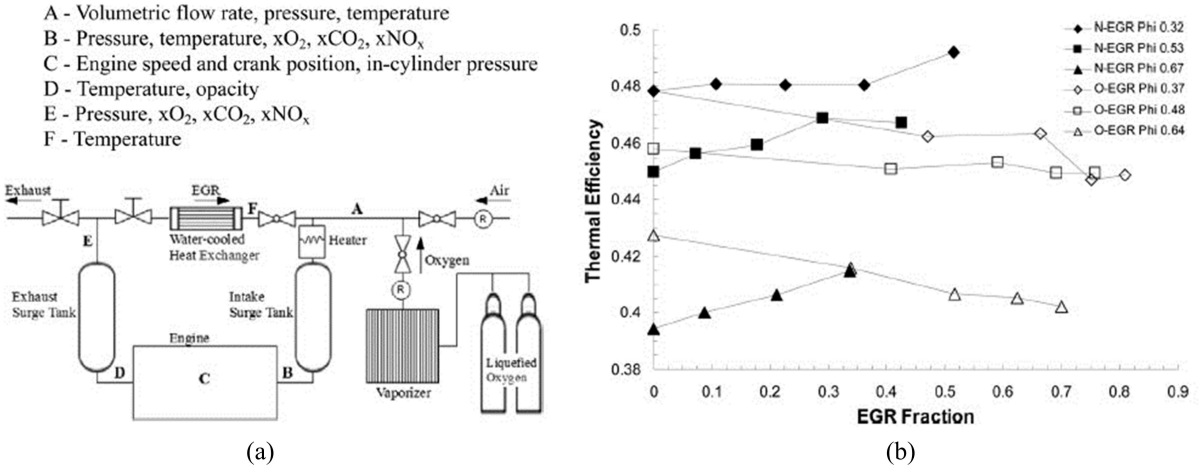

(a) (b)

Figure 1.10: (a) Flow diagram of the engine, EGR, and intake system. (b) Thermal efficiency versus EGR fraction. Data for each line is an average of three runs. (Salt, Tree, and Kim 2012)

thus will be the focus.

Intake gases were unheated, and the engine was run at 900 RPM for the experiments. Hydrogen and O_2 were always injected at a stoichiometric amount, with the ratio of fuel and oxidizer to Ar being varied. The work evaluated Ar concentrations of 84%, 86%, and 88% by volume. For all cases it was found that the compression ratio was highly limited by knock, with no possibility of operating above a CR of 7 without knock. However, even at low CRs the thermal efficiency of the H_2-O_2-Ar cases was found to be higher than H_2-air cases (Fig. 1.11). A three-zone model was used to help identify the reasons for the increase thermal efficiency, which were concluded to be: 1) reduced mass residing in the crevices that remains unburned, 2) reduced wall heat transfer (due to the lower compression ratio), and 3) faster burn due to higher in-cylinder temperature.

1.4 Conclusions

The far reaching effects of CO_2 emission has been established, with estimates predicting a bleak future for the earth's climate. Due to heavy reliance on fossil fuel, which are the main source of CO_2 emissions, there is little hope of curbing the production of CO_2 in the near-future. However, carbon capture and sequestration is a feasible method through which near-term reduction of CO_2 emissions could be reduced. There are many technologies and approaches to collecting CO_2 for sequestration, all of which have advantages and disadvantages. Oxycombustion is a viable option which is competitive with competing technologies and warrants further investigation.

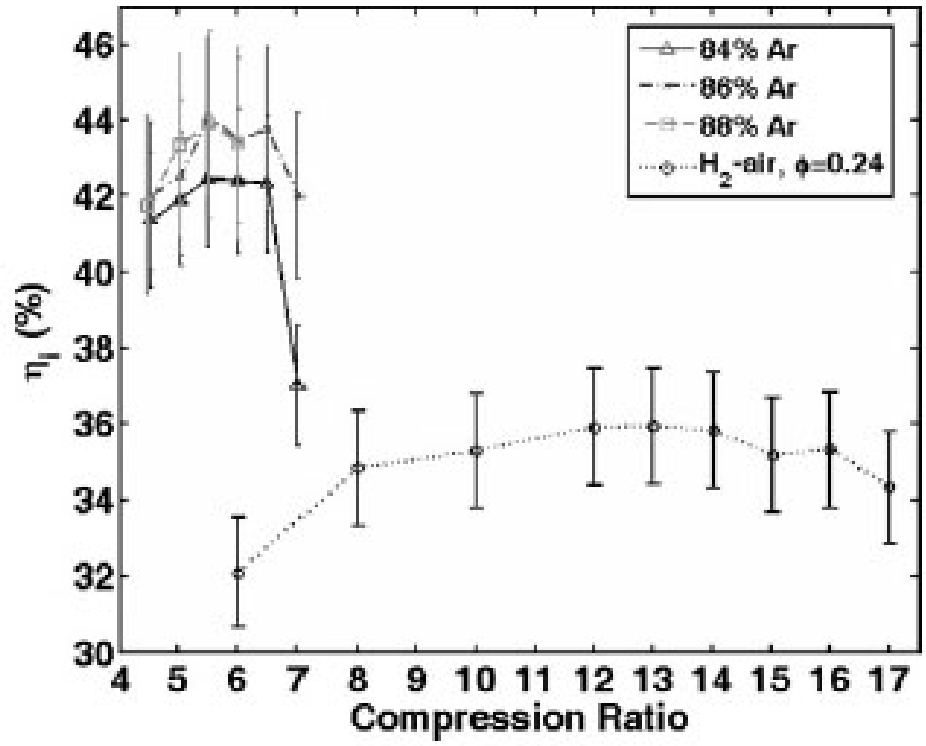

Figure 1.11: Indicated thermal efficiency versus compression ratio for H2O2Ar mixtures of 84%, 86%, and 88% Ar mole percentages and H_2-air mixture with $\phi = 0.24$. Error bars indicate the uncertainty of each measurement. (Killingsworth et al. 2011)

Despite the growing interest in CCS and oxycombustion, little experimental work has been performed in actual power generation systems. In fact, when investigating published works, not only was the research performed in this study unique, but very few similar studies exist. The research of Bilger and Wu (2009) is interesting and has a similar motivation, but takes a very different approach to using the piston engine in oxycombustion. Furthermore, Bilger performed only a theoretical study, where as the basis of this thesis is experimental research. Salt, Tree, and Kim (2012) experimentally ran an engine operating with pure oxygen injection and high levels of EGR (up to 80% of the intake by volume), but the experiments were on a diesel engine which has much different combustion characteristics and were of limited relevance as the volume fraction of N_2 remained over 50% for all presented cases. The work of Killingsworth et al. (2011) is the most similar, despite using no CO_2 or water working fluid. The process of analyzing the effect of an alternative working fluid in an SI piston engine, focusing on thermal efficiency, knock limits, and working fluid properties is very similar to the research in this thesis. One interesting note is how much lower the CR

had to be for AR working fluid in Killingsworth's experiment, which suggests that switching to CO_2 and water working fluid should allow significantly increased CRs. However, the analysis indicated that the CR did not significantly alter the efficiency between the Ar and air cases, but rather the combustion efficiency, heat transfer, and rapid burn rate improved the efficiency of the Ar cases. All three of the positive effects Killingsworth notes for Ar relative to air will be negative relative to air for CO_2 and water working fluids.

Chapter 2

Experimental Setup

All experiments were performed in the Combustion Analysis Laboratory at UC Berkeley. The engine used is a single-cylinder variable compression ratio Cooperative Fuel Research (CFR) F4 engine. A large external EGR loop was built on to the engine. The engine could be operated using the external EGR loop, or the loop could be sealed off, and the intake gases supplied.

2.1 Cooperative Fuel Research Engine

The engine used is a Waukesha CFR F4 engine, which is four-stroke, two-valve, single cylinder, port injected, spark-ignited engine with variable compression ratio (CR). There is no throttle on the intake, but intake pressure can be varied to simulate the effect. Main engine parameters are listed in Table 2.1. The engine can be run using either one or two spark plugs. For traditional single spark plug combustion the spark is mounted horizontally on the side of the combustion chamber. The optional second spark mounts vertically through the top of the cylinder head offset from the center on the opposite side as the horizontal spark. The head is made of cast iron and can be adjusted up or down during operation to vary the CR of the engine. A micrometer, with the upper mounted to the engine head, and the lower mounted to the engine body, is used to determine the current head height and corresponding CR. A clamping sleeve is used to lock the head in position once the desired CR has been reached. The piston has a flat geometry and the intake valve is plain, with no shrouds to promote mixing or swirl.

The engine is liquid cooled, using a constantly circulating system with the temperature controlled via a PID feedback system (Fig. 2.1). City water is used in a liquid-to-liquid heat exchanger to remove water from the coolant as needed. The flow of city water is controlled by an electronic needle valve, which is activated by a PID feedback system using a K-type thermocouple to monitor the coolant temperature. The CFR was originally designed to perform tests with a coolant temperature of 100°C, but the current coolant pump has a temperature limit of 80°C. Therefore the desired coolant-in temperature is set to 75°C for

Table 2.1: CFR ENGINE PARAMETERS AND OPERATING CONDITIONS.

Engine Parameters	
Type	Water cooled four-cycle
Bore	8.27 cm
stroke	11.4 cm
Cylinder swept volume	613.25 cm^3
Compression ratio	4 to 17.5
Combustion chamber volume	176.7 - 40.8 cm^3
Connection rod length	25.4 cm
Piston material	Aluminum
Piston rings	5 total (3 compression)

all tests. The difference between 100°C and 75°C is not significant for our testing, as the standard was written specifically for determining the octane rating of aviation fuels, which does not impact this study. The intake temperature dithers between 72-78°C while the coolant-out temperatures are between 80-88°C.

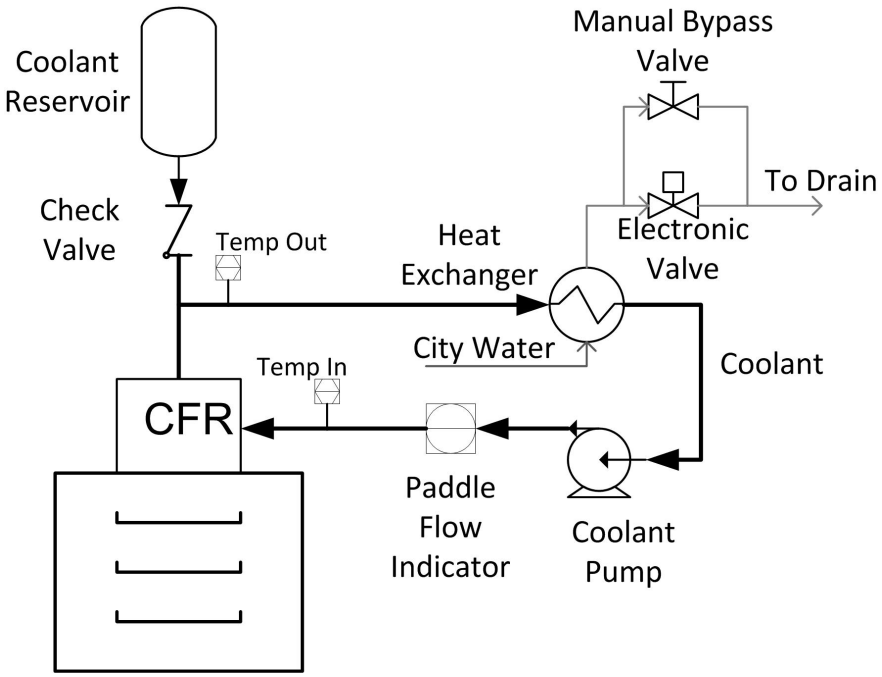

Figure 2.1: Diagram of the PID feedback controlled coolant loop.

An induction motor/generator and variable frequency drive are used to set and control

engine speed. The system can be driven or absorb power for a range of 600-1800 RPM, but the studies presented were run exclusively at the 600 RPM setting. Since the system uses an induction motor/generator the engine runs slightly below 600 RPM when it is being motored, and slightly over 600 RPM when being driven. Therefore most test data was taken at between 602-604 RPM. The engine's speed was measured by an optical encoder installed on the crankshaft. A BEI H25 optical encoder triggers acquisition from the intake and in-cylinder pressure transducers every 0.1 crank angle degrees.

Brake torque was measured using a 50lbs load-cell mounted on a torque arm of the induction generator. The generator was free to rotate about the drive-shaft axis, with only the load-cell and an oil damper restricting its movements (Fig. 2.2).

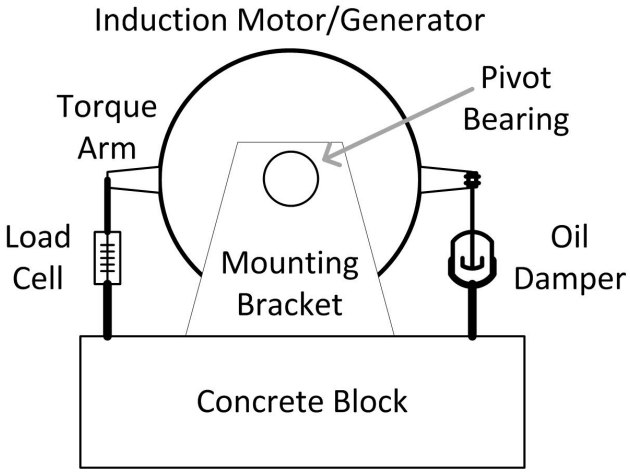

Figure 2.2: The induction motor/generator was mounted on a rotating axis, which allowed a load cell to meter the force applied.

Oil lubrication is provided by a gear pump located in the base of the CFR block. It provides roughly 40 psig when operating at 600 RPM. The oil temperature was not controlled, but would stabilize between 45-50°C during testing.

2.2 Air Setup

The engine could operated naturally asperated, drawing air from the room, or have a sealed intake with house air metered into the intake (Fig. 2.3). Ambient operation was used for motoring, warmup, and cooldown. All experiments were performed with metered house air.

House air was supplied at 100psig, and was immediately regulated down to 50psig. It then passed through the low pressure regulator, which reduced the pressure to anywhere from 0-10psig, depending on the running conditions and desired intake pressure. The absolute pressure and temperature were measured before the air passed through a sub-sonic orifice

with a differential pressure transducer measuring the pressure drop. After the orifice there is an internal coil heater with PID feedback control which can be used for testing elevated intake temperature cases. The surge plenum was built into the system prior to the installation of the intake plenum, and no longer serves a practical purpose. However, it does not pose any disadvantage to the system and therefore has been left in place. Ball valves are used to control whether the engine operates on only ambient air, only house air, both (when cooling down), or neither (when operating wet EGR).

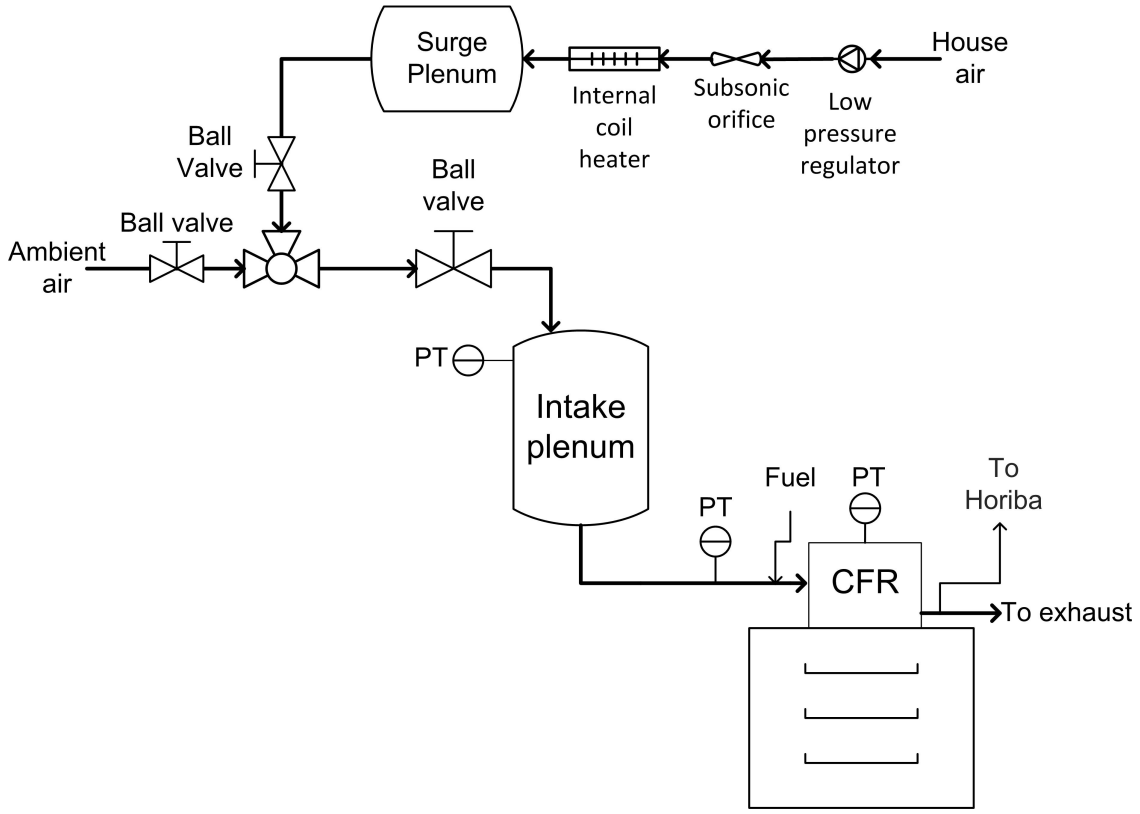

Figure 2.3: Diagram of the engine operating on ambient or house air.

2.3 Wet EGR Setup

An external EGR loop was constructed around the CFR engine (Fig. 2.4). The intake and exhaust plenums are used to dampen pressure fluctuation and promote homogeneity in the mixture. They are both cylinders 10.5 inches in diameter and 17 inches long, constructed out of stainless steel sheet metal. The exhaust plenum uses 4 inch V-band fittings for in the intake and exit, and a 2 inch female NPT fitting for the EGR loop. The intake plenum has 3 main ports, each which is a 2 inch NPT fitting. Both plenums have numerous 'bung' fittings

of 1/4 and 3/8 inch varieties which are used for pressure and temperature sensing as well as drawing gas samples. The exhaust plenum has a 4 inch wire tube connecting the intake and exit ports, which a blockage (a stainless steel flange was used for this) approximately 3 inches into the plenum. This combination of wire tube and blockage was designed to force the exhaust gas to expand and mix prior to exiting the plenum. Both plenums were constructed for us by Cleaire Advanced Emissions Controls.

Connecting the Exhaust plenum to the heat exchanger is 34 inches of flexible, stainless steel 1 inch ID swagelok tubing. All of the EGR tubing after the heat exchanger is 2 inch high-temperature radiator hose, and totals a length of roughly 5 feet. It is rated for a temperature of 160°C and is attached using barbed fittings throughout. The tubing connected the house air to the intake plenum is 1 inch ID flexible swagelok tubing. Large tubing was chosen throughout the system, minimizing pressure drops and heat losses.

The flow rate of wet EGR is controlled using a 1 1/2 inch high-temperature electronic butterfly valve mounted in the exhaust line downstream of the exhaust plenum. As the exhaust valve was closed the flow rate through the EGR loop was increased. Opening the valve had the opposite effect. For safety the valve could not be fully sealed, and did not have a sealing gasket, as it could not have been able to survive the high temperatures the valve was designed for. With the valve closed to its maximum level, the pressure in the EGR loop was maintained at roughly 1 bar. The globe valve between the intake and exhaust plenum was never used for adjusting EGR flow rate.

The heat exchanger used was an aluminum inter-cooler with a cross-flow gas-to-liquid design made by Spearco. Because the water is left in the wet EGR, and not condensed out, the gas cannot be cooled to below roughly 80°C. To provide additional confidence that no condensation is occurring, the gas is maintained at a 100°C throughout. The liquid coolant used was hot city water, with an intake temperature of 95-100°C, and a flow rate of roughly 1.2 liters per minute (lpm). The water was heated using the system shown in Fig. 2.5. The water flow rate was controlled using the needle valve just prior to the drain, result in the system operating at city water pressure, which is roughly 40 psig. For safety, a spring-loaded pressure release valve, set to release at 45psig, was installed in parallel with the needle valve. In the event that water stopped flowing the water in the heat exchanger would start to boil, greatly increasing the pressure. The pressure release valve ensures that the system, which is constructed of primarily 1/2 inch steel-braid re-enforced rubber tubing, would not fail.

Large changes in city water temperature were accomplished through changing the power level of the submersible heater. Fine control of the city water temperature was accomplished using the electronic needle valve. Any hot water which was allowed through the needle valve bypassed the brazed-plate heat exchanger and went directly to the drain. The resulting reduction in flow rate on the hot side of the brazed-plate heat exchanger lowered the water temperature entering the submersible water heater, and the net result was a reduction of cross-flow heat exchanger intake temperature.

The globe valve in the EGR loop is kept completely open when running wet EGR, and is completely sealed when running everything else. A globe valve was chosen because its geometry creates a turbulent environment, even when fully open, that helps to mix the

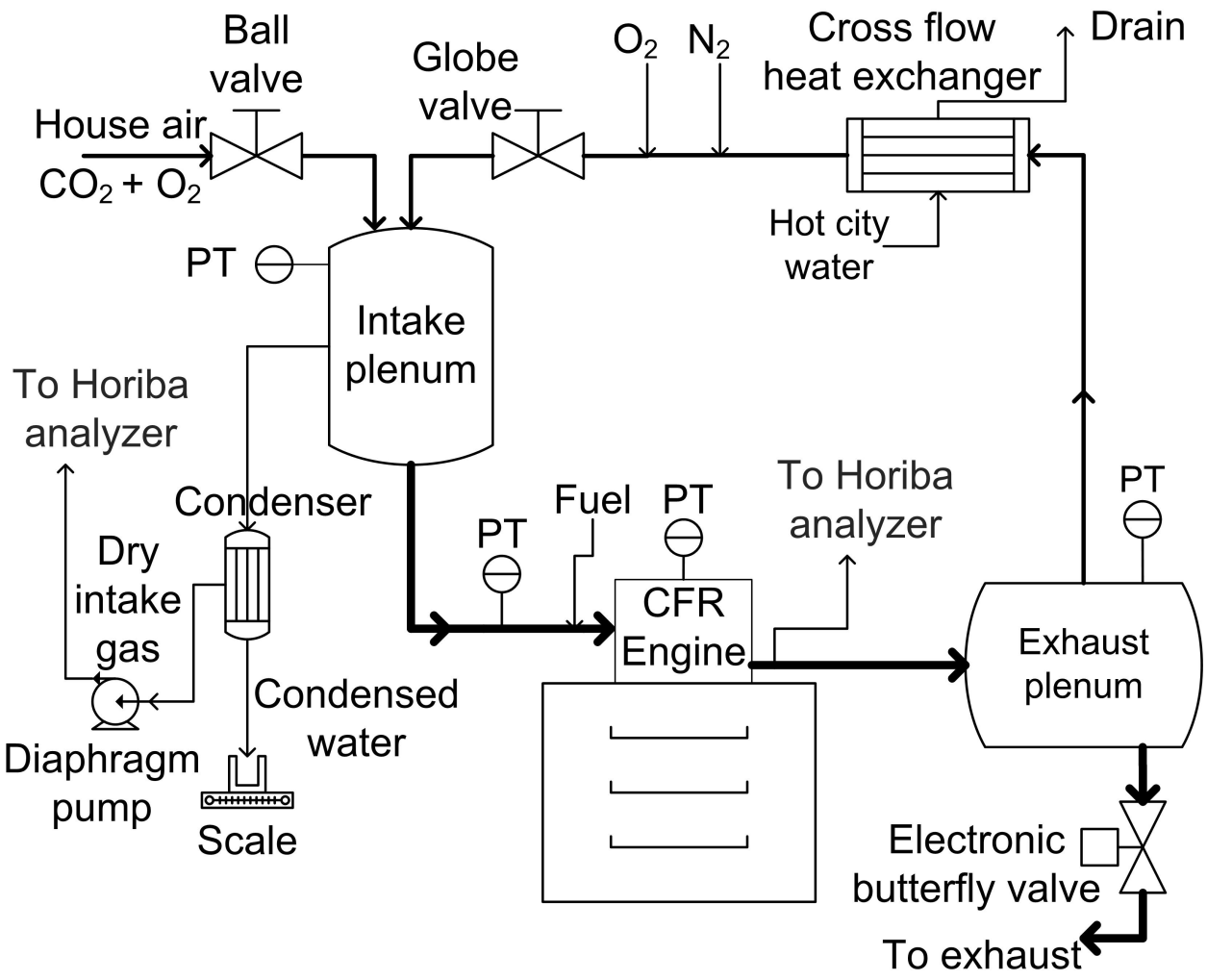

Figure 2.4: Layout of experimental setup. The full loop was used when operating with wet EGR. the globe valve between plenums was closed when operating on dry EGR and air. PT = pressure transducer.

injected O_2 and N_2 with the exhaust (Fig. 2.6).

With the exception of the tubing from the exhaust manifold to exhaust plenum, the entire EGR loop is insulated. The exhaust plenum, flexible hosing, and the heat exchanger are all insulated with at least 1 inch of high temperature ceramic insulation. It is in the form of a 1 inch thick flexible sheet, capable of withstanding 1200°C. After the heat exchanger, all lines are wrapped with electric resistance heating tape. The tape is approximately 1 cm wide, and wrapped at an interval of approximately 1 inch. The resistance of each is a function of the length of each and whether the wires are connected in series or parallel. The intake plenum is heated by a 12 inch by 18 inch silicon heating pad. The resistances off all

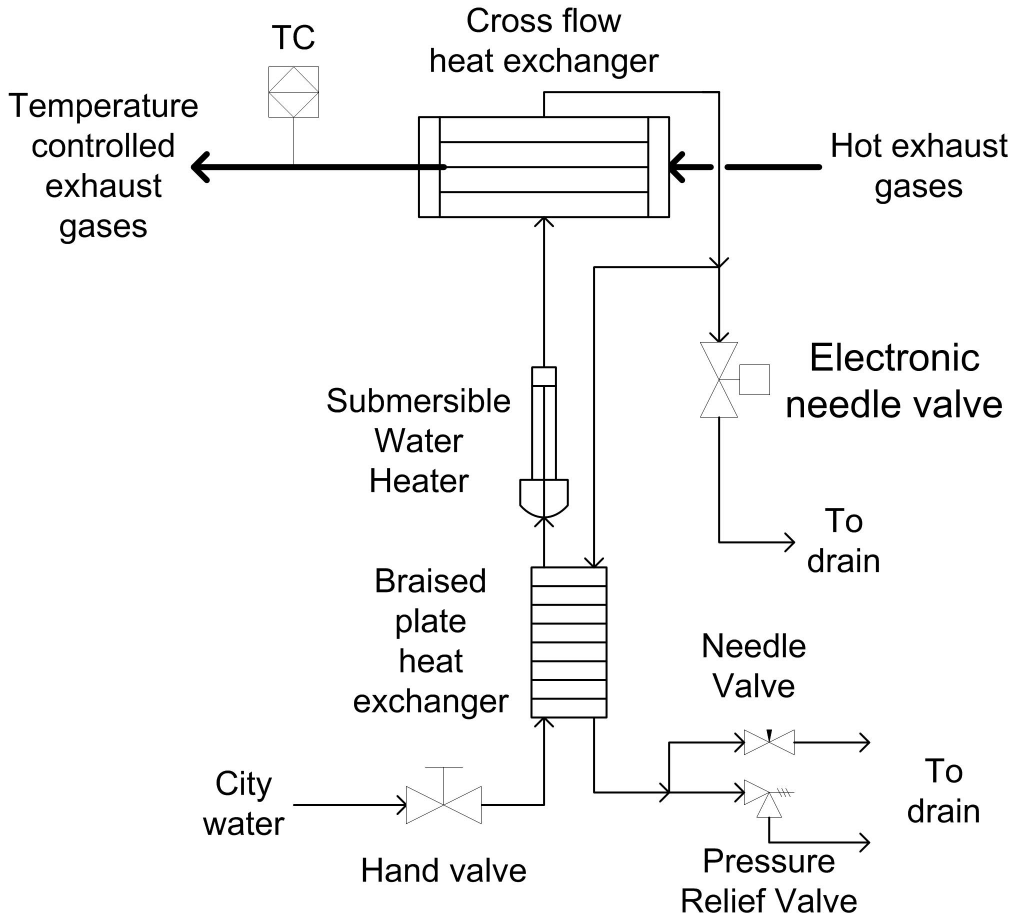

Figure 2.5: Layout of the system used to control the intake temperature of the city water for the EGR heat exchanger.

individual heating lines are listed in Table 2.2. All heated portions of the EGR loop are wrapped in 1/4 inch think NOMEX insulation, and then covered with 1 inch thick melamine insulation. The heat input of each section is adjusted using manually controlled variacs.

The condenser shown in Fig. 2.4 is used to determine the water concentration of the intake gases. A slipstream is drawn from the intake plenum through the condenser, which consists of a long 1/4 inch Teflon hose spiraling around a cylindrical collection chamber all of which rests in an ice bath, at a rate of just under 1-lpm using a diaphragm pump. The collection chamber is constructed from a 1 1/2 inch stainless steel pipe with reduction fittings on both ends. Approximately 3 inches from the base, a 1/4 inch NPT bung has been welded in place, which is where the gas and condensed water enter the chamber after passing through the spiraling wraps. The chamber is not sealed, but rather is open at the bottom through a long Teflon tube which extends through the bottom of the ice bath and into a

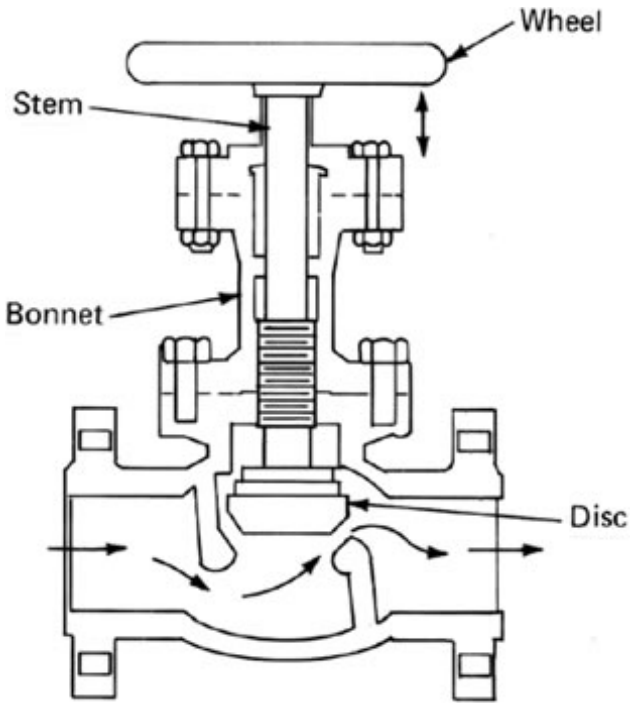

Figure 2.6: A globe valve creates a turbulent environment even when fully open.

Table 2.2: Measured EGR Heater Resistances.

Heater Resistances (Ω)	
EGR Valve	24
Valve to Plenum	57
Intake Plenum	21
Intake Manifold	109
Water Heater	7.2
Oxygen Line	34

collection cup. 4 Teflon coated wires inside the drain tube prevent any bubble entrapment due to adhesion. Because the EGR loop operates slightly below atmospheric pressure the tip of the drainage tube must always be submersed, allowing it to suck in water until equilibrium pressure between the gas and the static water column is reached.

After the water is condensed out, the dry exhaust stream passes through a 1-lpm mass flow meter and the measurement is recorded once a second. The gas then passes through the diaphragm pump, after which it is either vented, or can be sampled to look at the gas concentrations or the volumetric flow rate. The condensed water accumulates in the collection chamber, which sit on a scale. The reading of the scale is recorded during each

run point, so the that the water collection rate vs. time can be determined.

2.4 Dry EGR Setup

Dry EGR refers to exhaust gas in which the water has been removed, leaving only CO_2 and trace species. Because the external EGR loop was not designed to condense out water all experiments were run using bottles of CO_2 with no real EGR flow. This technique has the disadvantage of not recirculating any of the products of poor combustion (i.e. unburned $_2$, hydrocarbons, and CO) but it satisfies the criteria of experimentally measuring the performance of a primarily CO_2 working fluid. A layout of the delivery system used is shown in Fig. 2.7. The CO_2 bottles contain liquid, but are designed to draw gas out of the top of the bottle. Because of the rapid use of CO_2, and the rate of evaporation, the gas and bottle become very cold. The regulator and lines directly after the bottle are therefore heated using electric resistance heating wraps. The power of these wraps is controlled by hand using variacs, and set to heat the gas as much as possible without damaging the tape. The gas is regulated to 50 psig out of the bottles and heated to near room temperature. It then passes through a mass flow meter, which is used to ensure steady flow throughout the test. Details of the flow meter are discussed in section 2.4, which covers all flow meters and controllers used. A low pressure regulator is then used to step the pressure down to 2-3 psig. At this point it is mixed with O_2 and N_2, and the mixture passes through a subsonic orifice with differential pressure measurement. After the orifice the gas is heated using a PID feedback heater typically used for house air. Using this heater, the mixture can be heated to room temperature (compensating for the expansion of the CO_2), or high enough for the intake to reach 100°C, for direct comparison to wet EGR tests. After leaving the internal coil heater the gas flows through roughly 3 meters of 2 inch tubing, all with ceramic insulation, and is deposited into the top of the intake plenum. The globe valve in the EGR loop is closed, forcing all gas to pass through the engine.

Mass Flow Meters/Controllers

A total of nine mass flow meters and/or controllers are used as part of this experiment, and control or monitor the majority of the gas flows. Table 2.3 lists the different flow meters, the gases they were calibrated for, the gases they are currently used for, and whether they are used as a controller or a meter.

The 35-lpm and 50-lpm are used to control and meter the O_2 injection during both wet and dry EGR runs. When additional O_2 is required one of the 5-lpm flow controllers is moved to be in parallel with the 35-lpm controller, and the flow of both pass through the 50-lpm. Under normal conditions, two 5-lpm units are in series, with the first controlling and the second metering, N_2 into the system. The 20-lpm flow controller was calibrated for CH_4, and is used to measure the fuel flow rate. The fuel flow is controlled by the injector pulse width, which the MOTEC ECU adjusts to maintain a stoichiometric run point. The 10-lpm

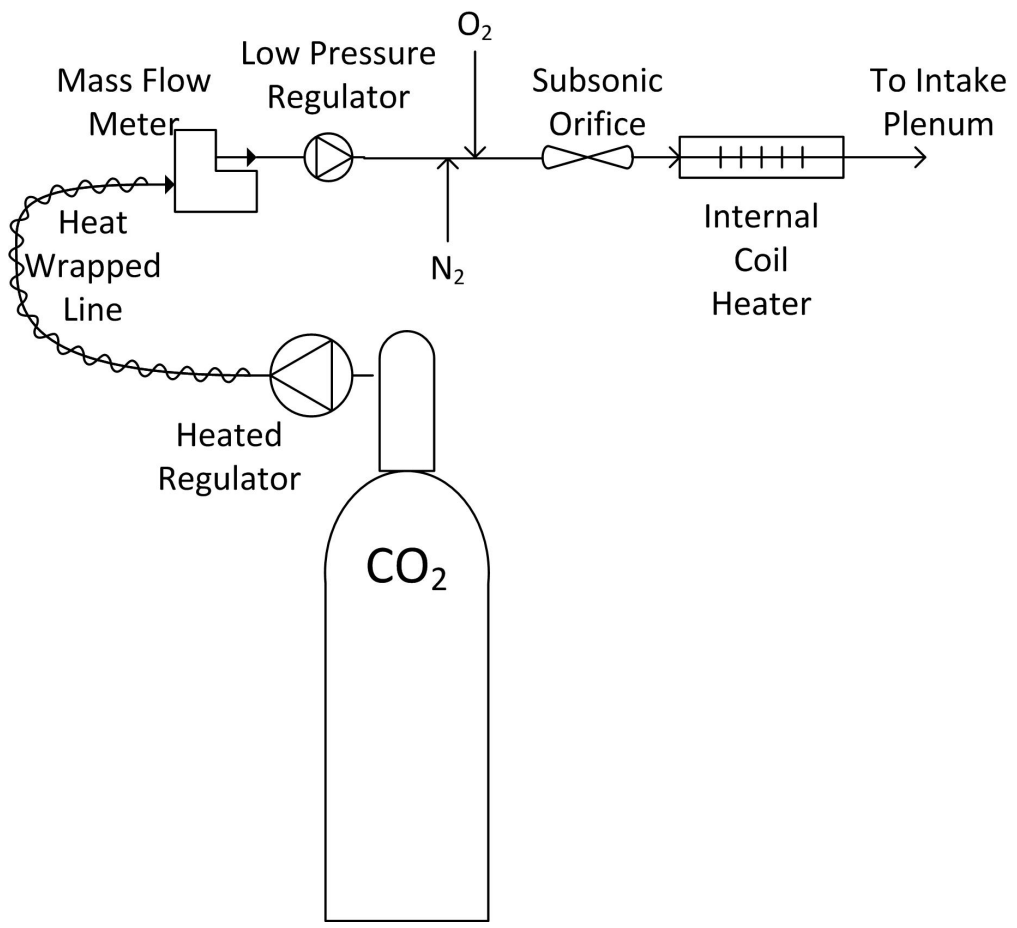

Figure 2.7: Layout of the system used to deliver simulated dry EGR to the intake of the engine.

flow controller is used in the sample dilution system, described in section 2.5. The 1-lpm flow meter is used to measure the flow rate of dry gas from the intake slip stream during wet EGR experiments. The third 5-lpm flow meter is used to measure the flow rate of the Horiba sample (either exhaust or intake). The 200-lpm flow meter is used to measure the flow rate of CO_2 during dry EGR experiments, and is programmable to measure a variety of gases, including CO_2.

Table 2.3: Mass Flow Meters/Controllers Used in the Experiment.

Size	Calibration Gas	Flow Gas	Controller	Meter
35-lpm	O_2	O_2	x	
50-lpm	N_2	O_2		x
5-lpm	N_2	N_2	x	
5-lpm	N_2	N_2		x
20-lpm	CH_4	CH_4		x
10-lpm	N_2	N_2	x	
1-lpm	N_2	Intake		x
5-lpm	N_2	Sample		x
200-lpm	Air	CO_2		x

2.5 Sampling System

Horiba Gas Analyzer

Sampling of exhaust and intake gases is performed using a Horiba test rack, including sensors for hydrocarbons, oxygen, carbon dioxide, carbon monoxide, and nitric oxides. A single sample can be split between these five sensors using flow-control rotometers. Testing can be performed with a single sensor, or all five at once depending on flow rates and user preference. The sensors all require that water vapor be removed from the sample. The bulk of the water is removed using a condenser which uses a descenging spiral of Teflon tubing in an ice bath, connecting to a collection chamber. The unit is almost identical to the intake condenser described previously, except it is fully sealed. Water must be periodically removed from the collection chamber by opening a ball valve at the base of the unit. Since the gas passing out of the collection chamber still contains a small amount of water vapor, it travels through a heated tube to the Horiba, where a dyer is used to remove any remaining moisture.

In the following sections the operating principle of each sensor is discussed.

Flame Ionization Magneto-Pneumatic Analyzer

The FMA-220 total hydrocarbon analyzer measures the total hydrocarbon concentration (FIA) as well as the oxygen concentration (MPA). The total hydrocarbon concentration is measured using a flame ionization detector while the oxygen concentration is measured with a magneto-pneumatic condenser microphone system. The basic principle of the hydrogen flame ionization detector is shown in Fig. 2.8[1]. When a hydrocarbon is exposed to the hydrogen flame it causes the tip of the jet nozzle to undergo ionization. An electrode, placed on either side of the tip of the flame, with a DC voltage is applied, and the ionization results in a flow of ions between the electrodes proportional to the number of carbon atoms.

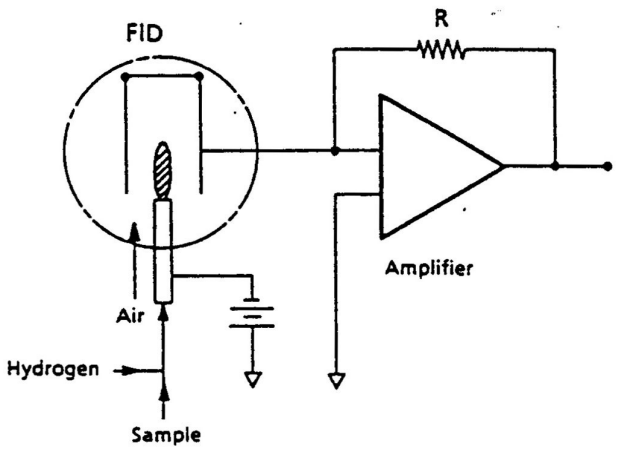

Figure 2.8: Diagram of the Hydrogen Flame Ionization Detector.

CO and CO_2 Infrared Analyzer

The Horiba AIA-210 infrared analyzer uses a non-dispersive infrared analysis for constant measurement. Figure 2.9[2]shows the basic principle of the infrared analyzer. Infrared light emitted by a light source is converted into intermittent light by a chopper. The intermittent light passes the measurement cells (sample and reference cell) and enters the detector cell. In the measurement cell infrared light is absorbed by what causes a difference in intensity between the two beams entering the detector cell. This difference causes a membrane, located between the two detector cells, to vibrate and the changes in capacity between the electrodes for the membrane generates an electric output. Each component absorbs a specific infrared wavelength to which the detector is set but there is no response to any other wavelength. Hence, a change in infrared absorption means a change in concentration of a component.

NO_x Chemiluminescent Analyzer

A Chemiluminescent Analyzer is used to measure NO or NO_x concentration in the exhaust gas. For the NO determination NO and O_3 are mixed in a reaction chamber which produces a chemiluminescent reaction (eqn 2.1), with the light emitted being directly proportional to the concentration of NO. Silicon photo-diodes sense the emitted light. NO_x is determined by the same principle except that prior the entry into the reaction chamber NO_2 is first dissociated to NO.

[1]Horiba Instruments INC., Instruction Manual for FMA-220 FIA-220/MPA-220 Flame Ionization Magneto-Pneumatic Analyzer, 1990.

[2]Horiba Instruments INC., Instruction Manual for AIA-210/220 Infrared Analyzer,1991.

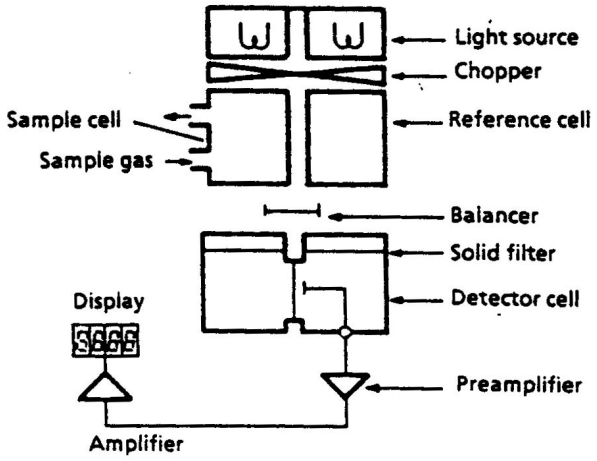

Figure 2.9: Infrared Analyzer for measuring CO and CO_2.

$$\begin{aligned} NO + O_3 &\rightarrow NO_2^* + O_2 \\ NO_2^* &\rightarrow NO_2 + hv \end{aligned} \tag{2.1}$$

Sensor Limitations

The CO_2 and O_2 sensors in the Hoibra test bench have saturation limitations which are exceeded when running oxycombustion experiments. After condensing out the water, it is expected for the dry exhaust stream to be over 90% CO_2, and the dry intake can have as much as 40% O_2 and up to 75% CO_2 for the extreme cases. However, It was found that the Horiba was no longer in its linear region for any CO_2 concentrations over 16%, and that the O_2 sensor was only accurate below 21%.

Calibration mixtures of CO_2 in N_2 of 11%, 20%, and 25% were purchased to extend the calibrated region of the CO_2 sensor. While the sensor reading was not linear in these regions, it was possible to use these points to define the correlation between the sensor reading and the actual gas concentrations. A sample curve is shown in Fig. 2.10. When analyzing samples, a linear linear correlation was assumed between 0 and 11% CO_2, and a second-order polynomial is used between 11 and 25%.

Dilution System

Since even with the extended CO_2 curve fit it was not possible to directly measure the CO_2 or O_2 concentrations for several test points, it was necessary to develop a dilution system. A diagram of the system is shown in Fig 2.11. The system uses a mass flow meter to measure

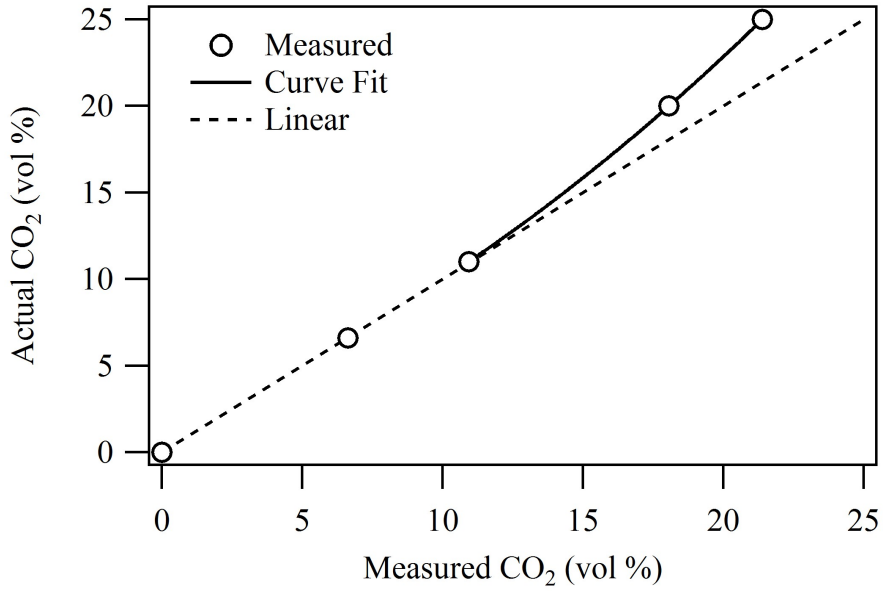

Figure 2.10: Actual concentrations vs. Horiba readings when measuring CO_2 calibration gases.

the dry sample leaving the condenser, and a mass flow controller to meter in a precise amount of N_2 dilution gas. A needle valve prior to the Horiba pump is used to control the flow rate of sample gases, and the 10-lpm N_2 flow controller was controlled and read from a computer. The gases were mixed just after the pump, and passed through over 1 meter of 1/4 inch tubing before reaching the test benches, allowing ample time for complete mixing to occur.

This dilution system requires very accurate measurement of the flow rates of both the sample and the N_2, as well as precise measurement of the diluted concentrations. To increase the accuracy of the measurement of the diluted sample, dilution quantities were chosen which resulted in a CO_2 concentration close to one of the calibration mixes (either 20 or 25%). O_2 was in the linear region of the test bench as long as the concentration was below 21%, so target values were more general. An attempt was made to capture points which had close to 21% O_2, but the concentration of CO_2 was prioritized.

Wet Test Meter

The accuracy of the mass flow meters was measured using a 0.25 cubic foot wet test meter. The wet test meter is a positive displacement gas flow meter which counts the number of times a fixed water volume is displaced by gas. To get the flow rate, the time for a certain displacement must be recorded and then the flow rate versus time is computed. The displacement volume is sensitive to the fill level of the meter, and thus care must be taken to ensure a proper fill level before each test. Additionally, time must be given for the water in

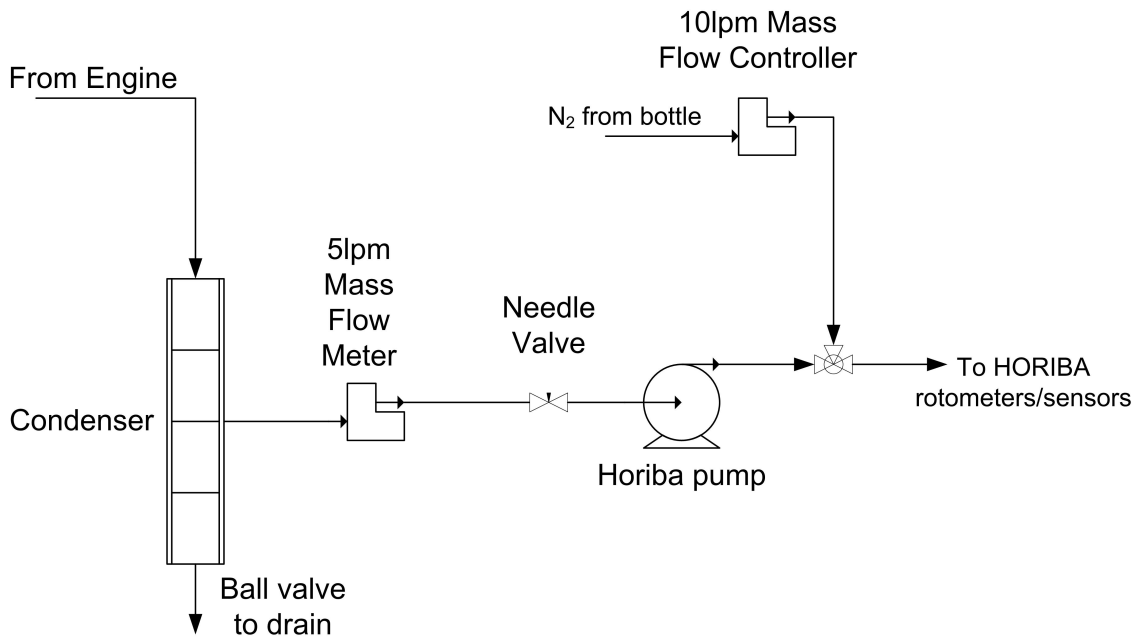

Figure 2.11: Horiba sample dilution system for measurement of high concentrations of CO_2 and O_2.

the meter to saturate with whatever sample gas is being tested. Because the gas is exposed to water, it is assumed that all gas exiting the meter is saturated at room temperature and pressure. In addition, it is assumed that the gas is dry entering the meter (having just exited the condenser), and that as it passes through over 5 meters of 1/4 inch tubing and a pump it equilibrates to room temperature. The results of calibration tests between the 10-lpm N_2 dilution flow controller and the wet test meter flow rate are shown in Fig. 2.12.

There is good agreement between the wet test meter and the flow controller, with better agreement at higher flow rates. It is expected that the flow meter accuracy is not as good at very low flow rates (relative to maximum) and thus when possible it is operated above 2-lpm. Slight adjustments were made to the 10-lpm flow controllers readings based on these tests. Similar tests were carried out for all flow meters and controllers used in the system, with corrections made when necessary.

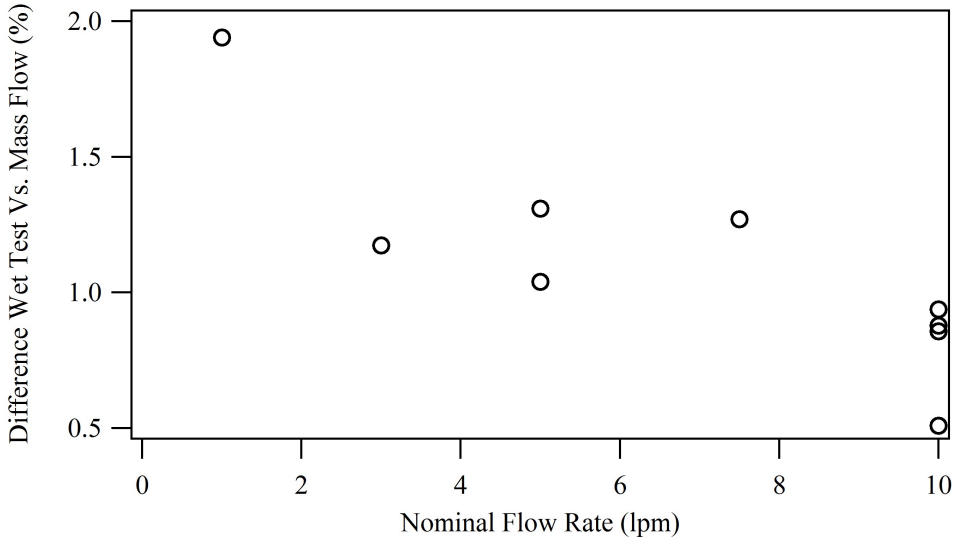

Figure 2.12: Percent difference between the 10-lpm N_2 dilution flow meter and the wet test meter.

Chapter 3

Experimental Procedure

A variety of experiments were performed, each with different procedures, but there are some conditions which were constant across all experiments. All experiments were performed at steady-state. Prior to running any experiments, ambient pressure and temperature were recorded and motoring traces were collected with ambient air and a CR of 10 to ensure consistency of systems and readings. Following the motoring traces, firing traces were taken. When operating with methane spark timings of 10, 15, and 20°BTDC were collected after the engine coolant had reached operating temperature. This tested the consistency of additional systems, including the fuel flow meter and the calculation of the thermal efficiency. The engine was always warmed up to ensure coolant had reached operating temperature and the oil temperature was above 35°C. Additional procedures were followed for each specific run condition.

Once a desired operating point was reached and the necessary intake and exhaust samples had been collected, engine data collection would occur. The CR would be adjusted to the desired setting, recorded, and the desired spark timings would be tested. This typically involved a spark sweep which spanned the maximum brake torque and maximum thermal efficiency points. For some cases the spark-timing was adjusted to investigate the onset of knock, which was calculated and displayed in real-time on the data acquisition system.

3.1 Air Operation

The engine was operated on air frequently, as at a minimum all test days warmed up while operating on air. When running on air, the engine could be naturally aspirated, or run on metered house air, as shown in Fig. 2.3. Ambient air was used only for warm-up, cool-down, or calibration runs. All experiments were performed using house air. Since absolute pressure, temperature, and differential pressure were measured at the subsonic orifice it was possible to compute the mass flow rate of air entering the system. The heater was used when elevated intake temperatures were required.

The engine was motored until coolant and oil temperatures reached operating tempera-

tures prior to the collection of any data. Additionally, CR 10 traces were always taken to start to serve as a reference.

When running air cases the concentration of CO_2 in the exhaust is low, and therefore it is not necessary to use the dilution system described in section 2.5. Since the dilution system was not used, it was not necessary to measure the sample rate with mass flow meters or the wet test meter. Exhaust samples could be drawn at any rate desired, with no effect on the engines operation. There is no CO_2 or other exhaust species in the intake, and a constant and well known O_2 concentration, so no intake composition measurements were performed.

3.2 Wet EGR Operation

Startup

One of the primary concerns when running wet EGR was condensation and water pooling due to cold sections in the EGR loop or exhaust. Preheating of the system was therefore necessary, and was accomplished through a combination of hot house air, heated by the internal coil heater shown in Figure 2.7, and use of the resistance heaters, listed in Table 2.2. The hot house air was supplied at a rate greater than the engine could accept, which resulted in hot air not only passing through the motoring engine, but also flowing backwards through the EGR loop and down the exhaust. Using this technique it was possible to heat the engine intake and exhaust system as well as the EGR loop simultaneously. It also made it possible to fire the engine, further heating the exhaust system as well as the coolant and oil, without risking condensation in the EGR loop (since hot air was still flowing backwards through this loop). During this process the heat exchanger system, shown in Fig. 2.5 was also being heated. The system primarily relies on recovered heat from the brazed plate heat exchanger to maintain temperature as the heater does not have enough power to sufficiently heat all of the water at the specified flow rate. However, since the brazed plate heat exchanger is very efficient, heat from the submersible water heater and heat from the hot air flowing backwards through the EGR loop get recycled in the system and eventually the temperature reaches the desired 98°C.

Once all of the systems are at or above 100°C (with the exception of the heat exchanger water, which must be above 90°C) and the engine has been firing for long enough to sufficiently heat all fluids and the exhaust system, the system can be switched to EGR by slowly sealing off the house air while increasing the O_2 flow rate and closing the exhaust butterfly valve. Once the house air flow is sufficiently low the line is closed off completely using a ball valve at the top of the intake plenum.

Sampling

A constant slipstream was pulled from the intake plenum and drawn through the condenser and mass flow meter using a diaphragm pump (Fig. 3.1). The flow rate was kept low

- less than 1-lpm of dry gas - to minimize the effect on the system. The system was run continuously for 2 reasons: 1) it was found that if a sample was only drawn periodically it had a noticeable effect on the experiment, affecting, among other things, the power output and emissions. By drawing constantly at a very low rate the effect was constant, and therefore the system maintained steady-state during sampling, which was done by simply re-routing the slipstream exhaust through the Horiba or wet test meter rather than venting it. 2) Drawing a constant flow rate during the entire experiment resulted in water being collected at a constant rate during the experiment. This greatly improved confidence in the water collection rates measured.

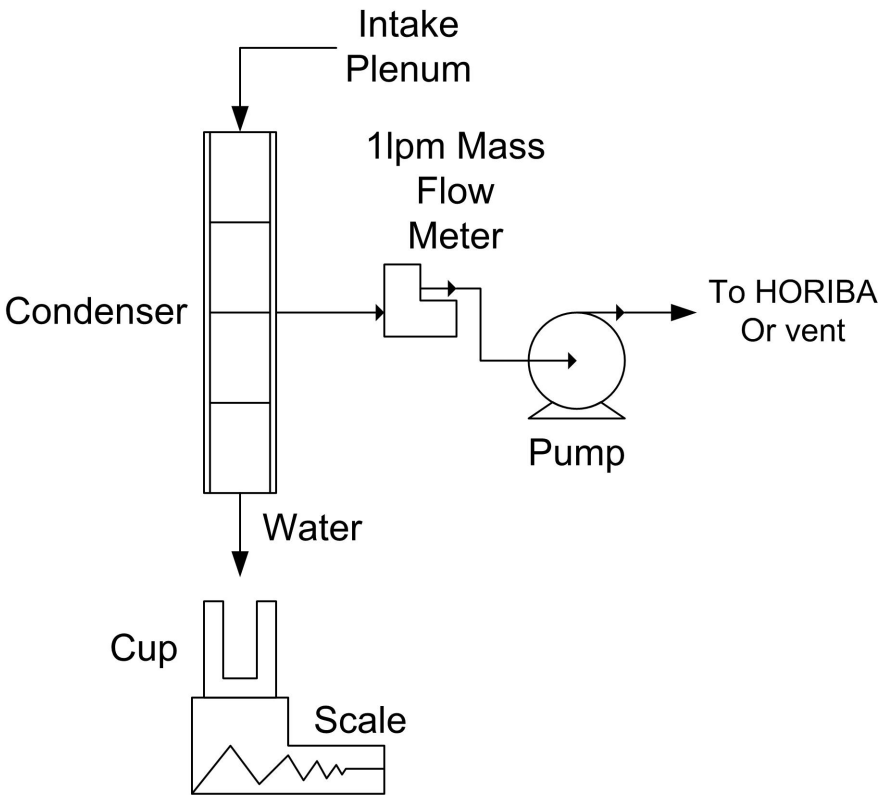

Figure 3.1: Layout of the system used to pull a steady slipstream from the intake plenum.

The exhaust could be sampled more freely, as drawing a sample of 5-8-lpm had no noticeable effect. The exhaust was only sampled on-demand, rather than pulling a constant slipstream. Exhaust could be drawn from 3 points in the exhaust system: the exhaust manifold, the exhaust plenum, and just after the exhaust back-pressure valve. When measuring combustion efficiency the port at the exhaust manifold was used, as it allowed very little time for further reactions to occur outside of the cylinder. The exhaust plenum port was used for the main exhaust composition tests. The port after the exhaust back-pressure valve

was only used when it was desired to pull a large amount of gas, and the accuracy of the sample was not prioritized over the isolation from the system that being downstream of the valve supplied.

When running experiments, sampling was performed on both the intake and the exhaust for each O_2 concentration prior to collecting performance data or pressure traces. The sample would first be measured in the Horiba at a minimum of 2 dilution levels for a minimum of 90 seconds per sample. After the Horiba sampling was complete, the sample would be passed through the wet test meter to determine the volumetric flow rate, which was used to determine the GCF, as discussed in section 4.1. When using the wet test meter on the intake gas the pump shown in Fig. 3.1 was used. Since the exhaust was not pumped constantly a second pump was required for these tests, as shown in Fig. 3.2. If the two dilution points taken prior to measuring with the wet test meter were not in good agreement, an additional Horiba test would be performed after the wet test meter measurement had concluded. Once all sampling was concluded performance tests could be performed, with the Horiba taking a raw(undiluted) sample from the exhaust manifold port to determine the combustion efficiency if desired. The fuel mass flow rate served as a indicator of the consistency of the run, as if the fuel flow rate changed, either abruptly or over time, it could be concluded that the intake composition had not been stable, and therefore the measurements were not reliable.

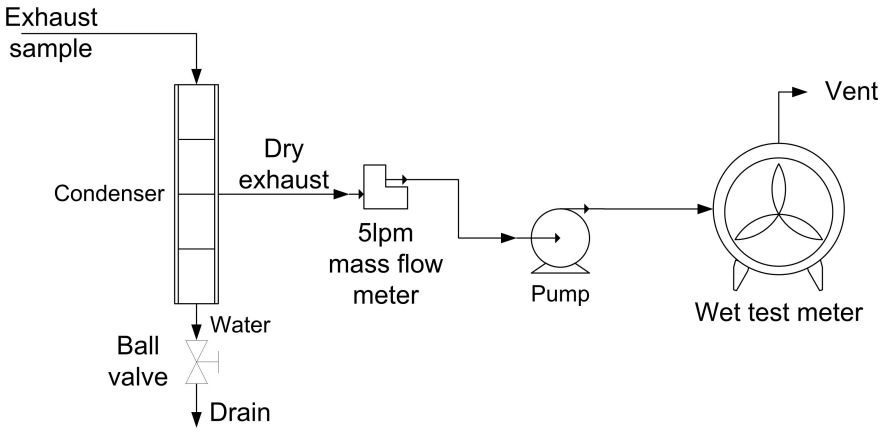

Figure 3.2: A second pump was used to draw the exhaust through the condenser and mass flow meter before being pumped through the wet test meter.

Maintaining Steady Conditions

Once the sampling process was complete the wet EGR runs were stable and required only monitoring during the performance tests. It was necessary to regularly check the O_2 and methane bottle levels, and swap them when necessary. For both O_2 and methane a system

was devised using two regulators and hand valves allowing bottle switches to be performed without disrupting the gas supply. Thus experiments could be run for many hours on end. Temperature monitoring was also important, both to prevent condensation, and to maintain the intake temperature within the desired range. The hot city water used in the heat exchanger also had to be carefully monitored, and the flow rate through the bypass valve (Fig. 2.5) adjusted accordingly.

3.3 Dry EGR Operation

As mentioned previously, dry EGR experiments were not run with true EGR, but rather the recirculated exhaust was simulated using bottled CO_2. Delivery of all three intake gases (CO_2, O_2, and N_2) was accomplished using the system shown in Fig. 2.7.

Startup

The engine was first fired on air to heat the coolant, oil, and exhaust to steady temperatures. Ambient air was used for this when running unheated intake conditions. If an elevated intake temperature was desired, hot house air (heated using the internal coil, PID controlled heater) was used. Once all systems had reached the desired, steady temperatures the system could be switched to CO_2.

When switching, the engine would be stopped temporarily. The CO_2 flow (without O_2 or N_2) was then started and allowed to pass backwards through the EGR loop, flushing out the air. Once the EGR loop had been flushed briefly the engine was started motoring with the EGR loop open. Several minutes of purging (i.e. motoring pure CO_2 with the EGR loop open) ensured the air was removed from the system, and would not influence the composition measurements. Once the purging was completed, the EGR valve was closed and the O_2 and N_2 injection were started. Fuel injection and combustion were initiated as soon as the oxidizer had stabilized. Since the flow rate of CO_2 was controlled by a sub-sonic orifice it was sensitive to the downstream pressure, which was slightly higher when fuel was being injected. Therefore, fuel was always injected during stabilization periods and during intake sampling. As the systems began to stabilize the back-pressure of the CO_2 was adjusted to reach the desired intake manifold pressure.

Sampling

Sampling of the intake composition of each dry EGR condition was performed prior to performing any performance studies. All three of the gases blended together to create the intake oxidizer were measured using mass flow meters, but the confidence in the absolute accuracy of the CO_2 meter was unknown and the flows were too great to confirm accuracy using the wet test meter. Instead, the reading of the CO_2 flow meter was used to confirm

that the flow rate of CO_2 was constant over the entire run, and did not decrease as the bottle emptied or gas temperature decreased.

Intake samples during dry EGR experiments were only drawn when needed. There was no need to run the intake condenser system as there was no water in the oxidizer, and the effect of sampling the intake had very little effect on the overall system since there was no real EGR to compound sampling effects. In addition, the CO_2 flow meter was used to verify consistency between mixture ratios when sampling the intake and mixture ratios when running performance tests.

The high CO_2 and O_2 intake concentrations in the oxidizer required the use of the dilution system (Section 2.5) when sampling with the Horiba. Samples were drawn at a rate of approximately 2-lpm, and three dilution fractions were tested. The wet test meter was not used for these tests.

Undiluted exhaust samples were taken during runs from the port in the exhaust manifold. Diluted exhaust samples were not taken, since the only species which could be measured was CO_2, which was not as valuable as the undiluted measurements of NO_x, CO, and unburned hydrocarbons.

Chapter 4

Analysis Methods

A wide range of properties were investigated, both experimentally and numerically. All of the studies required the measurement of intake compositions for the EGR experiments, and pressure traces were always collected. Wet EGR experiments additionally required the determination of the water vapor fraction and EGR flow rate. Some studies included the investigation of knock limits, with knock indicators being calculated in real-time during runs as well as with the filtered data.

In this chapter, the methods and techniques used to analyze the various aspects of the experiment will be presented.

4.1 Gas Correction Factor

All of the electronic flow sensors used measure the mass flow rate of the gases, rather than the volumetric flow rate. This can be misleading, as the flow controllers and meters use and report liters per minute, but they are employing a correction factor to convert from the mass flow rate to these reported volume flow rates. The conversion factor used is based on the brand of the flow meter and the gas it was calibrated for. When the gas flowed is the same as the calibration gas, the correction factor is appropriate and the volume flow rate can be used directly. However, when a gas different than the calibration gas is flowed through the meter a correction factor must be applied, called the gas correction factor (GCF). Each manufacturer provides their own correction factors for a variety of gases, and applying the factor is as simple as multiplying the GCF with the measured volume flow rate. However, the situation becomes more complex when gas mixtures are considered. For example, MKS provides the eqn. 4.1 for computing the gas correction factor of mixtures.

$$GCF = \frac{0.3106(a_1 s_1 + a_2 s_2 + ... + a_n s_n)}{a_1 d_1 c_{p1} + a_2 d_2 c_{p2} + ... + a_n d_n c_{pn}} \tag{4.1}$$

Where 'a_n' is the fractional flows of gas 1 through n and 's_n' are the molecular structure factors, defined as 1.030 for monoatomic gases, 1.000 for diatomic gases, 0.941 for triatomic

gases, and 0.880 for polyatomic gases. The 'd_n' terms are the standard densities of the gases, and 'c_p' terms are the specific heats.

This somewhat complex relation between gas fraction and GCF becomes an issue when trying to determine the actual volume flow rate through the 5-lpm sample mass flow meter. Since the gas passing through the meter is a sample of either the intake or the exhaust, the exact concentration of each gas is not known and thus the GCF cannot be computed. However, without the volume flow rate it is not possible to determine the dilution fraction, and the Horiba readings cannot be converted to accurate volume fractions. The result is a cyclical problem which can be solved in two ways: 1) measure the volume flow rate of the sample using the wet test meter to determine the appropriate GCF, 2) use the Horiba readings and the mass flow rates measured to iteratively solve for the GFC and concentration of CO_2.

The drawback of the iterative solution is that is cannot account for all species involved, rather it assumes that the sample consists of only CO_2 and O_2. This is a reasonable estimate, but has a few short comings: 1) N_2 is present in the system but is not accounted for. At the concentrations we are dealing with it is a minor effect, as it ends up being counted as O_2, which is a similar molecule as far as the flow meter is concerned. 2) There are other trace species, including water and unburned hydrocarbons, which are not included. However, the species should be present in such small quantities as to not significantly effect the results.

The wet test meter has the advantage of providing a definite answer with no iteration, however its accuracy is dependent on many assumptions which are difficult to verify (intake temperature, water concentration in, water concentration out, water saturation level, etc.).

A third method, called the 'two point method' was also briefly used to determine the GCF. It was based on the concept of measuring 2 different dilution ratios at each sample point. Each dilution point could then be setup to solve for the CO_2 concentration, but each lacked the GCF. This resulted in a situation of 2 equations (the two different dilution points) and 2 unknowns (the CO_2 concentration and the GCF), and thus a solution of both could be solved for. The main advantage of this system was it did not depend on the accuracy of the mass flow meter, only the repeatability of it. However, the results were highly unstable, an error propagation analysis indicated that a 1% error in the flows and the Horiba readings would result in as much as a 27% error in the final result. Based on these findings the two point method was abandoned in favor of the other two, more stable techniques.

4.2 Intake Composition Analysis

All intake concentration measurements required the use of the dilution system described in section 2.5. Therefore, it was necessary to compute the actual compositions. The actual CO_2 concentration was determined using Eqn. 4.2, where $CO_{2-measured}$ is the measured CO_2 concentration with dilution, GCF is the gas correction factor (section 4.1), $\dot{V}_{sample}$ is the uncorrected volume flow rate of the sample measured with the 5-lpm mass flow meter, and $\dot{V}_{dilution}$ is the volume flow rate of the N_2 dilution gas. Any of the four other species

measured by the Horiba could be determined using this same equation and simply replacing the CO_2 terms with the species of interest.

$$CO_2 = CO_{2-measured} \frac{GCF \cdot \dot{V}_{sample} + \dot{V}_{dilution}}{GCF \cdot \dot{V}_{sample}} \tag{4.2}$$

The volumetric flow rates used in the the calculation were the time averaged values of the mass flow meter readings during the period of the sample. Because of the time delay associate with the gas traveling from the mass flow meters to the Horiba sensors, the mass flow data was shifted by 20 seconds to correspond more accurately. Note that the exact precision of the shift should not influence the reading as all samples were taken with the system at steady state, and the flow rates were constant both before and after the Horiba sample had concluded. Horiba samples were taken for a minimum of 60 seconds, and 90-300 seconds were preferred, with the length of the sample being inversely correlated to the the apparent stability of the system. This process was followed for both wet and dry EGR intake samples.

Since the Horiba test rack has no sensor for N_2, the N_2 in the intake cannot be measured. Instead, the flow rate of injected N_2 relative to the flow rate of injected O_2 is used to determine the volume ratio of N_2 to O_2 and once the O_2 concentration is known the N_2 concentration can be computed. When computing the N_2 concentration in wet EGR recirculated N_2 must also be included, which requires first knowing the EGR rate.

Re-hydration of Wet EGR Intake Composition

The wet EGR experiments included large amounts of water vapor in the intake oxidizer which had to be determined and adjusted for. This re-hydration process is based on the intake slipstream and condenser system, shown and described in section 3.2. The slipstream from the intake plenum being drawn through the condenser results in water building up in the collection container. The mass of this water is measured and recorded automatically, and can be used to determine the water collection rate using a best-fit line, as shown in Fig. 4.1. The collection rate in g/sec can be easily converted to mol/min. The average flow rate and GCF (computed using the wet test meter) for the 1-lpm flow meter were then computed and multiplied to determine the dry flow rate in standard -lpm, which was also converted to mol/min. Using Eqn. 4.3 the mole fraction, which is equivalent to the vapor fraction, of the intake oxidizer could be determined.

$$X_{H_2O} = \frac{\dot{n}_{H_2O}}{\dot{n}_{slipstream} + \dot{n}_{H_2O}} \tag{4.3}$$

Once the water vapor concentration of the intake oxidizer is known, the dry concentration of CO_2 can be corrected as shown in eqn. 4.4. O_2 and other intake species can be corrected using the same formula with the CO_2 valves replaced with their respective values.

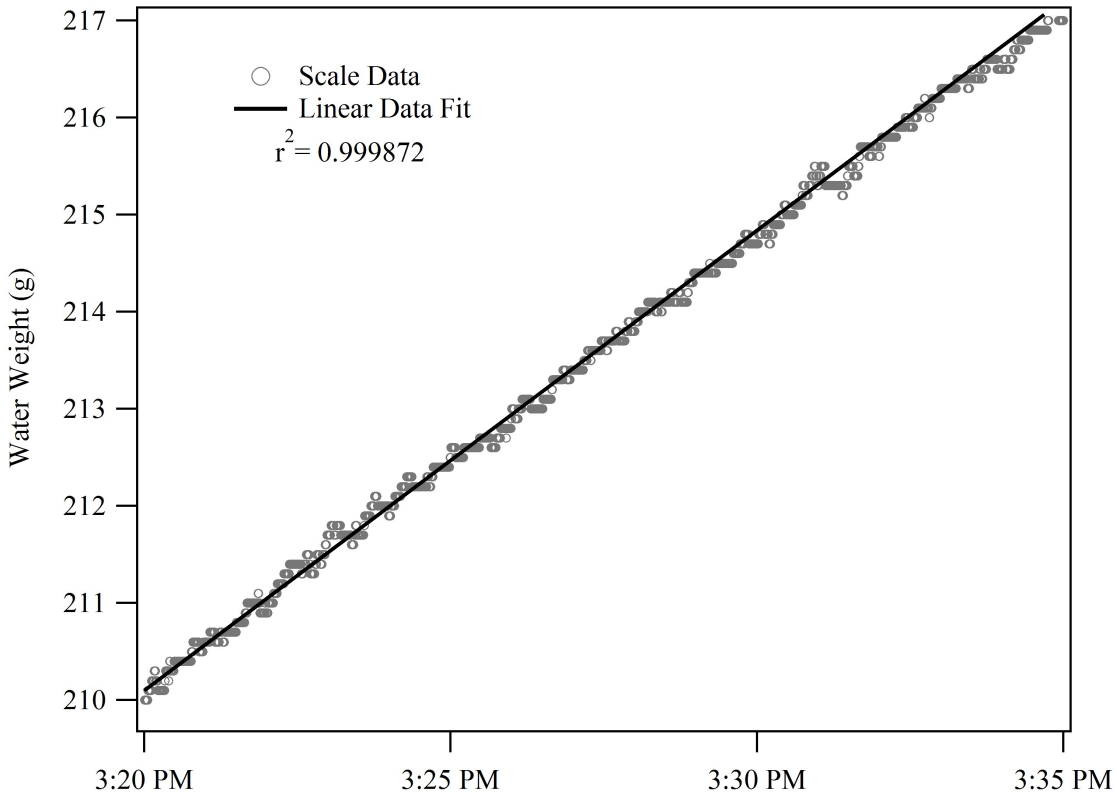

Figure 4.1: Raw scale data and a best fit line used to determine the water flow rate.

$$X_{CO_2} = X_{CO_2 Dry} \cdot (1 - X_{H_2O}) \tag{4.4}$$

4.3 EGR Flow Computation

The computation of the EGR flow rate is based on the known O_2 injection rate (set by a mass flow controller and measured with a redundant mass flow meter) compared to the measured O_2 concentration in the intake. For example, if 25-lpm O_2 is injected with no N_2, and the re-hydrated O_2 volume fraction is determined to be 25%, then the total EGR flow is estimated to be 75-lpm, and the total engine oxidizer flow rate is 100-lpm.

Additional complication exists due to the presence of unburned O_2 in the exhaust, which is recirculated to the intake, influencing the O_2 volume fraction measurement. In order to

account for this O_2, the injected O_2 is adjusted, resulting in the need to solve two equations with two unknowns: the EGR volumetric flow rate ($\dot{V}_{EGR}$) and the O_2 flow rate ($\dot{V}_{O_2}$).

$$\begin{aligned} \dot{V}_{O_2} =& \dot{V}_{O_2 Injected} + \dot{V}_{EGR} \cdot X_{O_2 Exhaust} \\ \dot{V}_{EGR} =& \frac{\dot{V}_{O_2}}{X_{O_2 Oxidizer}} - \dot{V}_{O_2 Injected} - \dot{V}_{N_2 Injected} \end{aligned} \tag{4.5}$$

Once the volumetric flow rate of EGR has been determined, the injected quantity of O_2 and N_2 can be added to determine total oxidizer flow rate. Finally, the measured fuel flow rate can be added to determine the total engine flow rate.

4.4 Performance Analysis

The indicated mean effective pressure (IMEP) and the brake power were both used to indicate engine performance. Fuel usage was measured and used to determine thermal and combustion efficiency.

Power Production

The IMEP was used to determine the power and efficiency of different test points. The IMEP was computed based on filtered in-cylinder pressure data (smoothed using a second-order Savitzky-Golay filter with a 19 point span), using the formula shown in Eqn. 4.6. Savitzky-Golay filtering was chosen for its ability to smooth the pressure traces while preserving local maximum (Savitzky and Golay 1964). With this method even knocking cycles can be filtered to a smooth curve without artificially raising or lowering the curve, as shown in Fig. 4.2. A minimum of 400 thermal cycles were averaged to determine IMEP values. From the IMEP the coefficient of variation (CoV) IMEP was also determined, which serves as an indicator of cycle-to-cycle variation.

$$IMEP = \frac{W_i}{V_s} = \frac{\int p_i \cdot dV}{V_s} \tag{4.6}$$

In addition to the IMEP, the brake power was also determined using a load cell mounted on a torque arm of the dynamometer. The load cell reported lbs force, which was recorded and could be multiplied by the torque are length and a conversion factor to determine the torque. The RPM was also recorded, which can be combined with the real-time torque to determine the brake power output. However, the CFR engine was built for robustness, not efficiency, and it was therefore necessary to determine the correlation between measured brake-power and the power computed using IMEP. Measured mechanical efficiency values are presented in Chapter 6 and compared to values of more traditional engines.

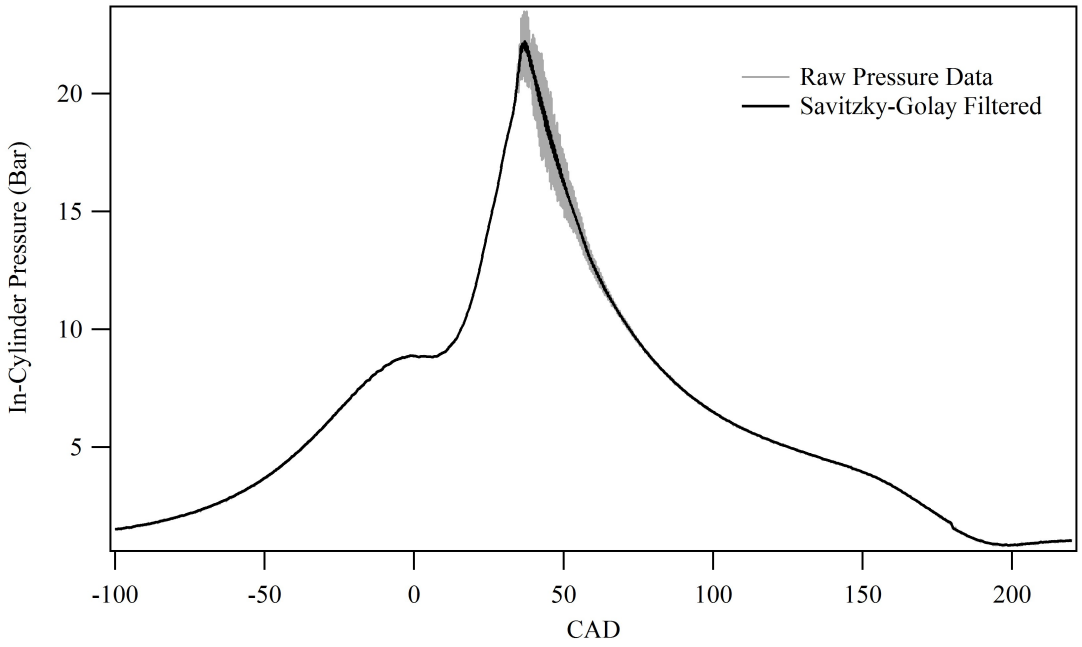

Figure 4.2: Raw pressure trace of a knocking cycle vs. Savitzky-Golay filtered curve.

Combustion Efficiency

Combustion efficiency, referring to the percentage of fuel combusted prior to exiting the cylinder, was computed using the formula shown in eqn. 4.7, where LHV is the lower heating value of the fuel. The HC-out is considered to be of the same heating value of the original fuel (note that the Horiba counts carbon atoms, not molecules, thus three carbons will be counted as one propane molecule, etc. This should increase the accuracy of the assumption, as the C to H ratio should be relatively constant). HC-in numbers were determined from fuel flow rate calculations (mass flow meter for methane, scale data for liquid), while CO and HC-out numbers were measured using the Horiba, and converted to per unit time by estimating the flow rate of the exhaust. For wet EGR the exhaust flow rate included all exhaust passing out of the engine, since the combustion efficiency is based on a simple in vs. out comparison. Therefore there was not adjustment for whether the exhaust returned to the intake via EGR, or exited the system.

$$\eta_{combustion} = 1 - \frac{\dot{N}_{CO} \cdot LHV_{CO} + \dot{N}_{HC-out} \cdot LHV_{HC}}{\dot{N}_{HC-in} \cdot LHV_{HC}} \tag{4.7}$$

NO_x Production

NO_x was determined in $g/(kW \cdot Hr)$ based on the measured NO_x ppm (including water vapor), the computed IMEP power, and the estimated flow rate of the exhaust. For wet EGR cases, this only included the portion of the exhaust which exited the system, and not the portion which recirculated to the intake. This is accurate as NO_x is measured as the amount leaving the exhaust relative to the power produced. Any NO_x which is recirculated is therefore not considered emissions. Note that this does not provide an unfair advantage to wet EGR as the recirculation of the EGR includes NO_x, and thus NO_x concentration in PPM are much higher for wet EGR cases than cases which do not recirculate.

Knock Indicator

The knock indicator used in this study uses the in-cylinder pressure measurement to determine the Maximum Amplitude of Pressure Oscillation (MAPO) as well as the Integral of Modulus of Pressure Oscillation (IMPO) (Brecq, Bellettre, and Tazerout 2003). The MAPO method is based on the largest amplitude pressure wave in a knocking cycle, while the IMPO method is based on the energy of the high frequency pressure fluctuations that typically occur during knocking combustion. The amplitude of the fluctuations is strongly linked to the amount of end-gas that undergoes autoignition. The chamber frequency has to be known and can be determined by solving the wave equation (Scholl et al. 1998). For both indicators, the signal is band-pass filtered from 5-11kHz, based on the calculated chamber frequency. The filtered data is then rectified, and the highest point of this curve represents the value of the MAPO. For IMPO, the filtered pressure data is rectified and integrated to compute the IMPO, as shown in Fig. 4.3.

A knock indicator is programmed into the Labview program which is used for acquiring pressure data from the system and provide real-time indication of knock intensity while operating. This is a rough method which helps determine which data points should be tested while running the engine. Official knocking data used for analysis is performed using the same procedure, but in an external code which filters the data and looks at a minimum of 400 thermal cycles when determining intensity and frequency of knocking.

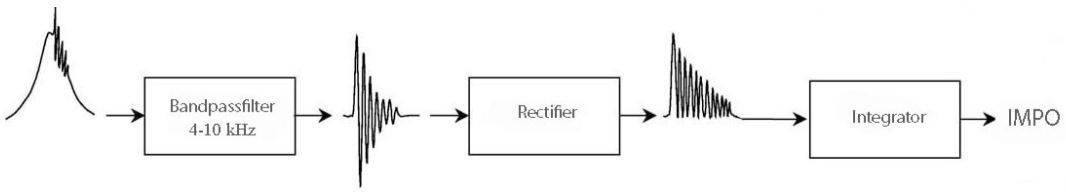

Figure 4.3: Diagram indicating the process of determining the IMPO value.

Chapter 5

Thermal and Chemical Properties of EGR

The thermal and physical properties of wet and dry EGR were evaluated as they relate to laminar flame speed. It is widely published that the flame speed in pure CO_2 diluent is significantly reduced relative to air, but the effect of including large quantities of water vapor are not well published. In this chapter the laminar flame speeds of wet and dry EGR are compared to air, with results indicating that even with 25% O_2 concentration the laminar flame speed in wet EGR drops by a factor of 2, and in dry EGR drops by a factor of 4. As reported in the literature, CO_2 is found to have significant negative chemical effects while water is shown to be relatively inert. Thermal effects are analyzed and it is shown that water has a significantly higher thermal diffusivity than CO_2, which is directly related to the laminar flame speed.

5.1 Laminar Flame Speed

Laminar flame speeds were calculated using the GRI 3.0 mechanism for wet EGR, dry EGR, and N_2 working fluids to better understand the difference in engine performance. All calculations were carried out for stoichiometric CH_4 with the oxidizers listed in Table 5.1. Results are presented in Fig. 5.1.

The computed flame speed in dry EGR drops by more than a factor of four compared to air despite 25% oxygen by volume, in agreement with previous flame speed investigations (Herbst et al. 2011). Surprisingly, the wet EGR case showed a dramatically increased flame speed relative to the dry EGR case. As described below, this difference is the result of H_2O displacing CO_2 in the working fluid.

Table 5.1: Oxidizer mole fractions and laminar flame speed comparison at 10 atm and 700K.

Case	Air	Dry EGR	Wet EGR
Oxidizer Mole Fractions			
O_2	0.21	0.25	0.25
CO_2	0.00	0.75	0.24
H_2O	0.00	0.00	0.48
N_2	0.79	0.00	0.03
Laminar Flame Speed			
$S_L[cm/s]$	86.6	18.7	48.6

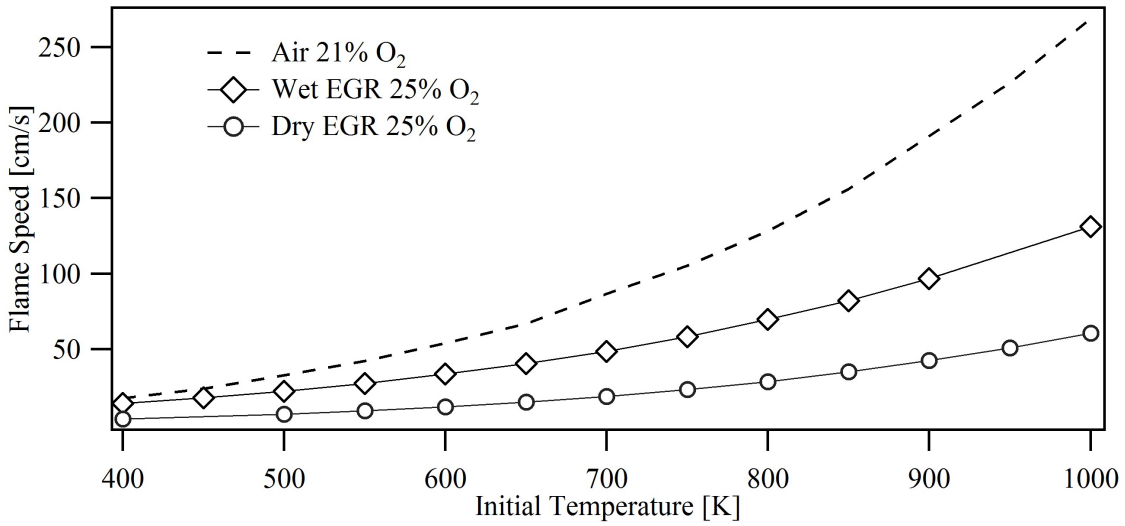

Figure 5.1: Laminar flame speed of stoichiometric CH_4 and oxidizer at 10 atm.

Chemical Effects

Additionally, flame speeds were calculated using chemically inert H_2O and CO_2 in the working fluid, thereby isolating thermal and physical effects (Table 5.2). In this method, the molecules retained their thermal and physical properties, but no longer participated in their respective kinetic reactions. The inert molecules still interacted as third bodies, but without the increased efficiency that has been found for CO_2 or H_2O in some chemical reactions (Davis et al. 2005). For confirmation of trends and relative magnitudes, flame speeds were also computed using mechanisms by Konnov (2009) and Miller and Bowman (1989). All mechanisms predicted equal trends and similar magnitudes, with Konnov and Miller predicting slightly higher flame speeds than GRI 3.0 for all cases.

Comparing run A and B shows working fluid CO_2 has significant kinetic interactions,

Table 5.2: Flame speed calculation results. Dry EGR cases mole fractions in oxidizer: O_2 = 0.28, CO_2 = 0.66, N_2 = 0.05, H_2O = 0.0; EGR cases mole fractions in oxidizer: O_2 = 0.28, CO_2 = 0.22, N_2 = 0.05, H_2O = 0.44; All calculations were performed at a pressure of 10 atm and an initial temperature of 700K.

	Mechanism	GRI 3.0	Konnov	Miller
Run	*Dry EGR Cases*		$S_L[cm/s]$	
A	Active CO_2	33.8	41.1	40.4
B	Inert CO_2	59.6	63.2	71.6
	Wet EGR Cases			
C	Active H_2O & CO_2	72.8	76.1	81.0
D	Inert H_2O	74.4	83.4	86.0
E	Inert CO_2	82.8	87.7	96.3
F	Inert H_2O & CO_2	96.4	102.0	108.5

with run A predicting lower flame speeds for all mechanisms. Even for EGR cases, which have a much lower CO_2 concentration, the predicted flame speed in run C with active CO_2 is significantly decreased relative to run E with inert CO_2; by over 14% in all mechanisms. Clearly CO_2 has a significant kinetic interaction even at a mole fraction of 22%. This is largely believed to be the effect of reactions such as the one shown in Eq. 5.1, which previous research has found significantly reduces the laminar flame speed (Yossefi et al. 1995; Liu, Guo, and Smallwood 2003; Walton et al. 2007).

$$CO + OH \leftrightarrow CO_2 + H \tag{5.1}$$

Water shows a much smaller chemical interaction. Das, Kumar, and Sung (2011), reported that a small amount of water in the fuel increased flame speed due to the positive chemical effects of H_2O for syngas. However, it was shown for increased concentrations of water, that the minor positive kinetic effect was dominated by the negative thermal effect. Comparing run D with inert H_2O to run C with active H_2O shows that all mechanisms predicted a relatively small decrease in flame speeds when the H_2O in the working fluid (in large concentration) interacts chemically. This suggests H_2O has only a small chemical effect, which is desirable when compared to the large negative chemical effect of CO_2. There was a large increase in flame speed in case F, when both H_2O and CO_2 were made inert. This indicates that CO_2, and to a lesser extent H_2O, inhibit the flame chemistry. The main effect of H_2O is high third-body efficiency on chain-terminating reactions (Davis et al. 2005; Seiser and Seshadri 2005). Thus, it is the lack of any efficient third-body molecules that produce the large increase in flame speed, and not a direct chemical interation of water. The main effect of CO_2 is in its direct influence on chemical reactions, because in additional computations, a variation of the third-body efficiency of CO_2 has shown to be of small importance.

Thermal Effects

In addition to its chemical advantage, H_2O has a thermal advantage over CO_2 based on the more than 50% increase in flame speed computed in run F compared to run B. This thermal difference is the result of the lower specific heat (C_P) and higher thermal diffusivity (α) of H_2O relative to CO_2 shown in Fig. 5.2.

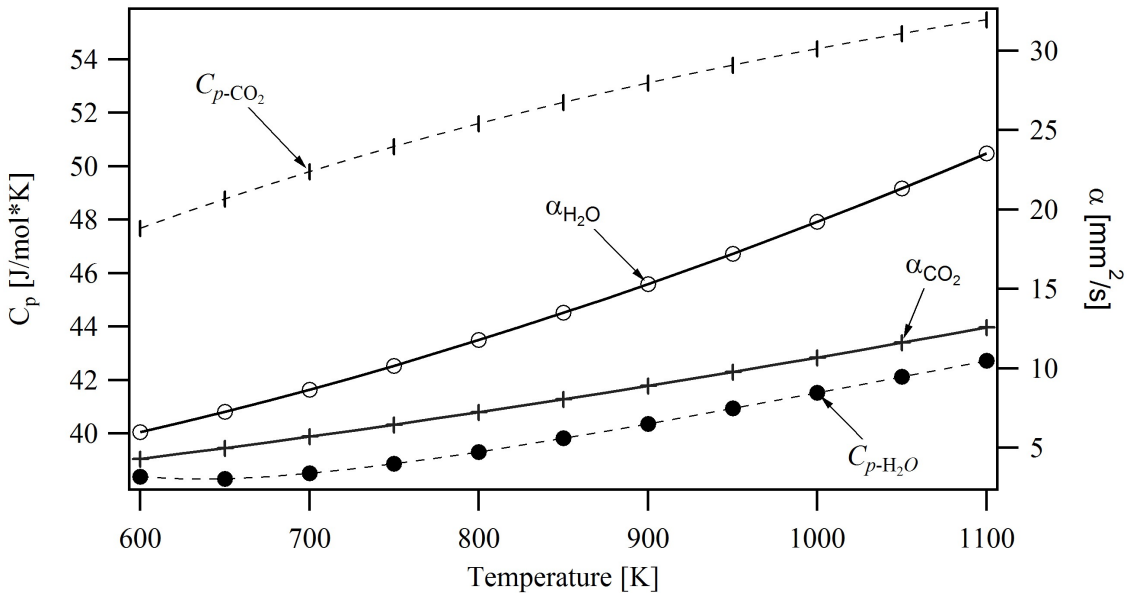

Figure 5.2: Thermal properties of H_2O and CO_2.

On a molar basis, the C_P of H_2O is around 20% lower than that of CO_2, resulting in an approximately 10% reduction of the mixture C_P. This will increase the flame speed slightly due to an increased temperature. However, the majority of the increase in flame speed is a direct result of the significantly higher α of H_2O, which is directly related to flame speed as seen in Eqn. 5.2 from simple thermal theory:

$$S_L \sim \left(\frac{\alpha}{\tau}\right)^{1/2} \tag{5.2}$$

where τ represents the characteristic time of reaction at a given temperature.

Conclusions

The laminar flame speeds of methane combustion in wet and dry EGR with 25% O_2 have been compared to methane-in-air. It was found that the laminar flame speed of wet EGR is roughly half that of air, and dry EGR has a flame speed only roughly 1/4 that of air. The difference

in flame speeds between wet and dry EGR was shown to be the product of both chemical and thermal effects. CO_2 has significant negative thermal effects, while water is relatively inert. In addition, water has a slightly lower specific heat than CO_2 (on a molar basis), and a significantly higher thermal diffusivity than CO_2, both of which contribute to faster flame propagation. In conclusion, the addition of water improves the combustion properties of the working fluid, and should therefore be considered when designing oxycombustion system.

Chapter 6

CFR Mechanical Efficiency

In this chapter, the mechanical efficiency of the CFR engine is evaluated to determine the validity of generalizing brake-measurements (power, thermal efficiency, NO_x, etc.) to other, more modern and specialized engine designs. This is particularly applicable to the reporting of emissions production, which is typically regulated in g/kWh. The robust design of the CFR, including additional rings and a long piston skirt which add friction and an over-bored cylinder head which increases blow-by, leads to significantly larger motoring losses than traditional engines. In addition, when considering losses in a traditional engine all peripheral belt-drive components necessary for operation, such as the alternator and coolant pump, are included, while on the CFR these systems are all externally powered and therefore not part of the brake power measurement. It was found that the increased losses due to robust design and the gained efficiency from the omission of critical systems such as the alternator and the coolant pump largely offset eachother, resulting in the total brake efficiency being reasonably close to a modern engine. It is concluded that 600 RPM, brake-power comparisons between the CFR and a traditional engine can be made with reasonable tolerances.

6.1 Theory of Friction and Pumping Losses

Friction in engines primarily stems from the sealing surface between the piston and the cylinder wall, called 'rings', which must have a very tight fit and exert significant force on the cylinder wall in order to minimize pressure losses. As the piston moves relative to the cylinder wall, the friction forces consist of 3 main types: 1) independent of speed, 2) proportional to speed, 3) proportional to speed squared. Thus the friction work for a cycle can be defined in the form of Eqn. 6.1, where N is the engine speed in revolutions per minute (Heywood 1988).

$$\text{TFMEP(bar)} = C_1 + C_2 N + C_3 N^2 \tag{6.1}$$

Heywood (1988) defines the true measurement of friction in a firing engine to be determined by subtracting the brake power from the indicated power determined from accurate measurements of cylinder pressure throughout the cycle. This combines the effects of rubbing friction mep (rfmep) and all external engine loads (i.e. alternator, water pump, oil pump) into a single total friction mep (TFMEP) for the engine. Other methods of estimating the friction include: 1) 'direct motoring tests,' in which the motor is turned by an external motor, and the power requirement is measured. 2) 'Willans line,' which plots fuel consumption versus brake output and extrapolates to no fuel injection to determine motoring friction (for diesels). 3) 'Morse test,' in which individual cylinders are cut from firing and the reduction in brake torque is determined while maintaining engine speed. However, each of these 3 techniques only estimates friction losses in non-firing (motoring) conditions, which is different than firing friction losses for the following reasons: 1) Rubbing friction increases with pressure, which are higher when firing. 2) Temperatures of piston and cylinder are higher when firing, which affects lubrication viscosity and reduces piston-cylinder clearances. 3) When motoring there is no exhaust blow-down phase, which can result in different pumping work. 4) Work is done during motoring due to heat losses from the gas to the walls and gas losses through blowby, but this work is not part of the true total friction of the engine. Since the CFR is spark ignited and single cylinder only the first motoring friction estimation technique would be possible to attempt. However, since the engine is equipped to measure both IMEP and BMEP there was not reason to use any motoring estimation, instead the 'true' friction losses were determined.

In his book, Heywood (1988) presents TFMEP data measured for several four-stoke engines over a wide range of engine speeds at wide-open throttle. The data is well correlated using the coefficients in Eqn. 6.2. Correlating this to experiments performed in this study; at 600rpm the predicted TFMEP is 1.078 bar.

$$\text{TFMEP(bar)} = 0.97 + 0.15\left(\frac{N}{1000}\right) + 0.05\left(\frac{N}{1000}\right)^2 \tag{6.2}$$

6.2 Results

The TFMEP was computed for experimental runs by subtracting the BMEP, based on the measured brake power (based on the load cell torque shown in Fig. 2.2 and the rpm), from the IMEP, determined from the in-cylinder pressure trace. Note that external engine loads, with the exception of the mechanically driven oil pump, are not included since they are electronically driven in our experiment. Results are shown in Fig. 6.1 versus the IMEP. While there is a significant amount of spread, the TFMEP is relatively constant across all power levels. The average value is only slightly elevated when compared to the curve fit proposed in Heywood (1988), and appears to fit within the range of measured data presented. There is not a clear trend between CR and TFMEP, though CR 12 does appear to be slightly

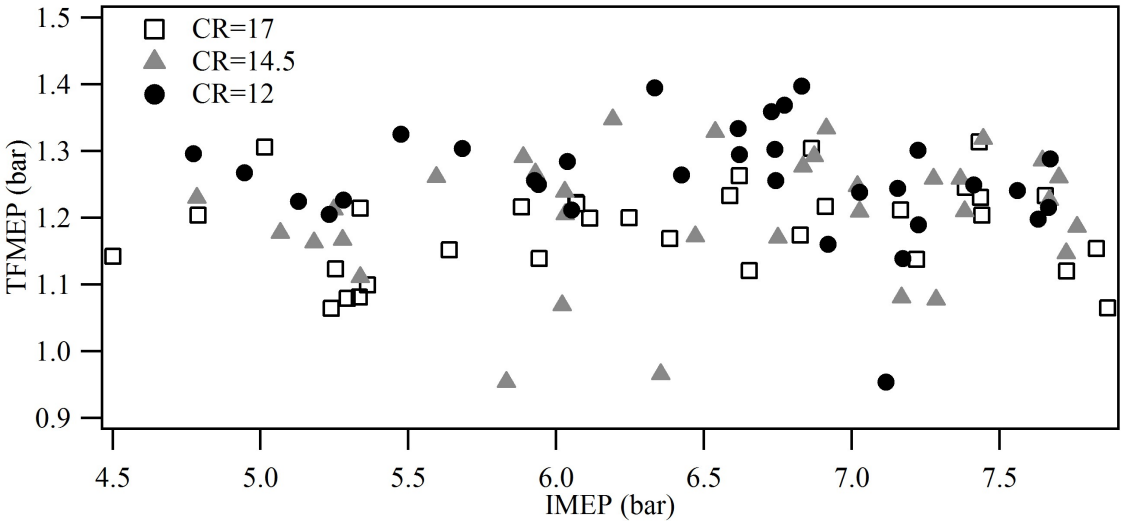

Figure 6.1: The TFMEP at three different CRs.

lower than CR 17 on average. It is expected that as the CR increases the TFMEP would also increase, primarily due to increased rubbing friction, but Heywood shows that the difference due to CR is reduced at low BMEP levels, approaching zero for the lowest power level cases.

The mechanical efficiency was computed as shown in Eqn. 6.3. Data from all experiments were included, with data from wet EGR, dry EGR, and air runs.

$$\eta_{mech} = \frac{P_{brake}}{P_{indicated}} \tag{6.3}$$

Computed mechanical efficiency values are shown in Fig. 6.2 relative to the IMEP value for each point. As expected, there is a fairly linear correlation between load and mechanical efficiency. Surprisingly, the mechanical efficiency is reasonable, and comparable to many modern engines despite the robust design of the CFR (Mahalec, Lulic, and Skok 2001). This is believed to be primarily a result of the traditional definition of brake power, which requires that all elements necessary for engine operation must be included. The results is that the the extra friction of the CFR essentially takes the place of traditional peripheral equipment losses, and the net outcome is an engine with reasonable mechanical efficiency at 600rpm.

6.3 Conclusions

It was found that at 600 RPM, the CFR produces mechanical efficiency values reasonably similar to modern engines, making brake-power comparisons reasonable. The result was not dependent on the working fluid being tested. The similarity between the CFR and a traditional engine is a result of the higher in-cylinder friction losses of the CFR counteracting the

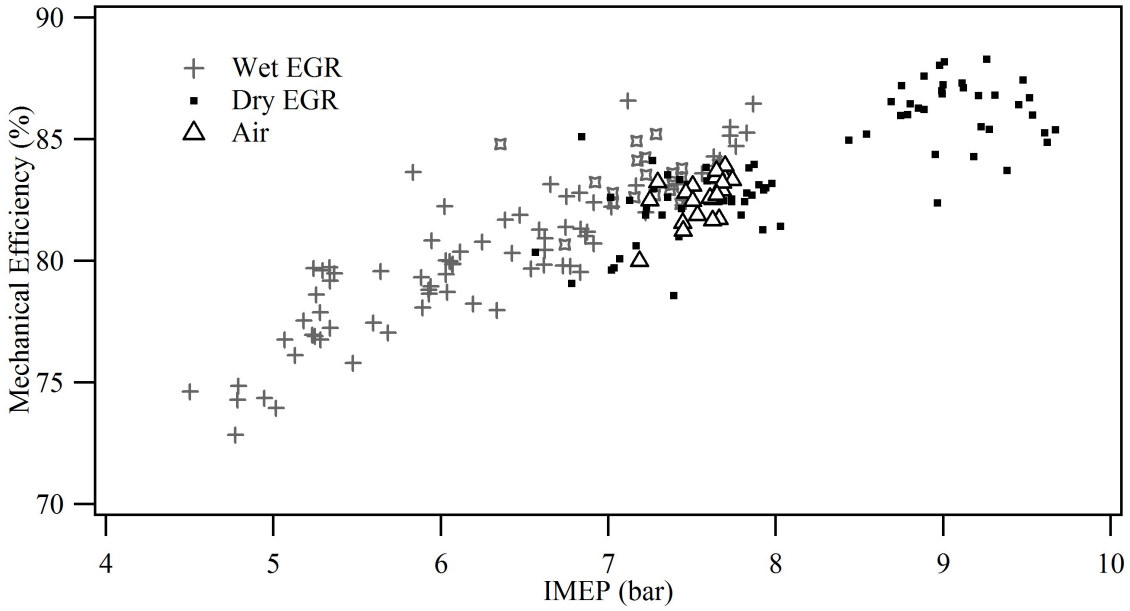

Figure 6.2: Mechanical efficiency of the CFR engine versus IMEP for a variety of working fluids and power conditions.

lack of engine-driven peripherals which are included in the mechanical losses of a traditional engine. The high in-cylinder losses of the CFR are attributed to its robust design, which include additional rings and a long piston skirt which add friction and over-bored cylinder head which increases blow-by. However, on the CFR peripheral equipments such as the alternator, coolant pump, and fuel pump are all externally driven, thus removing loads which normally reduce the mechanical efficiency of a traditional engine. Given these results, it is reasonable to report engine out emissions in g/kWh brake without significant biasing.

Chapter 7

Performance Limits of Methane Oxycombustion

This research experimentally investigates the performance of a spark-ignited (SI) internal combustion engine under methane (CH_4) fuel oxycombustion conditions and compares the results to methane-in-air performance. The main performance characteristics that are experimentally investigated in this work are: 1) thermal efficiency, 2) combustion efficiency, and 3) Coefficient of Variation (CoV) of Indicated Mean Effective Pressure (IMEP). Thermal efficiency is based on IMEP values and the lower heating value of the injected methane. Combustion efficiency is computed by evaluating the energy of the carbon monoxide (CO) and unburned hydrocarbons in the exhaust relative to the energy of the injected fuel. Blow-by of the cylinder gases past the piston rings is not accounted for when computing the combustion efficiency. The experimental work was performed with two different working fluids: wet EGR and dry EGR. Multiple O_2 concentrations were tested for both working fluids, with all runs performed at a stoichiometric air-fuel mixture. Compression ratio (CR) and spark-timing sweeps were performed for each test, with a maximum CR of 17 and a maximum spark advance of 60°BTDC. In addition, the CR and spark-timing sweeps are performed with methane-in-air combustion using the same engine conditions as a performance reference.

7.1 Tested Compositions

Tests were performed with five different O_2 concentrations for wet EGR, and four different O_2 concentrations for dry EGR. Tables 7.1 and 7.2 show the measured intake oxidizer compositions for wet EGR and dry EGR tests, respectively. The dilution system has a 2% margin of error, resulting in some reported values exceeding 100%. Upper and lower O_2 limits were chosen such that the local maximum of thermal efficiency was spanned. In addition to the oxycombustion tests, a standard air combustion test was performed to obtain a reference performance.

All nine O_2 concentration tests were run at CRs of 12, 14.5, and 17, and at each CR a

Table 7.1: Wet EGR intake compositions tested.

Case	O_2	CO_2	Water	N_2	Total
Wet EGR 1	23.7%	24.1%	49.1%	2.11%	99.5%
Wet EGR 2	26.4%	23.1%	47.7%	2.07%	99.8%
Wet EGR 3	29.3%	22.3%	45.4%	2.06%	99.3%
Wet EGR 4	32.9%	20.5%	43.6%	1.89%	99.2%
Wet EGR 5	36.7%	19.0%	41.2%	1.98%	99.1%

Table 7.2: Dry EGR intake compositions tested.

Case	O_2	CO_2	N_2	Total
Dry EGR 1	25.7%	69.1%	3.1%	98.0%
Dry EGR 2	28.0%	68.8%	3.2%	100.0%
Dry EGR 3	32.7%	63.9%	3.5%	100.1%
Dry EGR 4	35.4%	61.1%	3.5%	100.0%

Table 7.3: The tested CR and corresponding spark-timings for the case 'dry EGR 3'.

CR	Spark-Timings (°BTDC)					
17	20	23	26	29	32	
14.5	20	25	28	31	34	
12	20	24	27	30	33	36

spark-timing sweep was performed which spanned the maximum torque and peak thermal efficiency point. The air test was performed at CRs 12, 14, 16, and 17 with the same spark-timing sweep methodology.

7.2 Data Analysis Technique

A sample case, Dry EGR 3 (Table 7.2), will be presented to illustrate the techniques used to produce the results. The spark-timings tested for each CR are listed in Table 7.3.

Thermal efficiency was determined for each spark-timing tested, as shown in Fig. 7.1. A third-order polynomial was fit to each CR curve to determine the maximum thermal efficiency and corresponding spark-timing.

The combustion efficiency was also determined for each spark-timing, as shown in Fig. 7.2. A best-fit line was created for each CR, and the combustion efficiency corresponding to the maximum thermal efficiency spark-timing was determined. For dry EGR cases, the

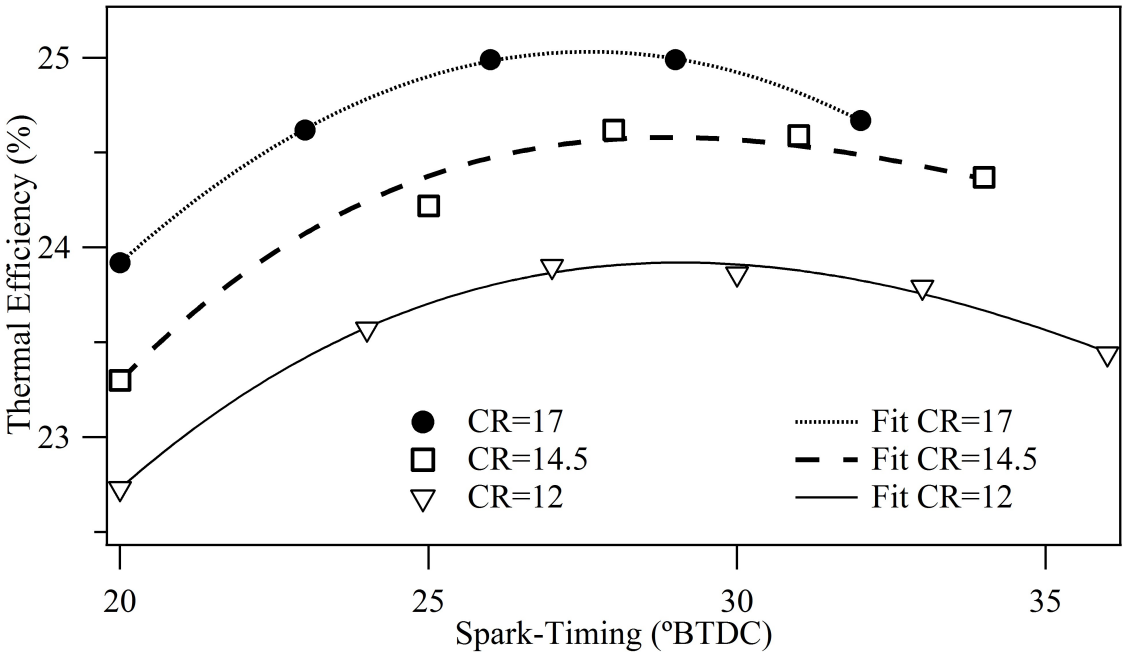

Figure 7.1: Measured thermal efficiency at each CR and corresponding spark-timings for the case 'dry EGR 3'.

experimental variability appeared quite high, indicating somewhat unstable combustion. Note that both CR and spark-timing had very little effect on the combustion efficiency. This trend was observed for all working fluids and O_2 concentrations.

The measured CoV IMEP values are shown in Fig. 7.3. Due to the low noise level and strong inverse correlation between CoV IMEP and maximum efficiency, the minimum measured CoV IMEP value of each CR curve was used rather than creating a best fit curve.

Using the described techniques, the spark-timing, combustion efficiency, and CoV IMEP corresponding to the peak thermal efficiency were determined and are shown in Table 7.4. Equivalent computations were carried out for all working fluids, O_2 concentrations, and CRs, including air. The combined results are presented graphically in the next section.

7.3 Results

The maximum thermal efficiency achieved at CR 17 for each case is plotted in Fig. 7.4. While it is clear that methane-in-air shows substantially higher thermal efficiency than any EGR case regardless of conditions, there are several interesting aspects of the EGR curves. Tests span the O_2 concentration corresponding to the peak thermal efficiency for both wet and dry EGR, and both cases required significantly more than the 21% O_2 concentration in

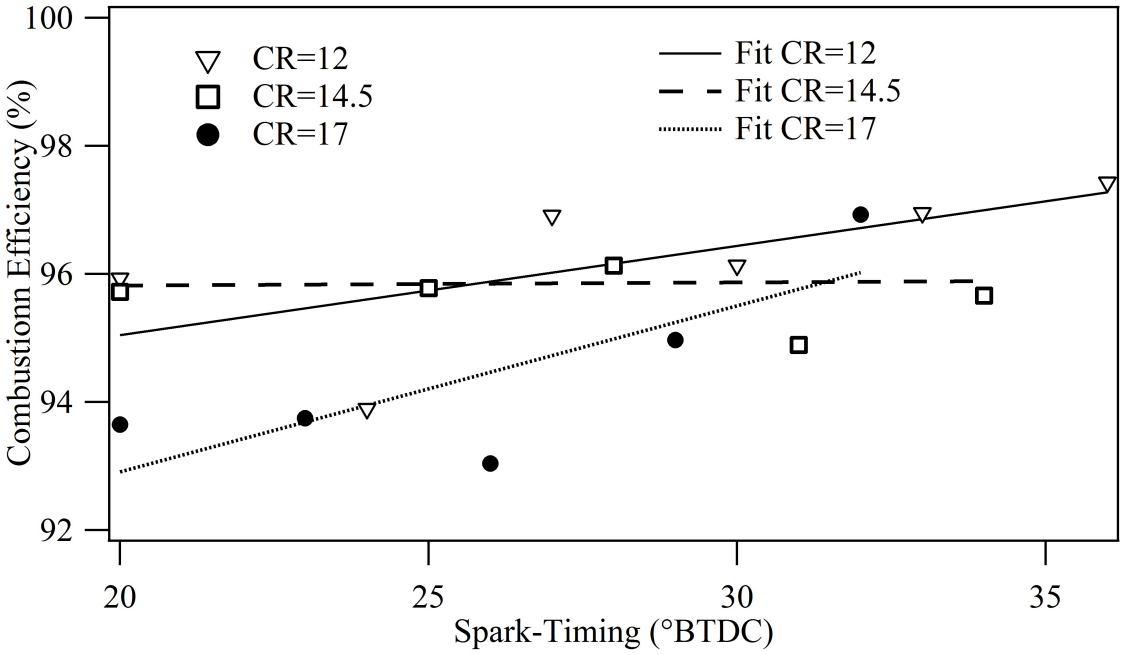

Figure 7.2: The combustion efficiency at each CR and corresponding spark-timings for the case 'dry EGR 3'.

Table 7.4: Tested CR and corresponding maximum thermal efficiency spark-timings for the case 'dry EGR 3'.

CR	12	14.5	17
Spark-Timing (°BTDC)	29.1	29.5	27.6
Thermal Efficiency (%)	23.9	24.6	25.0
Combustion Efficiency (%)	96.3	95.9	94.9
CoV IMEP	1.15	1.37	1.45

air. Relative to dry EGR, wet EGR shows a slightly lower maximum thermal efficiency, and it occurs at a slightly lower O_2 concentration.

Additional insight can be gained from plotting the peak efficiency of each case across compression ratios. The results of the wet EGR cases are shown in Fig. 7.5, with each group of connected data points representing a single O_2 concentration, and each data point representing the peak efficiency at a given CR. The filling of the marker indicates the compression ratio: CR 17 points are solid black, CR 14.5 points are solid grey, and CR 12 points are white with a black outline. As expected, for all curves the CR 17 point is at the top left, and the CR 12 point is in the bottom right. Observing the individual curves it appears that the

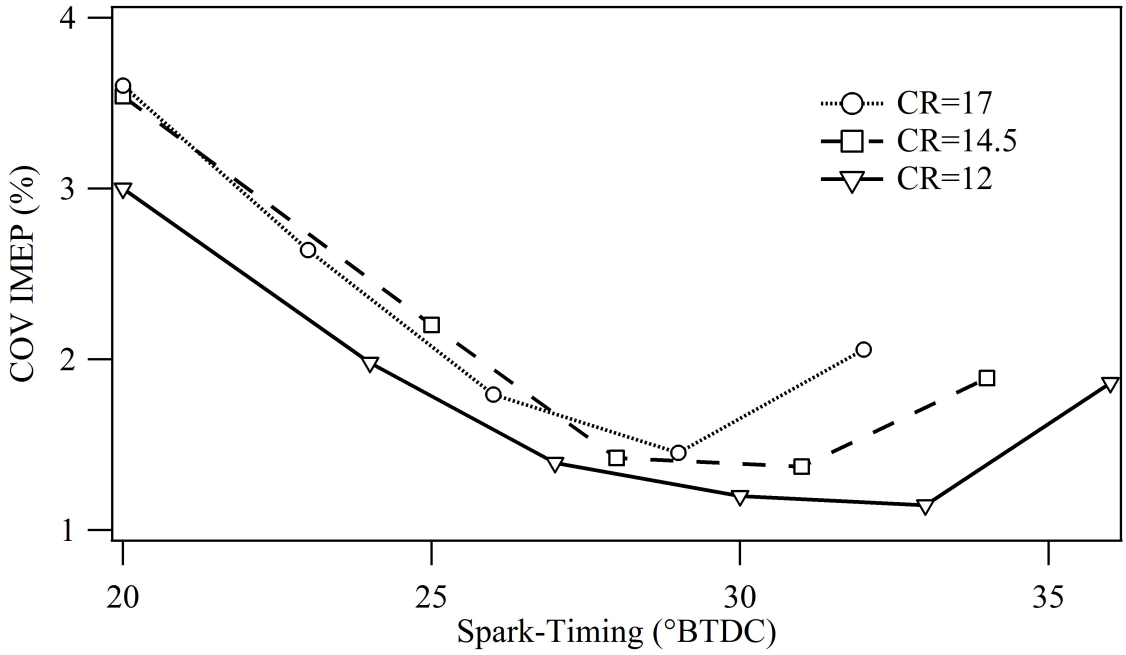

Figure 7.3: The CoV IMEP at each CR and corresponding spark-timings for the case 'dry EGR 3'.

CR has an increasingly significant effect on thermal efficiency at higher O_2 concentrations. This effect is discussed in combination with the heat release curves later in this section.

For comparison, Fig. 7.6(a) shows the same information as Fig. 7.5 but with dry EGR and air cases included. The same trend as was seen in Fig. 7.5 holds true for all cases, with CR 17 results occurring at the top left of each connected group, and CR 12 results occurring at the bottom right. Comparing the EGR cases to air it is immediately obvious that CR has a relatively minor effect; even at a CR of 12 air produced a much higher thermal efficiency than any EGR case.

Figure 7.6(b) shows the peak indicated power corresponding to the thermal efficiency points in Fig. 7.6(a). Since the engine is unthrottled for all cases, the indicated power for each working fluid primarily shifts as a function of oxygen concentration. The lower power of Wet EGR cases relative to dry EGR cases is a result of reduced engine flow due to the lower average intake pressure and the elevated intake temperature. Wet EGR cases had approximately a 10% reduction in engine flow rate compared to air and dry EGR cases.

Theoretical Thermal Efficiency

The primary reason for the reduced thermal efficiency of EGR vs. air is the lower ratio of specific heats (γ) of the EGR cases (1.23 for wet EGR, 1.21 for dry EGR) relative to air (1.30). For both the wet and dry EGR cases, the range of O_2 concentrations tested resulted

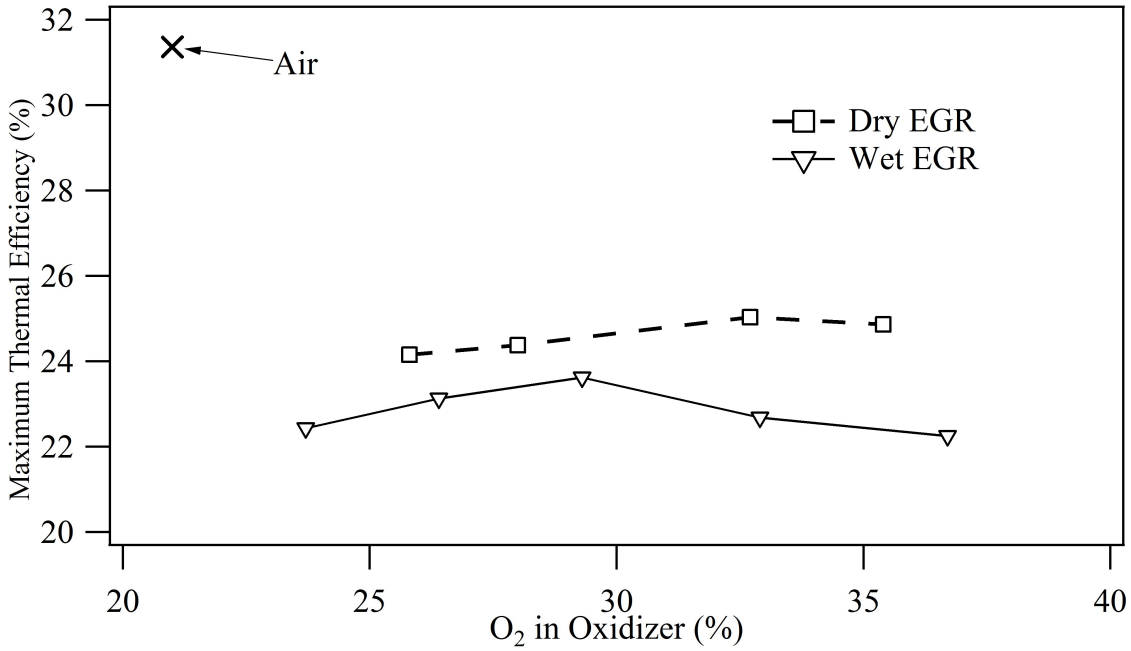

Figure 7.4: Peak thermal efficiency vs. O_2 concentration for CR=17 (CR=17 produced the highest thermal efficiency for all cases).

in a total change in average gamma of less than 0.005. The values were computed based on the measured intake compositions and modeling the combustion process using the pressure curve to predict the combustion rate. The γ values predicted throughout the combustion process are shown in Fig. 7.7. Reported γ values are the averages of the individual curves.

The thermal efficiency of the ideal Otto cycle (theoretical thermal efficiency) was computed using Eqn. (7.1), for a range of CRs from 9 to 17 (Fig. 7.8).

$$\eta_{ideal} = 1 - \frac{1}{CR^{(\gamma-1)}} \tag{7.1}$$

Observing Fig. 7.8, in the range of g values tested, reducing γ by 0.1 results in a much larger decrease in theoretical efficiency than reducing the CR from 17 to 12. When γ is reduced from 1.30 (methane-in-air) to 1.21 (dry EGR) the thermal efficiency of the ideal Otto cycle is reduced from 57.3% to 44.8%, which is a reduction of 21.8% ($57.3 \times 0.782 = 44.8$). Correlating this with experimental results, the maximum experimental thermal efficiency of air is 31.4%, which when reduced by 21.8% results in 24.6%, which is very close to the measured efficiency of 25.0%.

Wet EGR, with a γ of 1.23, corresponds to a theoretical thermal efficiency of 47.9% at CR 17; a reduction of 16.4% relative to the 57.3% of air. However, the experimental thermal efficiency of air reduced by 16.4% is 26.3%, which when compared to wet EGR is significantly higher than the measured maximum thermal efficiency of 23.6%. Similarly, the higher γ of

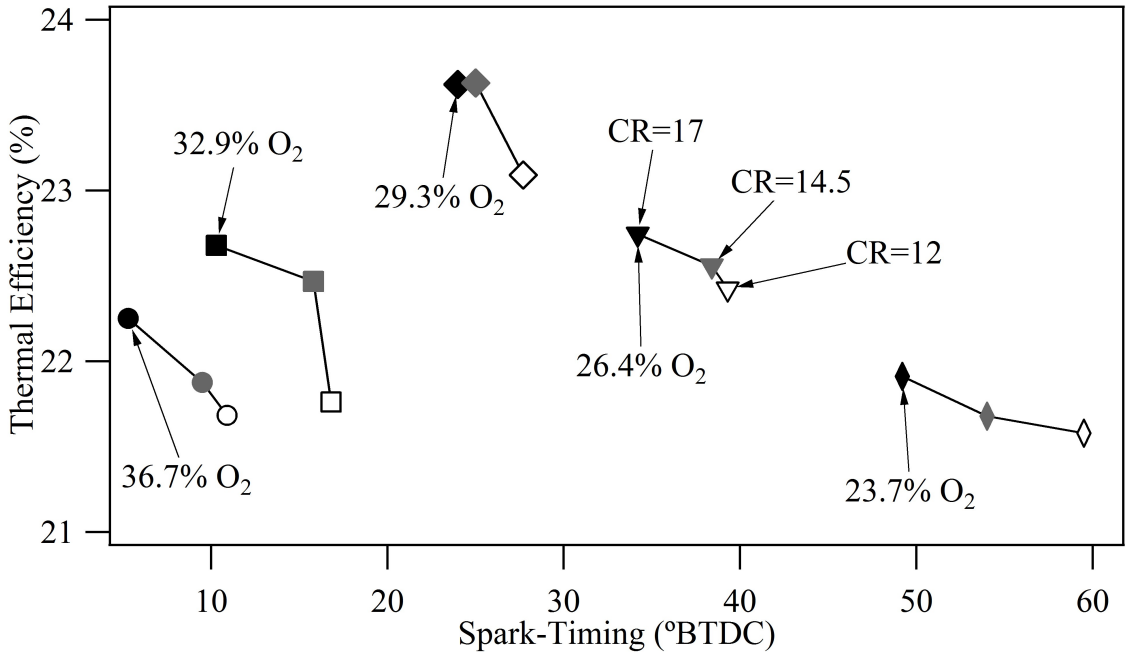

Figure 7.5: Peak thermal efficiency of wet EGR for each CR tested.

wet EGR relative to dry EGR corresponds to a 3% higher theoretical thermal efficiency for wet EGR at CR 17, but dry EGR produced slightly higher experimental thermal efficiency than wet EGR across all O_2 concentrations.

For an engine to have equivalent theoretical efficiency for wet EGR and air, it would require operating at CR 17 for wet EGR, and at CR 9 for air. The situation is even more extreme for dry EGR, and would require air to operate at a CR of approximately 7.25 to match the 44.8% theoretical thermal efficiency of dry EGR at CR 17.

Heat Release Profiles

Figure 7.6 shows another interesting result; all three working fluids produce maximum efficiency at a spark-timing in the 20-30°BTDC range. Observing the O_2 concentrations at the maximum thermal efficiency, the O_2 volume fractions of 21%, ∼30%, and ∼32%, corresponding to air, wet EGR, and dry EGR respectively, increase as the laminar flame speed of the working fluid (under equivalent O_2 concentrations) decreases. This inverse correlation results in all three maximum thermal efficiency cases having nearly identical normalized heat release curves (Fig. 7.9).

Rate of heat release is calculated from the averaged cylinder pressure over 400 cycles, and is based on the method presented in Heywood with the thermodynamic properties of the gas calculated by the NASA polynomials (Heywood 1988). The calculation includes the

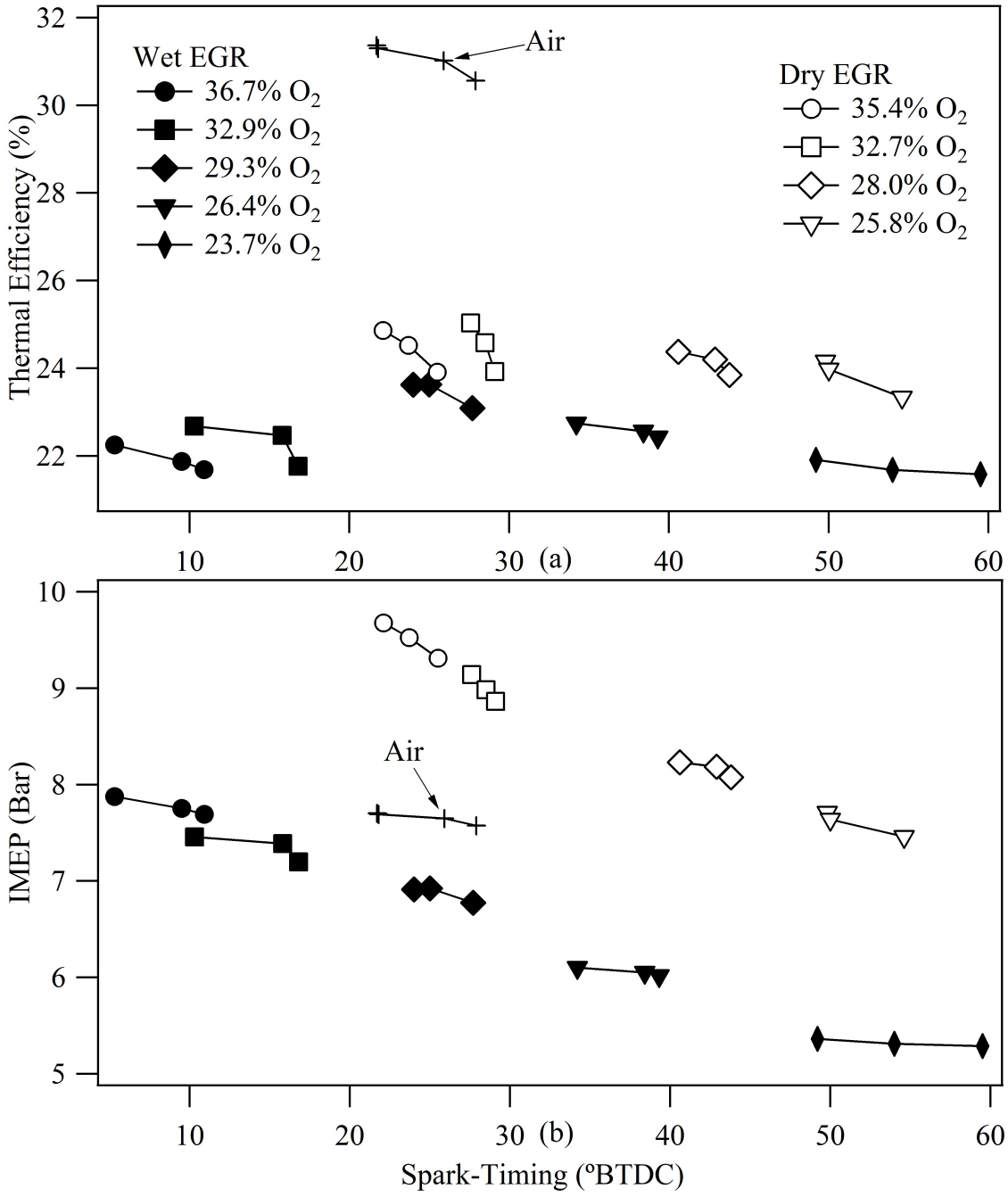

Figure 7.6: Peak thermal efficiency of wet EGR, dry EGR, and air. Connected points are the peaks measured at different CRs for the same O_2 concentration.

wall heat losses which are calculated by a Woschni correlation for convective heat transfer

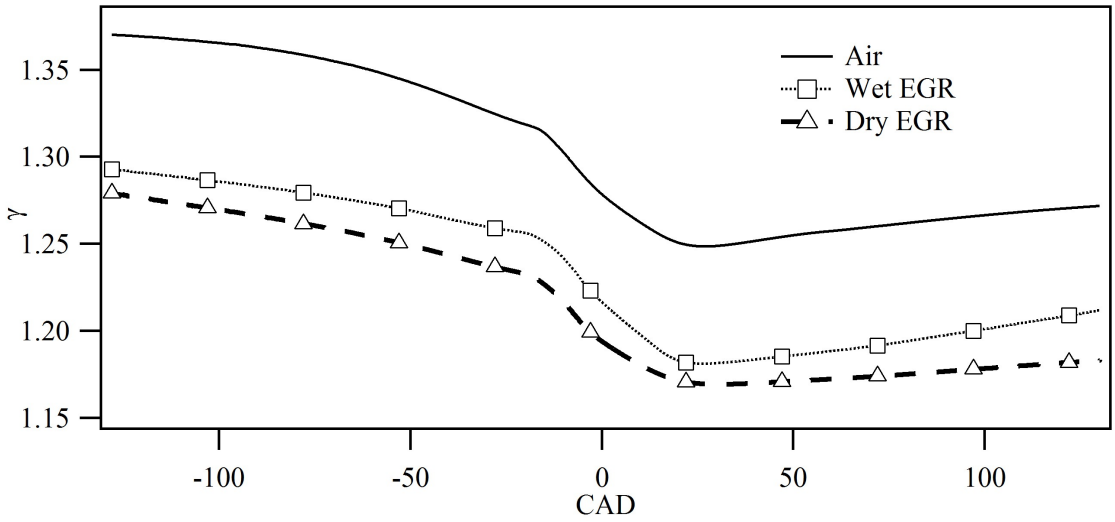

Figure 7.7: γ values vs. CAD of the cylinder mixture for the peak thermal efficiency cases.

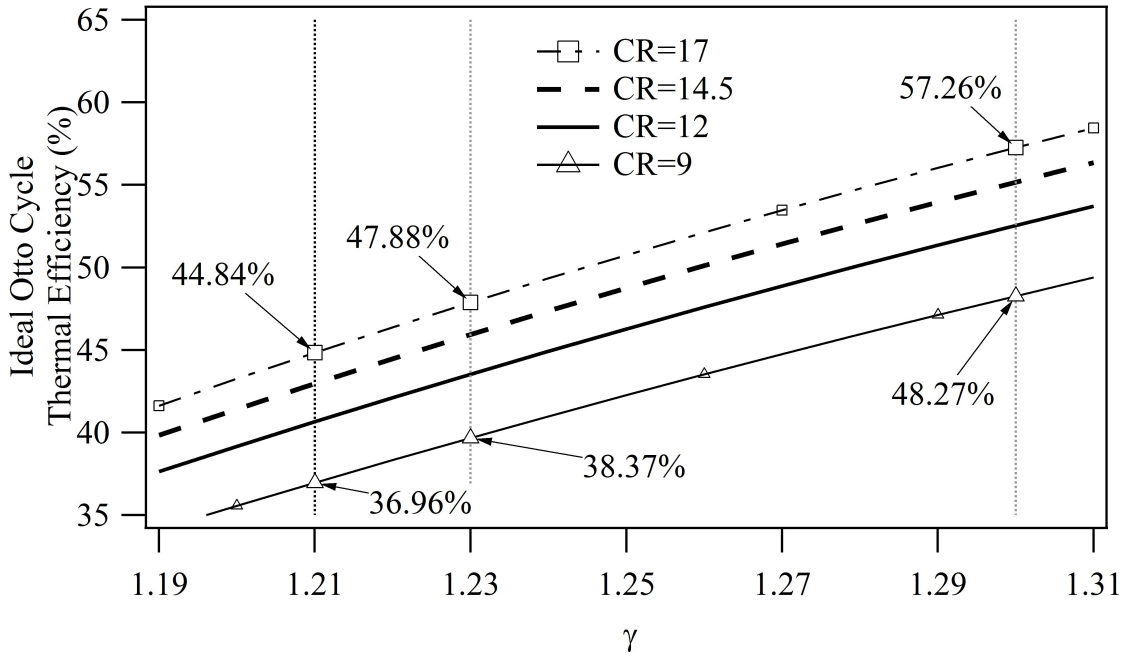

Figure 7.8: Thermal efficiency of the ideal otto cycle. Vertical lines are positioned at the average γ value of each case: dry EGR = 1.21, wet EGR = 1.23, air = 1.30.

(Woschni 1967). The model includes blow-by mass loss which is estimated on the basis of comparison of measured and calculated motored pressure trace. Normalized heat release is

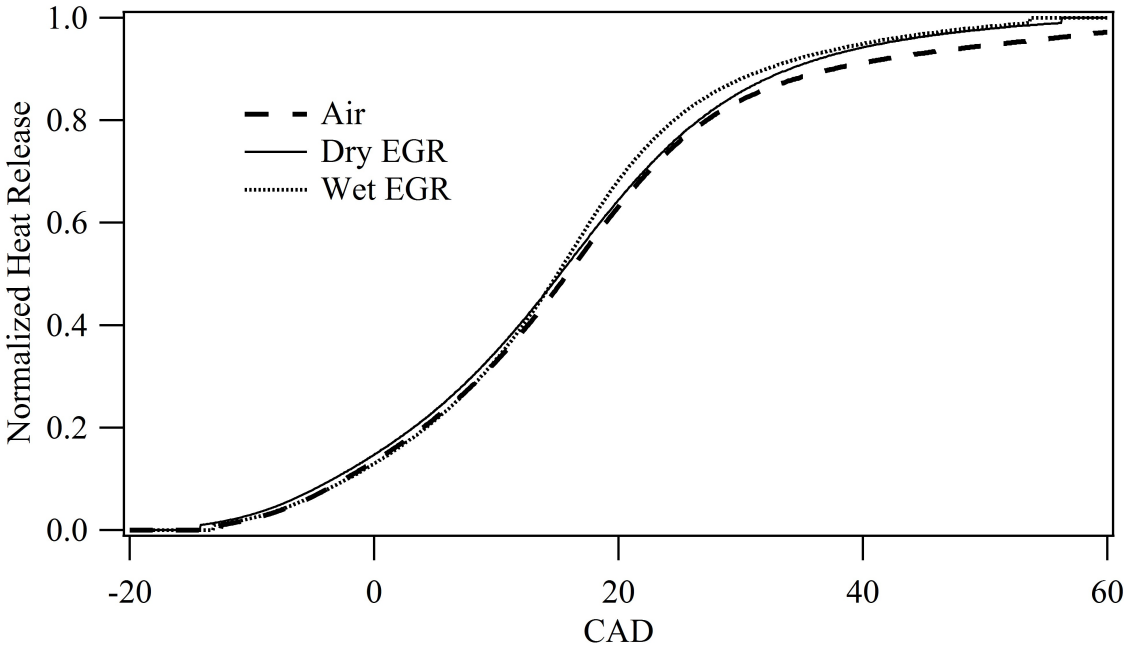

Figure 7.9: Normalized heat release curves of the three maximum thermal efficiency cases.

obtained by integrating the rate of heat release and dividing it by total heat released during the combustion process.

For comparison, the results of selected wet EGR tests are shown in Fig. 7.10. Increasing the O_2 concentration results in a more rapid Heat Release Rate (HRR), while decreasing the O_2 concentration produces a slower HRR. Base on the effect of O_2 concentration on HRR, combined with the correlation of Fig. 7.9 across working fluids, it is apparent that for these engine conditions, a HRR corresponding to a spark in the 20-30°BTDC range is optimal for all working fluids.

The normalized heat release curves provide some insight explaining the reduced effect of CR on thermal efficiency at low O_2 concentrations. With slow heat release, it is necessary to spark very early to achieve solid combustion in the high pressure region and avoid excessive exhaust losses. Therefore the heat released before TDC is higher for slow combustion cases (see Fig. 7.10), and thus increasing the CR will force the spark to retard to avoid increased wall heat losses. Since the combustion is slow, the increase in exhaust losses (defined as the energy lost due to high temperature exhaust exiting the cylinder) as a consequence of spark retard is counteracting the positive effect of the increased CR. At higher O_2 concentrations, the overall HRR is faster, allowing later spark-timing without producing excessive exhaust losses, therefore increasing the impact of CR. However, the high O_2 and fuel concentrations produce higher in-cylinder temperatures which increase heat losses such that the thermal efficiency is reduced relative to lower O_2 concentration cases.

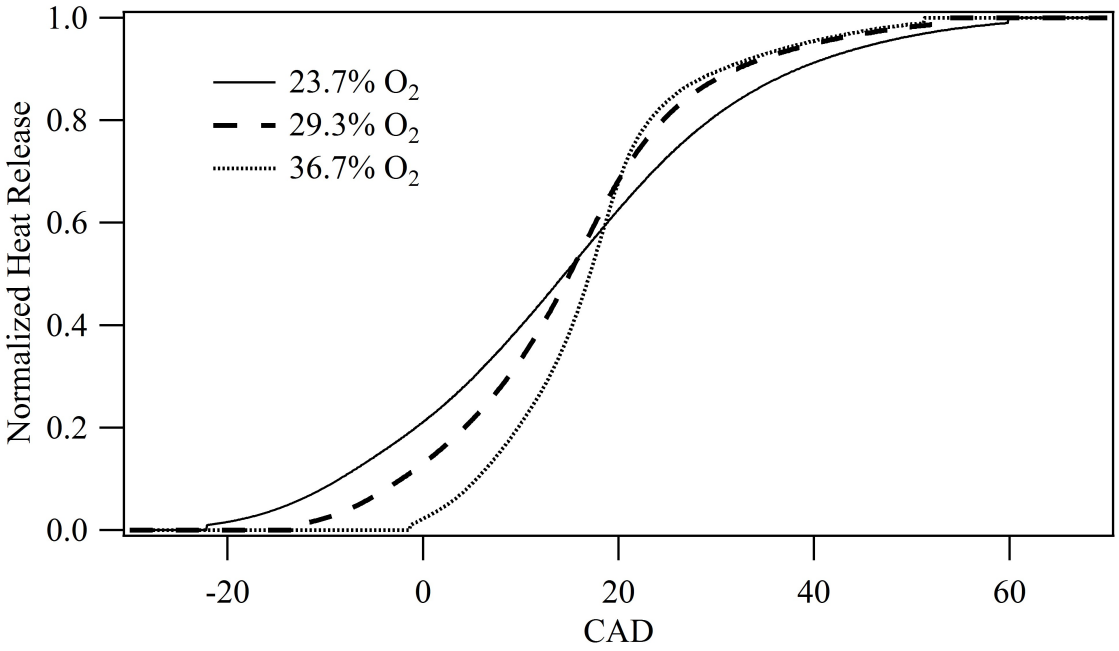

Figure 7.10: Normalized heat release of wet EGR cases. Note that the 29.7% O_2 case, which produced the highest overall thermal efficiency for wet EGR, is nearly identical to the air case.

Based on these findings, it can be concluded that the ideal oxycombustion case should produce a high HRR with low O_2 concentrations. It could be possible to increase the HRR at a given O_2 concentration through traditional techniques, such as increased tumble or swirl, or moving to an engine with multiple spark plugs. By increasing the HRR for each O_2 concentration, the maximum thermal efficiency should occur at a lower O_2 concentration (one producing a HRR similar to methane-in-air) and the value of the maximum thermal efficiency should be increased due to reduced heat losses.

Combustion Efficiency and CoV IMEP

In order to thoroughly investigate oxycombustion in an SI engine, the combustion efficiency and CoV IMEP were also investigated. Combustion efficiency could explain some of the noticed thermal efficiency effects. For example, the theoretical thermal efficiency of wet EGR is higher than the theoretical thermal efficiency of dry EGR, but experimental results found that wet EGR produced the lower thermal efficiency. This low thermal efficiency could be partly explained if the wet EGR had poor combustion efficiency relative to dry EGR. In addition, low combustion efficiency could also represent a source of possible improvement, or be an issue for catalysts and exhaust cleanup.

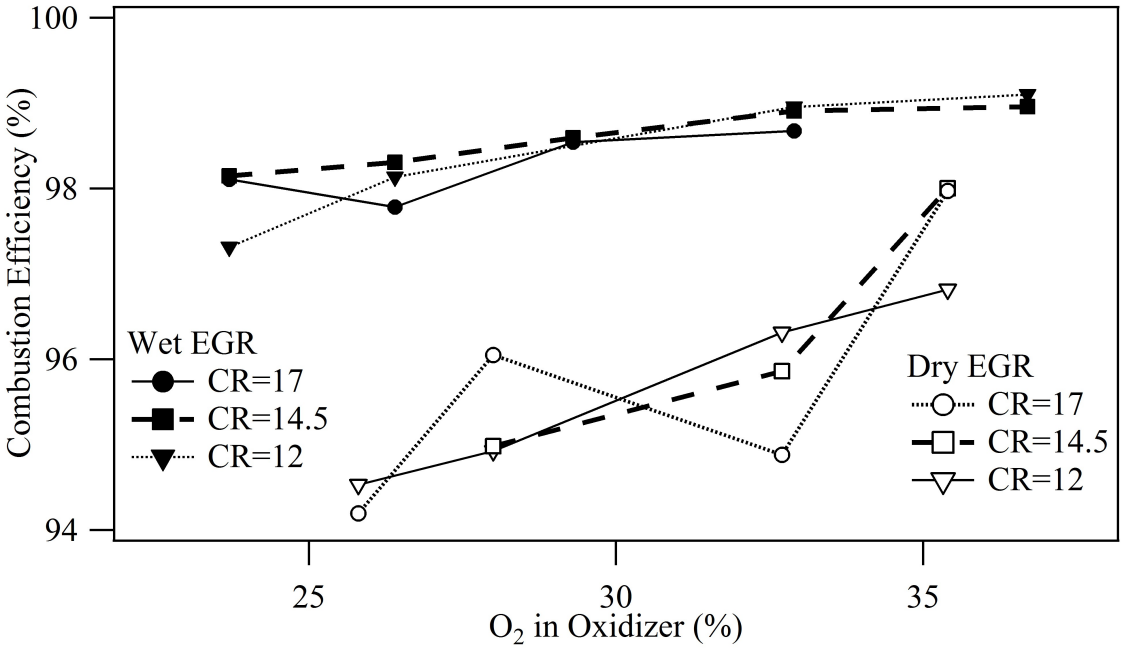

Figure 7.11: Measured combustion efficiency of wet and dry EGR.

The combustion efficiency corresponding to the peak thermal efficiency of each case is presented in Fig. 7.11. It is immediately clear that the lower thermal efficiency of wet EGR when compared to dry EGR is not the result of poor combustion efficiency. Rather, dry EGR produces the lower combustion efficiency, which is likely due to the negative kinetic effects of CO_2 on combustion (Liu, Guo, and Smallwood 2003; Mazas, Lacoste, and Schuller 2010; Walton et al. 2007). The higher intake temperature of the wet EGR could also help improve the combustion efficiency. Overall, wet EGR cases show good combustion efficiency of over 98% for most cases with good consistency, indicating little room for improvement, while dry EGR produces a combustion efficiency of only 94-96% for most of the cases and shows a high level of variation. Any improvement to the combustion efficiency of dry EGR would be very beneficial, as it would directly increase thermal efficiency while reducing the requirements of exhaust cleanup. Similar strategies as suggested for increasing HRR (increased swirl or tumble, multiple spark plugs, etc.) could prove effective in increasing the combustion efficiency.

Measured engine-out emissions of THC and CO for the CR=17 cases are shown in Fig. 7.12 in g/kWh. For all oxygen concentrations wet EGR produces lower engine emissions than dry EGR for both CO and THC. The increased combustion efficiency of dry EGR at 35.4% (Fig. 7.11) corresponds to a significant decrease in the engine out THC levels, while the CO levels remained relatively constant. As previously mentioned, there was a large amount of variation in the measured emissions of dry EGR even among spark sweeps at a single oxygen

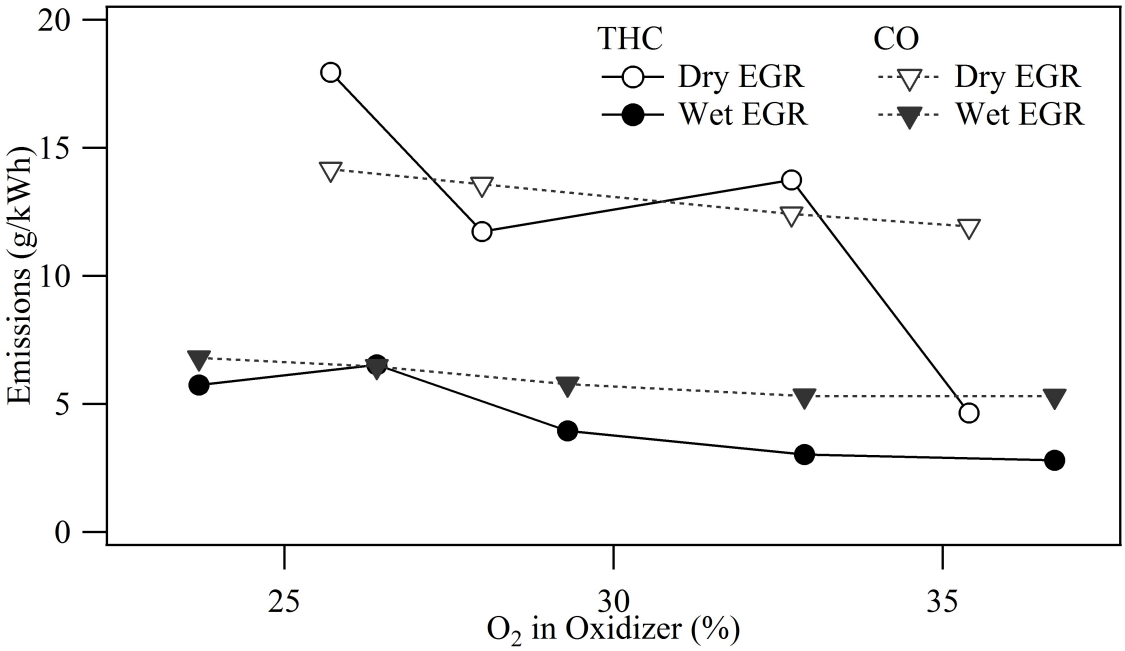

Figure 7.12: Measured engine-out emissions of wet and dry EGR for CR=17.

concentration. It should also be noted that presented emissions are engine-out, not tailpipe. As a result of the very high levels of EGR used for these systems, between 50-85% of these engine-out emissions would be recirculated to the intake, reducing the tailpipe emissions to 50-15% of the values shown in Fig. 7.12.

Both EGR cases show increasing combustion efficiency with higher O_2 concentrations, though the variation of dry EGR makes it hard to identify a clear correlation. Compression ratio does not seem to have a significant impact on combustion efficiency for either case.

The significant increase in dry EGR combustion efficiency at the 35.4% O_2 case could partially explain why the drop-off in thermal efficiency relative to the 32.7% O_2 case is so minor. However, it is not clear whether this is a repeatable increase due to the higher O_2 concentration, or if the increase in combustion efficiency is simply within the range of variability.

All of the EGR peak thermal efficiency points correspond to reasonable CoV IMEP values as shown in Fig. 7.13. The wet and dry EGR cases are very similar, and show a strong correlation relative to the O_2 concentration. Dry EGR cases had slightly higher CoV IMEP values than corresponding wet EGR cases, but the difference is relatively small. The difference is likely a product of the lower flame speed in dry EGR at equivalent O_2 concentrations as well as the lower and more variable combustion efficiency shown in Fig. 7.11.

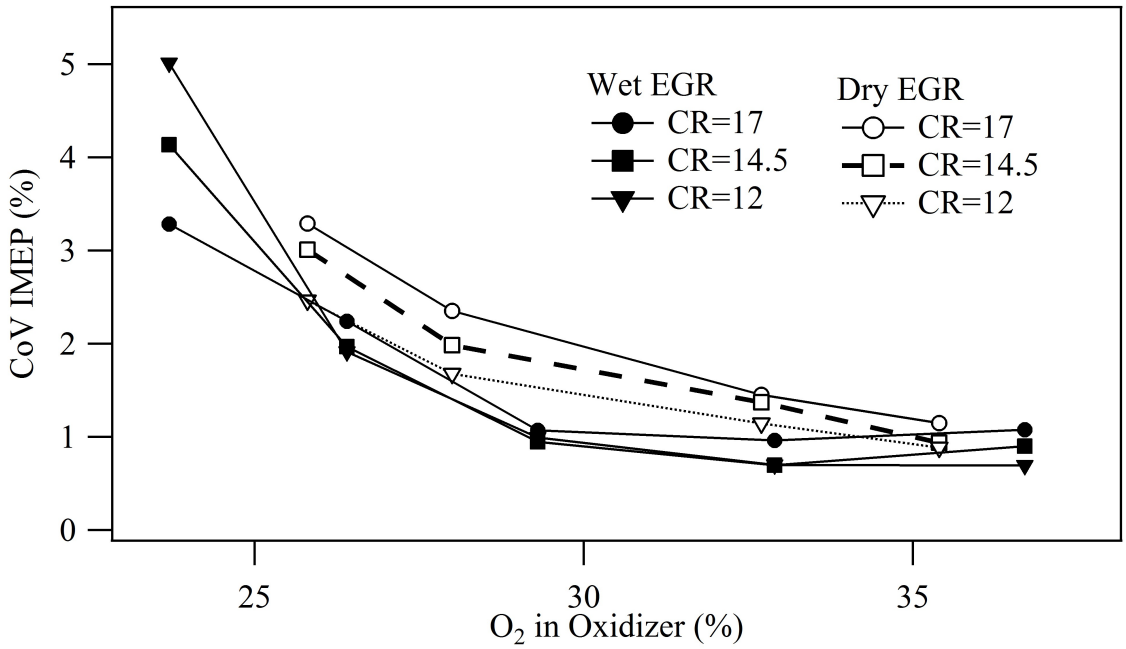

Figure 7.13: CoV IMEP values for wet and dry EGR cases.

Poor Performance of wet EGR

It has been shown that wet EGR produced the lowest experimental thermal efficiency of all three working fluids. This was unexpected, as wet EGR produces a higher flame speed than dry EGR under similar O_2 concentrations, has a higher average γ than dry EGR, and showed better combustion efficiency than dry EGR. Combining these effects, one would expect wet EGR to produce peak thermal efficiency of 2-3% points higher than dry EGR, rather than the 1.4% point decrease measured.

It appears that the higher intake temperature and pumping losses have minimal effects and are not the primary reason for the low thermal efficiency. Initial calculations indicate that wet EGR loses a much larger percentage of fuel heat to the cylinder walls than dry EGR. This difference in heat loss is more than the effect of the elevated intake temperature, and is hypothesized to be the primary reason for the reduced thermal efficiency. One possible explanation for the high heat transfer could be that the high water concentration of the working fluid (Table 7.1) results in a very small quantity of water condensing on the cylinder walls, thus greatly increasing the convection coefficient.

7.4 Conclusions

Comparing wet and dry EGR, it was found that despite having a lower theoretical maximum thermal efficiency, dry EGR produced higher measured thermal efficiency than wet EGR for all O_2 concentrations. The difference in thermal efficiency is not a result of combustion efficiency; dry EGR had lower and more variable combustion efficiency, but rather it appears to be caused by a much larger wall convection coefficient for the wet EGR case.

Experimental peak thermal efficiency of both EGR cases occurred at significantly elevated O_2 concentrations relative to air. The best thermal efficiency for both EGR cases was found to occur with O_2 concentrations corresponding to an ideal spark-timing of 20-30°BTDC. The heat release curves corresponding to the maximum thermal efficiency show good agreement across all three cases, with both higher and lower HRRs resulting in decreased thermal efficiency. This represents a possibility for improvement, as increasing the HRR at each O_2 concentration through tumble, swirl, or increased number of spark plugs would shift the peak thermal efficiency case to a lower O_2 concentration. This should produce higher efficiency, as the heat losses to the cylinder walls and exhaust losses would be reduced.

Chapter 8

NO_x Reduction Using Oxycombustion

This chapter investigates nitric oxides (NO_x) production in a spark-ignited (SI) internal combustion engine under oxycombustion conditions. In oxycombustion, the concentration of N_2 can be controlled to very low levels, thus reducing the rate of formation of NO_x. In addition, the concentration of O_2 can be reduced by using higher levels of Exhaust Gas Recirculation (EGR), reducing in-cylinder temperature, and thus further reducing NO_x formation.

Current NO_x regulations vary widely based on location and engine size and type, but in general the regulations for most stationary power sectors falls in the 1-2 g/kWh range. However, trends have been towards unifying, and lowering, the standards. South coast air quality management (SCAQM) in southern California continues to set the bar for NO_x regulation, currently limiting engines to 0.15g/kWh NO_x and attempting to further reduce the limit to 0.0323g/kWh. This is far ahead of the rest of the country, which is currently targeting 1g/kWh NO_x, but historically California and SCAQM have been the leaders in pollution control, and it is likely the rest of the country will follow their lead.

When considering oxycombustion, one logical solution would be the complete removal of N_2 from the air; if no N_2 was present in the system then NO_x formation could not occur. However, separating N_2 from air requires energy and capital investment, and in general the costs required to produce O_2 scale with the desired purity of O_2. In addition, creating a perfectly sealed EGR system is expensive and challenging. Even a small leak which develops over time will allow trace amounts of N_2 into the system and produce NO_x. Therefore from a capital and practical standpoint it is desirable for the system to tolerate some quantity of N_2 while still suppressing NO_x formation enough to satisfy regulations. Since the rate of production of NO_x in an SI engine is a continuum, from zero production when there is no N_2 present, to production of several hundred times over regulatory levels when combusting stoichiometrically in air, it follows that there must exist an acceptable level of N_2 at which regulations can be satisfied while saving the capital cost of eliminating N_2 from the system.

The concept of sequestering the NO_x with liquid CO_2 can also be pointed to as an alternative to NO_x reduction. However, despite being commonly proposed, the concept has not been thoroughly researched or understood (Grunwald 2009). Residual emissions, such as NO_x, which are not absorbed into the liquid CO_2 could present significant issues for the

sequestration process. In the situation where there is a small fraction of residual N_2 which needs to be vented, pollutants would also be partially vented, requiring that the vented stream be cleaned to prevent the release of urban pollutants. If the gaseous pollutants were buried along with the CO_2 they would displace large quantities of space, and could lead to storage problems such as harmful leaks (Grunwald 2009). It is therefore reasonable to conclude that minimizing the production of NO_x is beneficial, even when considering Carbon Capture and Sequestration (CCS).

NO_x formation requires the presences of N_2, for which the quantity formed is a function of in-cylinder conditions, or fuel-bound nitrogen, which is primarily a function of the quantity of bound nitrogen. Methane contains no fuel-bound nitrogen, thus, it is expected that NO_x formation will vary with brake thermal efficiency, power density, and Coefficient of Variation of Indicated Mean Effective Pressure (CoV IMEP). Three main factors were studied to quantify the effects on NO_x production: N_2 concentration, O_2 concentration, and the working fluid composition and concentration. As part of the study, spark timing and CR are also varied to determine if a correlation exists between efficiency and NO_x production.

8.1 NO Formation Theory

Four main routes produce NO during the combustion process: thermal, prompt, N_2 O, and fuel bound nitrogen. Thermal NO, known as the Zeldovich mechanism, consists of 3 main reactions (Eqn. 8.1). Of the three reactions, the first is the rate limiting step, and emerges at temperatures greater than 1800K, which is the reason for the name 'thermal NO'. Above 1800K, the rate of reaction 3 is exponentially dependent on temperature, roughly doubling with every increase of 70K. The reaction is so slow that equilibrium NO levels are reached only for times which are longer than typical residence times in the high temperature range (some ms) (Warnatz, Maas, and Dibble 2006). Thermal NO is strongly exponential, with small increases in temperature resulting in much higher NO production.

$$\begin{aligned} N_2 + O &\rightarrow NO + N \\ N + O_2 &\rightarrow NO + O \\ N + OH &\rightarrow NO + H \end{aligned} \tag{8.1}$$

The formation rate of NO, assuming nitrogen atoms are in a quasi-steady state (based on the fast reaction of the second two reactions in Eqn. 8.1), can be reduced to Eqn. 8.2. It is therefore clear that for SI piston engine combustion, which routinely exceeds 1800K, the formation rate of thermal NO can be minimized by reducing N_2, O, or temperature. It should be noted that oxycombustion allows adjustment of the N_2 concentration as well as some control over the temperature (through variation of the O_2 and fuel injected).

$$\begin{aligned} \frac{d[NO]}{dt} &= 2k_1[O][N_2] \\ k_1 &= 1.8 \cdot 10^{14} T e^{-\frac{318 kJ \cdot mol^{-1}}{RT}} \end{aligned} \tag{8.2}$$

Prompt NO, known as Fenimore NO, can form small quantities of NO in low temperature flames (>1000K) because the prompt NO results from the radical briefly appearing CH. In a combustion engine operating in SI mode, temperatures almost always exceed 1800K, which typically results in much greater NO formation through the Zeldovich mechanism than from Fenimore NO.

N_2O generated NO is typically an insignificant contributor to the total NO, but under certain conditions, when thermal and prompt NO production is very low, it can be significant. For example, very lean combustion can suppress the formation of CH, thus limiting Fenimore NO, and the lean mixture has low temperatures, thus suppressing Zeldovich NO. The result is in certain forms of combustion, such as premixed gas turbine engines, the N_2O route is the major source of NO (Correa 1993).

The formation of NO through fuel-bound nitrogen is mainly observed in coal combustion. It has been found that under certain conditions, as much as 2/3 of the fuel bound nitrogen can form NO (Warnatz, Maas, and Dibble 2006), however, in this investigation the fuel used is methane, which does not contain any fuel-bound nitrogen.

8.2 Varying Nitrogen Concentration

Experiments were performed using wet EGR with varying quantities of N_2. Compression ratio, spark-timing, and engine power were held constant across all runs. Control of engine power levels was achieved by varying the quantity of O_2 injected. Three different N_2 concentrations were tested, with intake oxidizer compositions listed in Table 8.1.

Table 8.1: Intake composition of constant-power N_2 test points (volume percent). EGR is defined as the volume fraction of the exhaust.

N_2	EGR	O2	CO2	Intake Water
2.0%	63.9%	28.7%	22.6%	45.1%
4.1%	62.9%	28.7%	22.0%	43.9%
12.6%	60.4%	28.3%	19.7%	39.4%

Measured performance and emissions results are shown in Table 8.2. As expected, efficiency and NO_x production decrease with the N_2 level in the oxidizer. Brake power was stable for all EGR runs, with a slight decrease for the methane-in-air case. This consistency provides confidence when comparing NO_x levels between different N_2-concentration cases.

Minor exhaust species are listed in Table 8.3. Relatively low THC, CO, and O_2 levels indicate good combustion efficiency, and the agreement between the HORIBA NO_x measurement and the electronic NO_x sensor reading adds confidence in measurement techniques. Note, that the measured PPM values listed in Table 8.3 include re-circulated NO_x (a component of the recirculared exhaust), and are therefore higher than the actual production of NO_x (with the exception of the air run). When NO_x measurements are converted to [g/kWh] (such as in Table 8.2) only the fraction of NO_x which exist the system through the exhaust is considered, allowing all cases to be compared directly.

Table 8.2: Measured performance and major exhaust species (% volume).

N_2	Brake Power (kW)	NO_x (g/kWh)	CO_2	Water
Air	1.459	10.19	9.0%	18.0%
12.6%	1.486	1.94	28.9%	58.4%
4.1%	1.486	0.88	31.1%	63.4%
2.0%	1.487	0.51	31.4%	64.8%

Table 8.3: Measured minor exhaust species (reported in PPM unless noted, % volume).

N_2	O_2	THC	CO	NO_x	NO_x Sensor
Air	0.64%	2150	1690	1470	1310
12.6%	0.56%	1790	2500	770	705
4.1%	0.53%	1830	2510	360	345
2.0%	0.51%	2050	2580	215	210

Experimental results are plotted against equilibrium NO_x levels in Fig. 8.1. The significant finding is that NO_x varies almost linearly with N_2 concentrations, where as the model predicts higher NO_x levels and a curving profile. However, even with 2.0% N_2 too much NO_x was produced to satisfy the current SCAQM emission regulations, which require less than 0.15 g/kWh NO_x emissions. If we assume the linear trend between NO_x production and N_2 continues, a N_2 concentration of less than approximately 0.6% in the oxidizer would be necessary for meeting the standard at this CR, spark-timing, and power level.

8.3 Wet versus Dry EGR

Several different O_2 concentrations were run with a small amount of N_2 injection. Measured intake oxidizer values and the range of spark timings tested are listed in Tables 8.4 and 8.5.

All cases were run at CRs of 12, 14.5, and 17, with spark-sweeps performed which spanned the maximum break torque and peak IMEP. NO_x emissions were measured in PPM, and converted to g/kWh based on the estimated exhaust flow rate (Section 4.3) and the measured

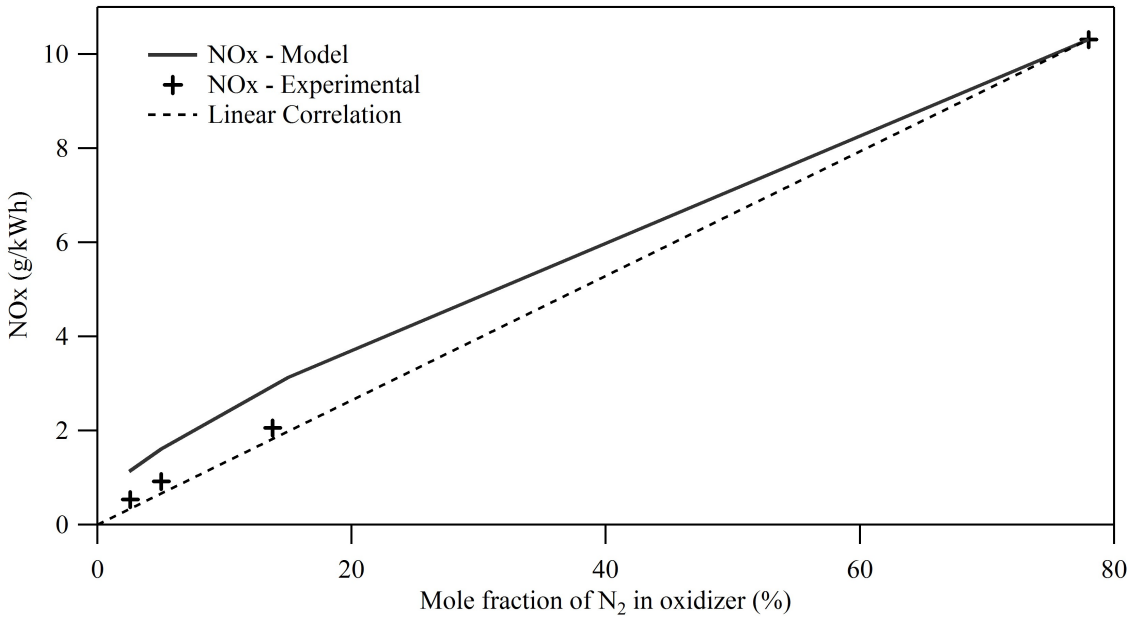

Figure 8.1: NO_x formation rate versus N_2 concentration.

Table 8.4: WET EGR INTAKE COMPOSITIONS TESTED.

Case	O_2	CO_2	Water	N_2	Total
Wet EGR 1	23.7%	24.1%	49.1%	2.11%	99.5%
Wet EGR 2	26.4%	23.1%	47.7%	2.07%	99.8%
Wet EGR 3	29.3%	22.3%	45.4%	2.06%	99.3%
Wet EGR 4	32.9%	20.5%	43.6%	1.89%	99.2%
Wet EGR 5	36.7%	19.0%	41.2%	1.98%	99.1%

brake power. Because the NO_x is determined based on exhaust flow rate, and not engine flow rate, the wet EGR numbers are properly adjusted to account for the large quantity of NO_x which recirculates through the engine and is not released as emissions.

NO_x emissions for wet and dry EGR cases are shown with respect to spark timing in Fig. 8.2 (a) and (b), respectively. Common shapes represent a single O_2 concentration (i.e. for wet EGR square symbols represent 36.7% O_2) while shading indicates the CR: white is CR=17, grey is CR=14.5, black is CR=12. Higher O_2 concentrations correspond to higher NO_x production for similar spark-timings. This is a direct result of the increased combustion temperatures, which increase the k_1 factor in Eqn. 8.2.

Both working fluids were able to produce some cases below the 1 g/kWh regulation level, but only at the lower O_2 concentrations. Only the lowest O_2 concentrations were able to

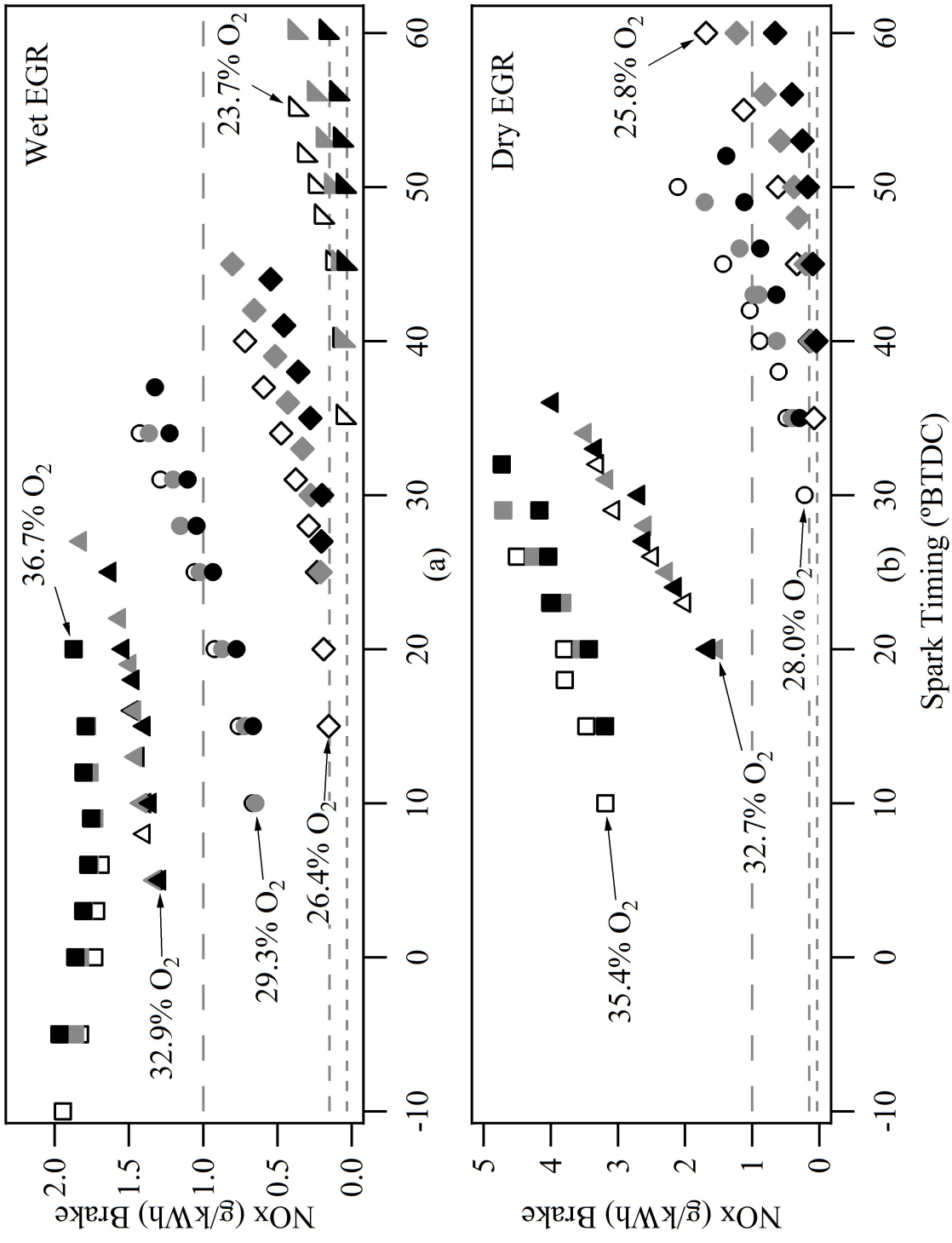

Figure 8.2: Measured NO_x at each experimental point. Common shapes represent a single O_2 concentration (labeled), and shading indicates the CR. White symbols are CR=17, grey symbols are CR=14.5, and black symbols are CR=12. The three horizontal dashed lines represent the major NO_x regulations of 1g/kWh, 0.15g/kWh, and 0.0323g/kWh

Table 8.5: DRY EGR INTAKE COMPOSITIONS TESTED.

Case	O_2	CO_2	N_2	Total
Dry EGR 1	25.7%	69.1%	3.1%	98.0%
Dry EGR 2	28.0%	68.8%	3.2%	100.0%
Dry EGR 3	32.7%	63.9%	3.5%	100.1%
Dry EGR 4	35.4%	61.1%	3.5%	100.0%

operate below the 0.15 g/kWh limit, and even those cases were limited primarily to low CRs and later spark-timing. Neither working fluid was able to operate below the 0.0323 g/kWh regulation level for any O_2 concentration or spark-timing, but trends indicate that it would be possible with low enough O_2 concentrations and late enough spark-timings. However, other major factors, such as thermal efficiency, CoV IMEP, and power, should be considered in relation to the NO_x production. It is also interesting to note the decreasing effect of CR at higher O_2 concentrations; for both wet and dry EGR the lowest O_2 cases show a significant spread, with CR 12 producing less NO_x than CR 17, while the highest O_2 cases have no apparent difference between CRs. This effect is studied in Fig. 8.3 (a) and (b), which show a breakdown of the NO_x production in ppm (a) and the brake power (b) for the dry EGR cases with 32.7% O_2 and 25.8% O_2.

From Fig. 8.3 (a) and (b) it is apparent that the reason for the convergence of NO_x production in g/kWh at higher O_2 concentrations is partly a combination of the reduced spread in the NO_x ppm production, and also is a result of a strong correlation between NO_x (ppm) production and power. For example, in Fig. 8.3 (a), the 32.7% O_2 curve for CR 12 has an out-lying point at a spark-timing of 30°BTDC. Referring to Fig. 8.3 (b), the corresponding point is also noted to be out-lying as a low power production point. This strong correlation between power and NO_x (ppm) is not seen in the lower O_2 concentration case. The decreased spread in measured NO_x levels (ppm) at higher O_2 concentrations is attributed to the higher combustion temperatures and later spark-timing, which somewhat reduces the relative significance of the CR on NO_x production. The combined effects at higher O_2 concentrations of reduced NO_x (ppm) spread and correlation between NO_x (ppm) and power result in the convergence of NO_x (g/kWh) for all CRs seen in Fig. 8.2.

NO_x versus Performance

The objective of any NO_x cleanup system is the reduction or elimination of NO_x from the exhaust while minimizing the negative effects on the engine operation. Therefore, it is of interest to investigate not only how much NO_x is produced, but how the production varies relative to important engine parameters, such as brake power, brake thermal efficiency, and CoV IMEP.

The NO_x production relative to brake power at CR 17 are shown in Fig. 8.4 for all 9 of the EGR cases tested. As previously observed, reduced O_2 concentrations result in lower NO_x,

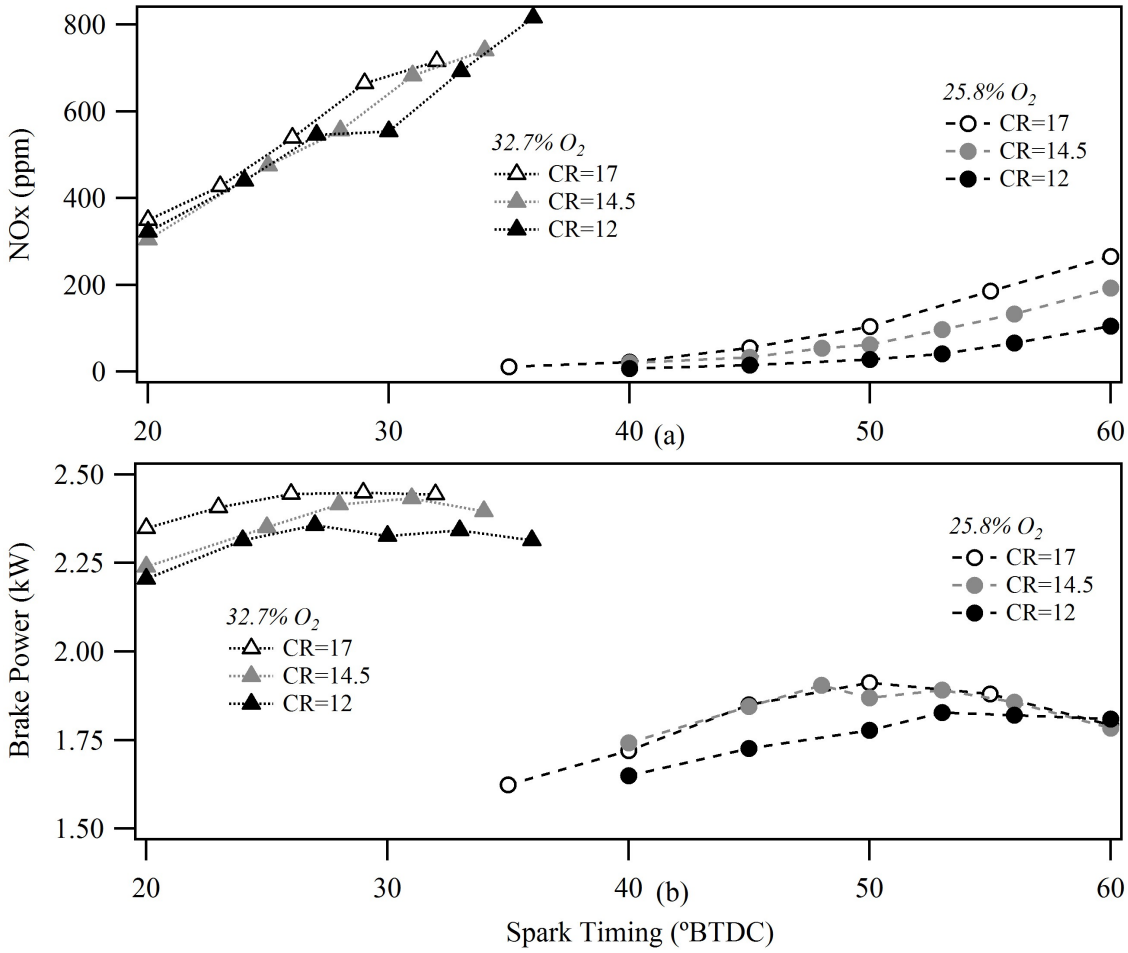

Figure 8.3: Comparison of the NO_x production in ppm (a), and the brake power production (b), for dry EGR cases with 32.7% O_2 and 25.8% O_2 for all CRs and spark-timings.

but this is correlated with lower power production. Surprisingly, dry EGR produces lower NO_x levels for equivalent brake power despite having significantly higher N_2 concentrations. This is believed to be the results of the lower intake temperature of dry EGR relative to wet EGR, as well as the slightly higher specific heat of dry EGR. These factors combine to produce higher in-cylinder temperatures for the wet EGR case, which is significant due to the exponential dependence of NO_x formation on temperature.

One of the primary focuses of any power production is the thermal efficiency, particularly for stationary power generation, in which power density is often not a major concern (as opposed to planes or cars, where power density is paramount). Figure 8.5 shows the NO_x production versus thermal efficiency for all wet and dry EGR O_2 concentrations at CR 17. Despite having the higher N_2 concentration, dry EGR has slightly better performance than

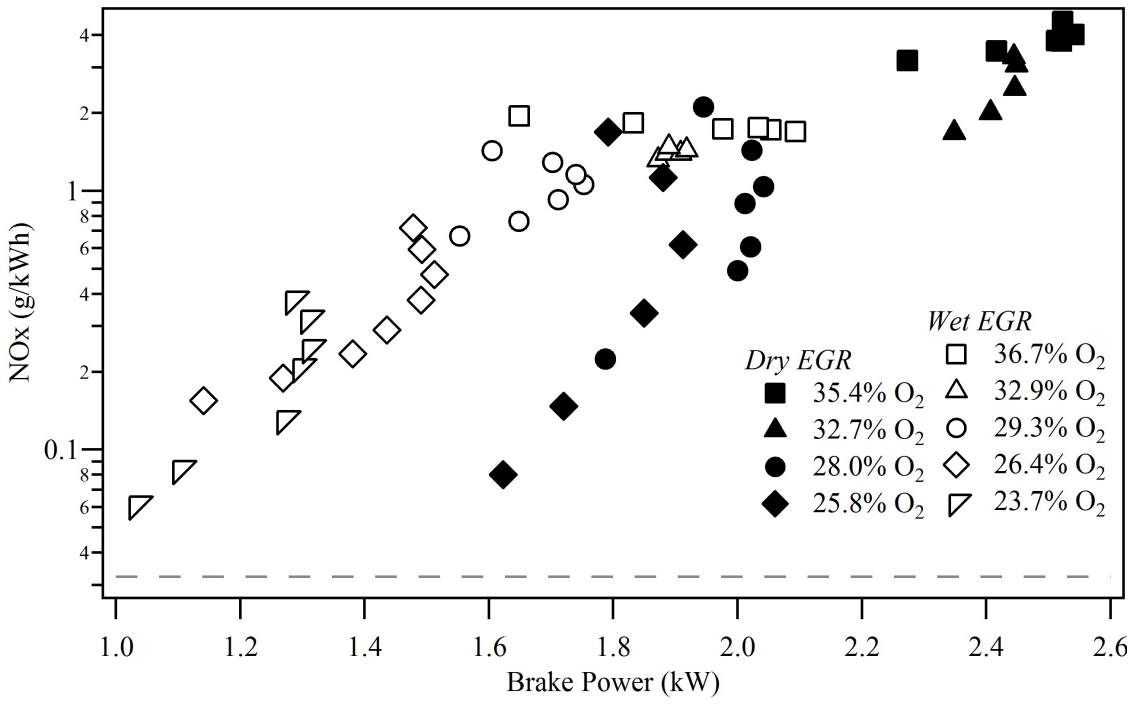

Figure 8.4: NO_x production of wet and dry EGR versus brake power at CR 17.

wet EGR - producing lower NO_x levels for similar thermal efficiencies - but the difference is much less pronounced than was seen in Fig. 8.4. The trade-off between NO_x production and thermal efficiency is clear for both working fluids; conditions which lower NO_x production also reduce thermal efficiency.

Figure 8.5 clearly shows the correlation between NO_x production and brake thermal efficiency, but only includes results from CR 17. Based on Fig. 8.2, which showed that at low O_2 concentrations the CR has a significant effect on NO_x production, it is possible that the reduced CRs at the lowest O_2 concentrations could produce better results than the CR 17 cases. A comparison of the wet EGR case with 23.7% O_2 and the dry EGR case with 25.8% O_2 is shown in Fig. 8.6(a). When plotted relative to brake thermal efficiency, there is not a strong reduction in NO_x production with decreasing CR. For wet EGR the CR 12 curve does fall at a slightly lower NO_x production than CR 14.5 or 17, but the difference is relatively minor. Dry EGR shows a similar trend, but with more variability. Overall, if reduced NO_x is the objective, it appears that there is a slight advantage to operating at a lower CR with low O_2 concentrations.

Figure 8.6(b) shows how the NO_x production varies with CR at higher O_2 concentrations. It is interesting that at the higher O_2 concentration, the dry EGR curves do no converge, but rather have inverted, with the CR 17 case now showing both the lower NO_x and higher thermal efficiency values. This is a result of the increased effect of CR on brake thermal

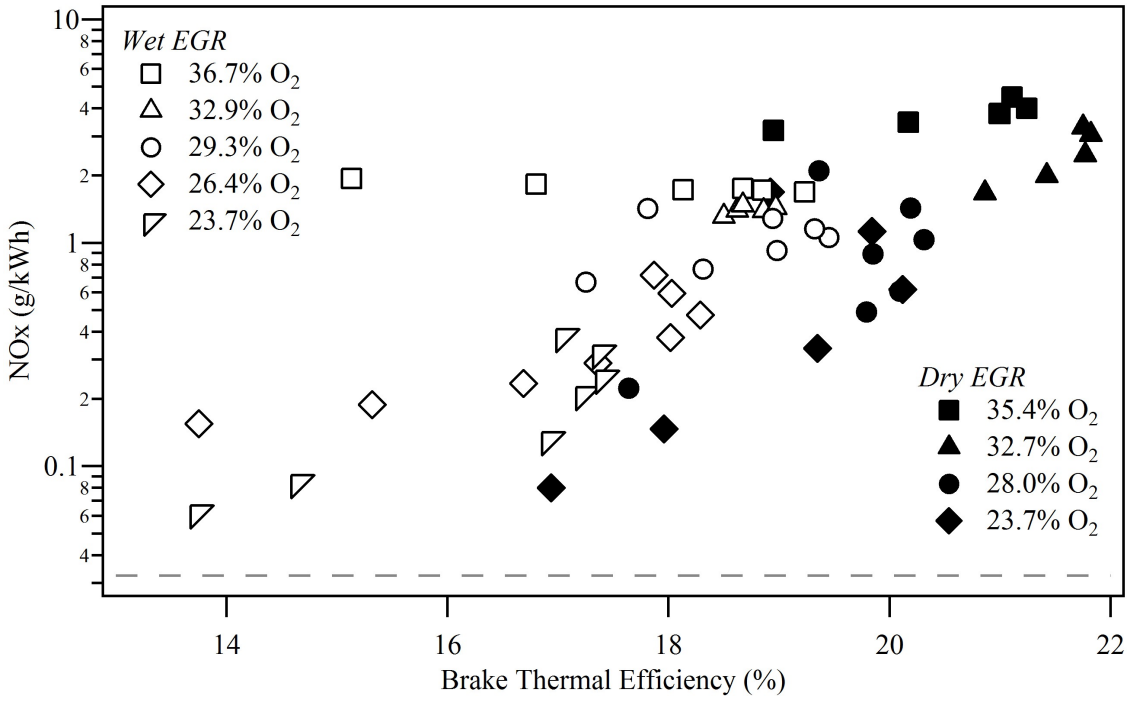

Figure 8.5: NO_x production of wet and dry EGR versus brake thermal efficiency at CR 17.

efficiency, and a corresponding decreased dependence of the NO_x production on CR. Wet EGR shows very little change in NO_x production across all test points, indicating that the maximum efficiency point should be used. Note that for all cases show in Fig. 8.6(b) the NO_x production is well over an order of magnitude greater than the regulation level, and thus it is unlikely it would be desirable to sacrifice any thermal efficiency for minor NO_x reduction.

Finally, NO_x production of the wet and dry EGR data points, including all O_2 concentrations and CRs, are plotted against CoV IMEP values (Fig 8.7). Once again, there is a clear trade-off between the desired low NO_x production, and the need for a low CoV IMEP. Wet EGR cases produce slightly better results than dry EGR, which is likely due to the higher flame speeds, but both fluids show a large quantity of scatter. In general, it is not acceptable to operate an engine for prolonged periods with a CoV IMEP of more than 5%, which corresponds to a minimum NO_x production of roughly 0.3 g/kWh - an order of magnitude greater than the regulation level of 0.0323 g/kWh.

Conclusions

NO_x production is negatively correlated with power, thermal efficiency, and CoV IMEP. It is possible to reduce NO_x levels to near regulation levels by using low O_2 concentration levels and sacrificing performance, but none of the test cases fell below the regulation limit. It

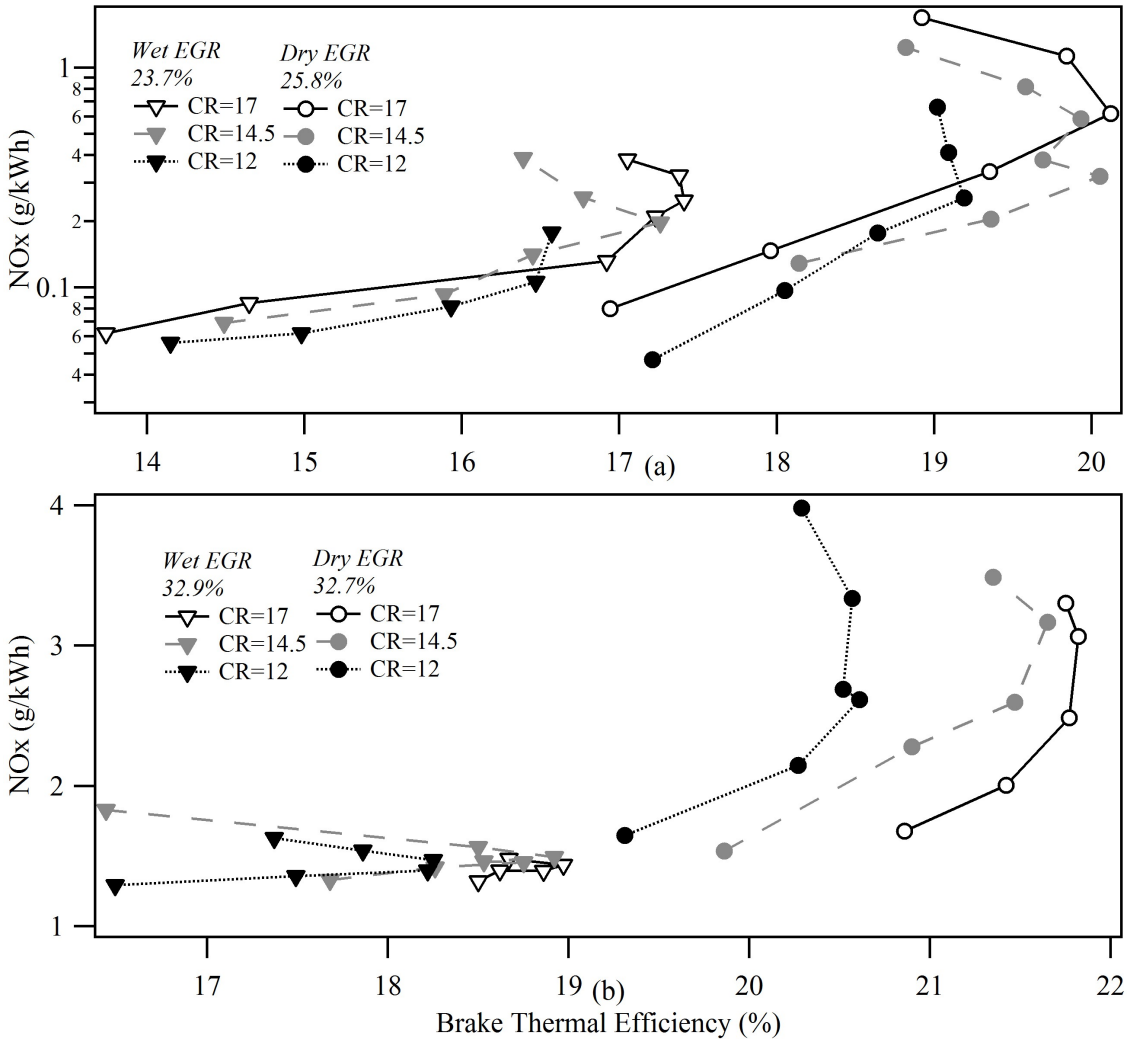

Figure 8.6: NO_x production of wet and dry EGR versus brake thermal efficiency for all CRs. (a) shows the minimum O_2 concentrations tested on a logarithmic scale. (b) shows higher O_2 concentration cases on a linear scale.

is important to note the linear correlation between N_2 concentrations and NO_x production, which means all of the results found can be extrapolated to other N_2 concentrations. Based on the observed trends, to operate below regulation NO_x levels with the amount of N_2 used in these tests (roughly 2% for wet EGR and 3-4% for dry EGR) would require taking unacceptable reductions in thermal efficiency and CoV IMEP. Using the CoV IMEP findings, along with the rule-of-thumb limit of 5% CoV IMEP, it appears that N_2 levels need to be on the order of 0.2-0.4% for NO_x compliance with the latest regulations while achieving reasonable engine performance.

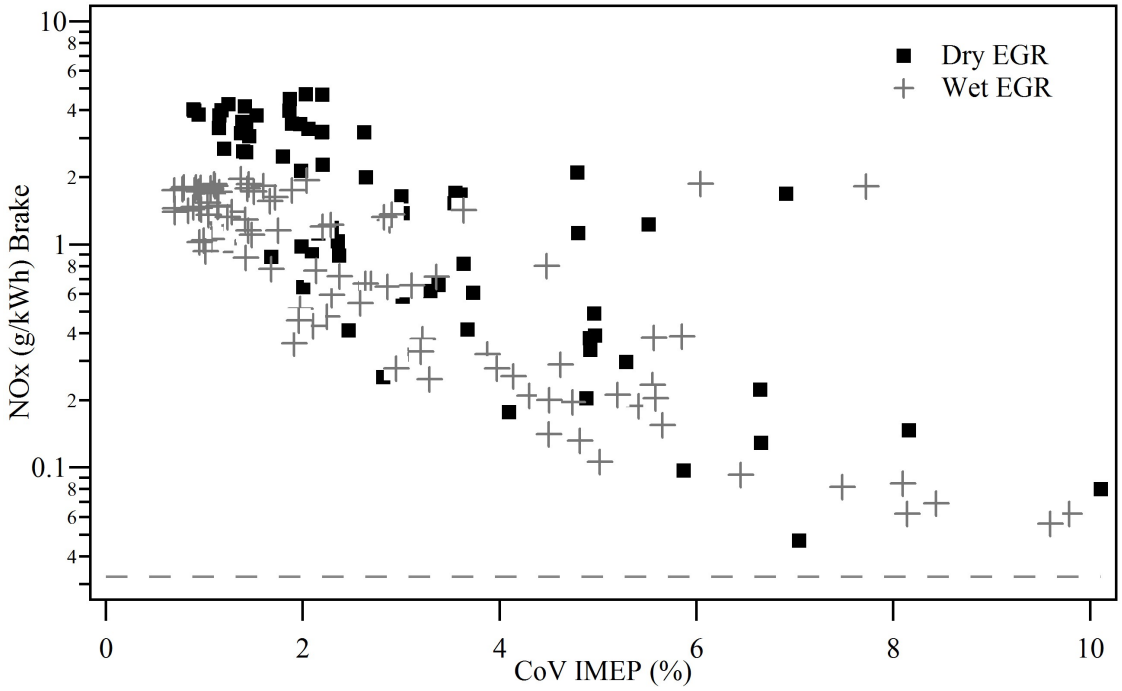

Figure 8.7: NO_x production of wet and dry EGR, including all O_2 concentrations and CRs, versus CoV IMEP on a logarithmic scale.

Chapter 9

Performance Limits of Heptane Oxycombustion

This research experimentally investigates the performance of a spark-ignited (SI) internal combustion engine under heptane (C_7H_{16}) fuel oxycombustion conditions and compares the results to heptane-in-air performance. Heptanes have very low knock resistance, with nHeptane (the least knock resistant heptane) being the definition of a zero octane rating. The low knock resistance is virtually the opposite of methane, which has a very high knock resistance; boasting an octane rating of over 100. The low knock resistance of Heptanes allows the study of different performance aspects, and limist, than was found when operating on methane, which had no knock limitations for any of the test points. Wet EGR was operated at an intake temperature of 100°C to prevent condensation while air and dry EGR operated at ambient temperatures. Even when the engine intake was naturally asperated with room temperature air, uncontrollable knock occured at CRs greater than 6.25.

As with the methane cases, the main performance characteristics that are experimentally investigated in this chapter are: 1) thermal efficiency, 2) combustion efficiency, and 3) Coefficient of Variation (CoV) of Indicated Mean Effective Pressure (IMEP). Thermal efficiency is based on IMEP values and the lower heating value of the injected methane. Combustion efficiency is computed by evaluating the energy of the carbon monoxide (CO) and unburned hydrocarbons in the exhaust relative to the energy of the injected fuel. Blow-by of the cylinder gases past the piston rings is not accounted for when computing the combustion efficiency. The experimental work was performed with two different working fluids: wet EGR and dry EGR. Multiple O_2 concentrations were tested for both working fluids, with all runs performed at a stoichiometric air-fuel mixture. Compression ratio (CR) and spark-timing sweeps were performed for each test, with a maximum CR of 17 and a maximum spark advance of 60°BTDC. In addition, the CR and spark-timing sweeps are performed with heptane-in-air combustion using the same engine conditions as a performance reference.

9.1 Knock Theory

Knocking in an engine is defined as the significant in-cylinder pressure oscillations which result from an uncontrolled auto-ignition of end-gases. The auto-ignition event results when a threshold temperature and pressure condition (fuel specific) are exceeded in the end-gas, and thus the knock resistance of a fuel is a function of its ability to resist auto-ignition, among other factors. The size and duration of these pressure oscillations determine the intensity of knocking, which is quantified by the MAPO and IMPO numbers as defined in section 4.4, which is primarily a function of the quantity of end-gas which ignites. High intensity knocking must be avoided, as the large pressure oscillations are detrimental to engine longevity. A natural conclusion would be that one should avoid knock all together, however, conditions which produce maximum thermal efficiency are often correlated with knocking when operating on fuels with poor knock resistance. Therefore, when specifying the range of acceptable operating conditions it is common to specify an acceptable knock intensity, which permits some engine knock, but requires modification of run conditions once the threshold is crossed.

Since knocking occurs when the end-gas reaches a temperature threshold, it is logical that the tri-atomic working fluid and ability to vary O_2 concentration of oxycombustion should be able to produce opertating points with superior knock resistance, and correspondingly the ability to operate at higher CRs. As was discussed in chapter 7, the effect of lower γ of the wet and dry EGR working fluids relative to air on the theoretical maximum efficiency could be partially offset by higher CRs. However, for methane it was found that even the air case was not knock limited at a CR of 17 (the highest CR possible), and therefore the EGR working fluids had no advantage. For a better understanding of the knock limitations, and any possible advantages, the same comparison was made using n-heptane fuel. N-heptane has very little resistance to knock, which permits an excellent opportunity to investigate how much, if any, knock resistance the EGR working fluids offer.

Knock Limit

The knock intensity of each thermal cycle was determined using the technique described in section 4.4, with a minimum of 500 thermal cycles analyzed for each case. Unlike the methane cases, which produced a local maximum efficiency with respect to spark-timing, the heptane cases continued to produce better thermal efficiency and lower CoV IMEP as the spark-timing was advanced. Therefore all cases were knock limited, and all thermal efficiency and CoV IMEP results presented correspond to the spark-timing at the knock-limit. The knock limit was defined as the operating condition at which 5% of the thermal cycles exceeded the specified knock intensity. Each thermal cycle is individually analyzed for knock intensity, which produces a value for both MAPO and IMPO. This process is repeated for all of the thermal cycles collected at a single run point, and the resulting values are used to create a distribution curve. Since the threshold values are defined as the number of cycles which exceed a specific MAPO or IMPO value, the distribution curve is

Table 9.1: Fraction of cycles with MAPO and IMPO knock index values exceeding the defined threshold. n-Heptane-in-air, CR=5.5.

Case Spark-timing	Fraction of cycles exceeding MAPO [0.50 Bar]	MAPO [0.75 Bar]	IMPO [7.5 Bar·°]	IMPO [10 Bar·°]
0	0.000	0.000	0.000	0.000
5	0.008	0.005	0.008	0.006
8	0.060	0.045	0.056	0.048
11	0.211	0.156	0.209	0.136
13	0.463	0.308	0.428	0.305

then integrated, normalized, and converted into curves which represent the fraction of cycles which exceed the corresponding MAPO or IMPO threshold (the X-axis). Figure 9.1 shows the curves produced for n-Heptane-in-air combustion at a CR of 5.5 for MAPO thresholds (a) and IMPO thresholds (b). Each curve represents a single spark-timing which was run. All of the curves start at a value of 1 at very low threshold values due to noise in the raw pressure signal. As expected, the curves shift higher as the spark-timing is advanced (i.e. the curve for spark-timing 13°BTDC is higher than the curve corresponding to 11°BTDC), indicating that for the same knock threshold, advancing the spark-timing results in a greater fraction of knocking cycles. The threshold chosen (X-axis) is not universally defined, rather an appropriate threshold must be chosen based on the required engine performance, engine robustness, and desired lifetime, among other things.

In Fig. 9.1(a), the Y axis represents the portion of cycles which produced knocking in excess of the corresponding MAPO threshold (the X axis). Figure 9.1(b) shows the same information, but with respect to an IMPO threshold. Table 9.1 shows the values of the individual curves for different specified threshold values. For example, if the threshold were defined as MAPO = 0.75 bar, and IMPO = 10 bar·°, the fraction of knocking cycles for each spark-timing would be equal to the value of each curve at the X-values of 0.75 and 10, respectively. Since the knock limit was defined as the point at which 5% of the cycles exceed the specified threshold, for this case, the limit falls at a spark-timing between 8 and 11°BTDC. For consistency when comparing runs, a linear interpolation is used to determine the point that corresponds to precisely the 5% limit. Interpolation is then also used to determine corresponding spark-timing, IMEP, CoV IMEP, and thermal efficiency.

As previously discussed, the threshold of knock intensity is not universal, and thus the cutoff values used in this study are somewhat arbitrary. The primary comparison between cases is made using a threshold value of 0.75 bar MAPO, and 10 bar·°IMPO. The effect of altering this threshold value are also discussed for select cases. The compositions tested were chosen to determine the profile of the thermal efficiency and knock limitation limits.

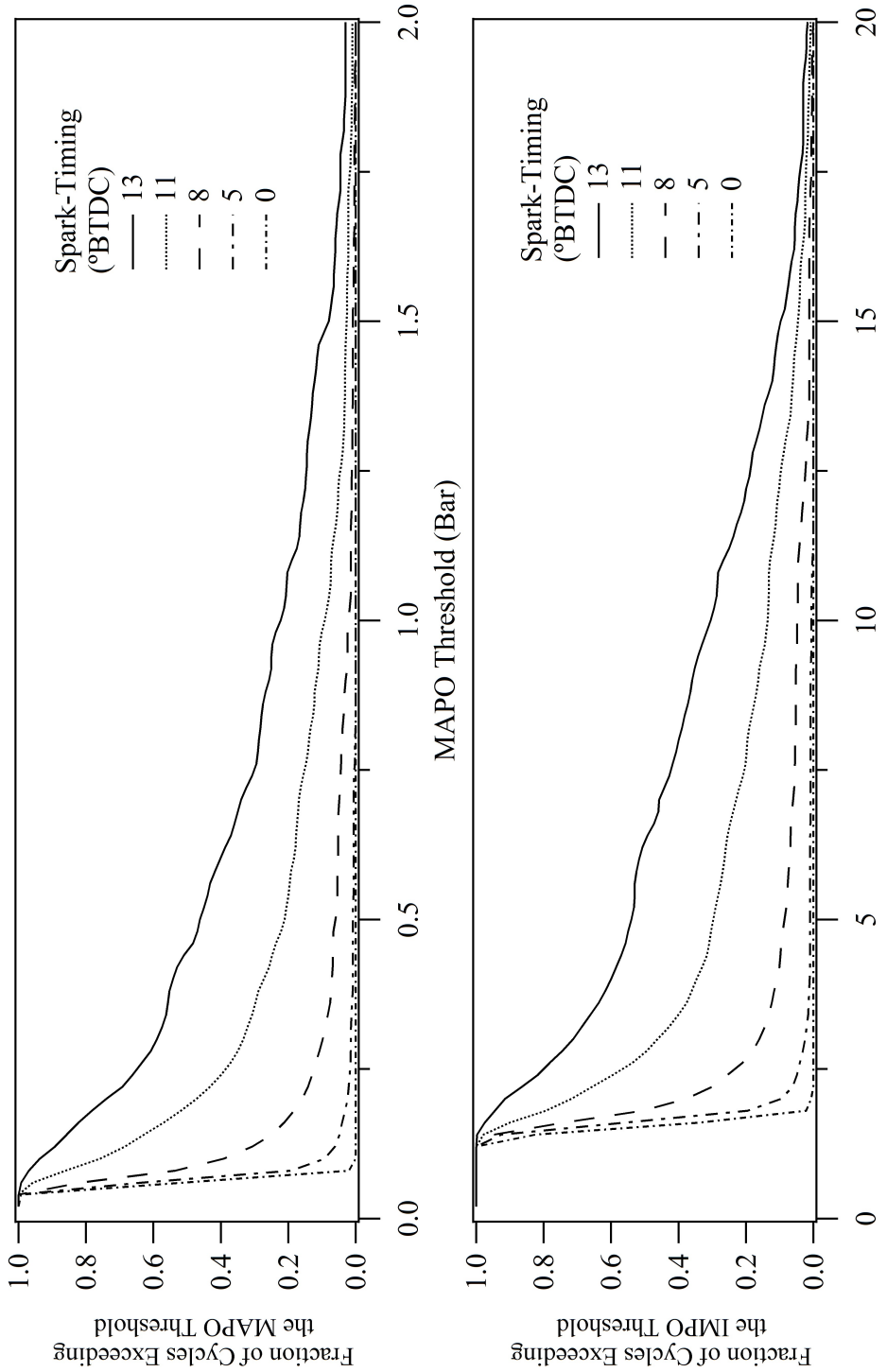

Figure 9.1: Fraction of cycles with MAPO knock intensities exceeding the threshold value.

MAPO Versus IMPO

Figure 9.2 shows the spark-timings for heptanes-in-air which correspond to 5% knock for the thresholds: MAPO = 0.75, IMPO = 10. The similarity between the MAPO and IMPO derived spark-timings (Fig. 9.2) confirm that both techniques are measuring the same phenomenon. The slight differences between the two methods is largely a part of late-cycle oscillations which have a small amplitude (producing a small MAPO), but last for an extended period (producing a large IMPO). Two individual cycles which demonstrate the differences described were chosen from the n-Heptane-in-air case run at a CR of 5.5 and a spark-timing of 8°BTDC, and can be seen in Fig. 9.3 a, which shows a normal knock cycles, and b, which shows a late knock cycle which lasts for an extended portion of the cycle. The late and extended knock (b), which appears to gain significant energy later in the stroke, could be influenced by sensor pipe ringing, which can artificially extend and increase the knocking due to pressure osculations in the transducer adapter.

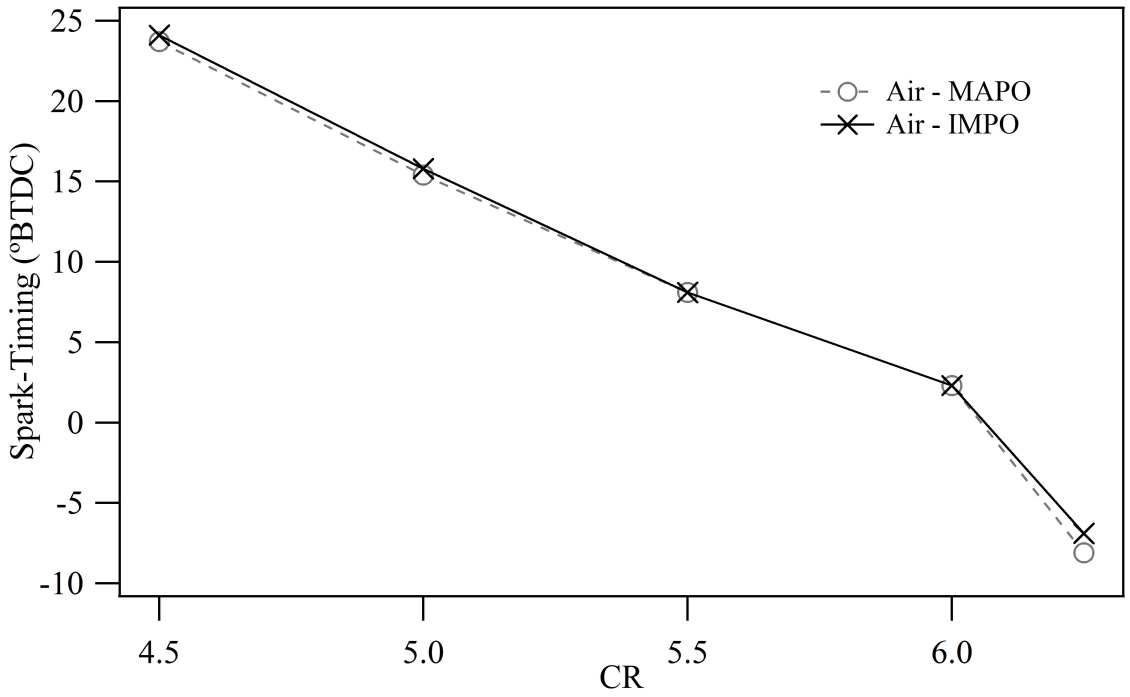

Figure 9.2: Spark-timing corresponding to 5% knock, determined based on IMPO=10 and MAPO=0.75 values.

In his masters thesis,Tschann (2009) addresses the possibility of pipe ringing in the transducer of the CFR as a result of the adapter which is used to mount the transducer in the CFR head. As part of his discussion, Tschann (2009) presents Eqn. 9.1, from Andreas Wimmer (2002),

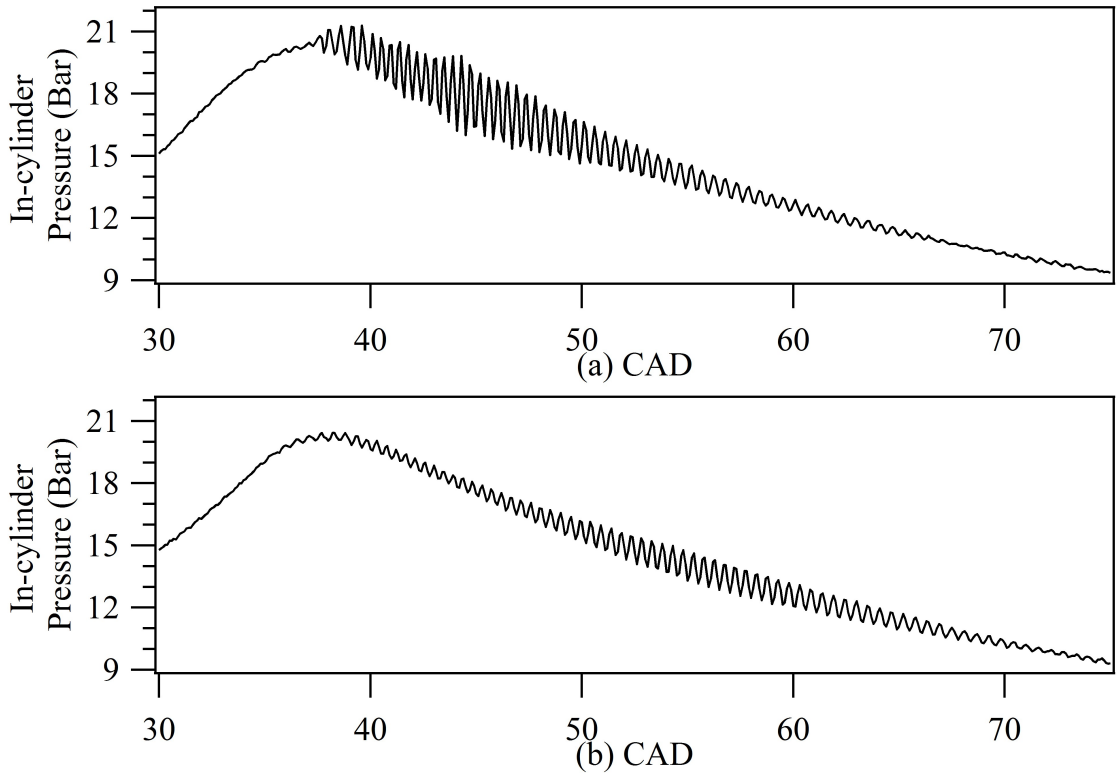

Figure 9.3: Raw in-cylinder pressures for n-Heptane-in-air knocking cycles, run at CR=5.5 and spark-timing = 8°BTDC. (a) shows a normal knocking cycle, (b) shows a late knocking cycle.

$$f = \frac{\sqrt{\gamma RT}}{2\pi}\sqrt{\frac{r^2\pi}{Vl}} \tag{9.1}$$

where f denotes the frequency, γ the ratio of specific heat capacities, R the gas constant, T the temperature, r the radius of the indicating bore, l the length of the indicating bore and V the volume between the measuring surface of the pressure transducer and the top of the indicating bore. However, Tschann (2009) reports that for the CFR system, such ringing would only occur at frequencies above 28kHz, which is well outside the range of the Buttersworth filter (which band-pass filters 5-11kHz), and therefore pipe ringing should not influence the knock intensity computation.

The MAPO and IMPO knock intensity numbers corresponding to the cycles shown in Fig. 9.3 a & b are presented in Table 9.2. Looking at the difference in knock intensity, which indicates the percent decrease between the normal knock (a), and the late knock (b), it can be seen that the MAPO intensity decreases by over 35%, while the IMPO intensity decreases

by only 15.7%. This illustrates the difference between how MAPO and IMPO interpret the knock intensity associated with late knock events, and is the main source of the (minor) discrepancies between MAPO and IMPO intensities seen in Fig. 9.2.

Table 9.2: Comparison of MAPO and IMPO values for cycles with normals versus late knock correspondiong to Fig. 9.3.

	MAPO (Bar)	IMPO (Bar·°)
Normal (a)	0.997	12.93
Late (b)	0.736	11.17
Difference	35.42%	15.70%

Logically, the late knock should be less detrimental to the engine, since it occurs at lower total engine pressure and has smaller amplitude waves (even though the waves last longer). Therefore, it was determined to perform the full analysis using the MAPO values, which better capture the normal knocking. It is important to note that the difference between IMPO and MAPO knock intensities is very minor, and therefore using one versus the other has a negligible effect on the results of the study.

9.2 Experimental Findings

Compositions Tested

Tests were carried out in a manner consistent with the methane tests presented in chapter 7 with Heptane-in-air, wet EGR, and dry EGR. A range of O_2 concentrations were tested for both EGR cases, in an attempt to span the peak thermal efficiency point. Wet and dry EGR test concentrations which were tested are presented in table 9.3. As previously noted, the dilution system has a 2% margin of error. Upper O_2 limits were chosen such that stable engine operation, defined by a low CoV IMEP, was easily achieved. Lower O_2 concentrations were limited by high CoV IMEP values. In addition to the oxycombustion tests, a standard air combustion test was performed to obtain a reference performance.

Each of the seven O_2 concentrations were tested over several CRs, with the maximum CR tested for each case corresponding to the point where any further increase in CR resulted in uncontrollable knocking regardless of spark-timing. The CRs tested for each case are listed in table 9.4. Note that as the O_2 concentration is decreased, the maximum CR increases. Air is limited to very low CRs, as is expected. Wet EGR is also limited to low CRs, with only case wet EGR 3 achieving higher CRs than air. Dry EGR was able to operate at significantly higher CRs across all O_2 concentrations, which, among other things, is a product of its higher specific heat capacity relative to air, and its cooler intake temperature relative to wet EGR. These effects and more are discussed throughout this chapter and the follow chapter on autoignition.

Table 9.3: Wet and dry EGR intake compositions tested.

Case	O_2	CO_2	Water	N_2	Total
Wet EGR					
1	28.4%	31.9%	36.5%	2.2%	99.0%
2	26.3%	32.8%	38.5%	2.2%	99.8%
3	23.6%	33.5%	38.8%	2.2%	98.0%
Dry EGR					
1	29.2%	68.3%	0%	2.3%	99.7%
2	28.0%	69.4%	0%	2.3%	99.6%
3	25.8%	71.6%	0%	2.3%	99.7%
4	22.8%	74.0%	0%	2.2%	99.0%

Table 9.4: Dry EGR intake compositions tested with Heptanes.

Case	CRs Tested
Dry EGR 1	7,7.5,8
Dry EGR 2	7,8,9,10,10.6
Dry EGR 3	9,10,11,12,13,14
Dry EGR 4	13,15,17
Wet EGR 1	4.5,5,5.5
Wet EGR 2	5,6,6.5
Wet EGR 3	6,7,8
Air	4.5,5,5.5,6,6.25

Results

For each composition tested a spark-timing and CR sweep was performed. At each CR tested, spark-timings were tested which spanned conditions from no discernible knock (when possible) to heavy knock. The CR sweep started at a condition which required relatively late spark-timing to induce knock, and was increased until heavy knock could not be avoided, even with a spark-timing significantly after TDC. MAPO and IMPO knock threshold predicted very similar spark-timing limits, as shown in Fig. 9.4. As expected, the spark-timing corresponding to the knock limit occurred later at higher CRs. For a given working fluid and CR, lowing the O_2 concentration resulted in an earlier knock limit spark-timing. Air was limited to the latest spark-timing at every CR.

Thermal efficiencies of all test cases are shown in Fig. 9.5. Immediately it can be seen that, unlike the methane fuel study which found air produced far superior thermal efficiencies, under the proper conditions, dry EGR produces higher thermal efficiency than Heptane-in-air. Shockingly, dry EGR was able to produce *higher* thermal efficiency when

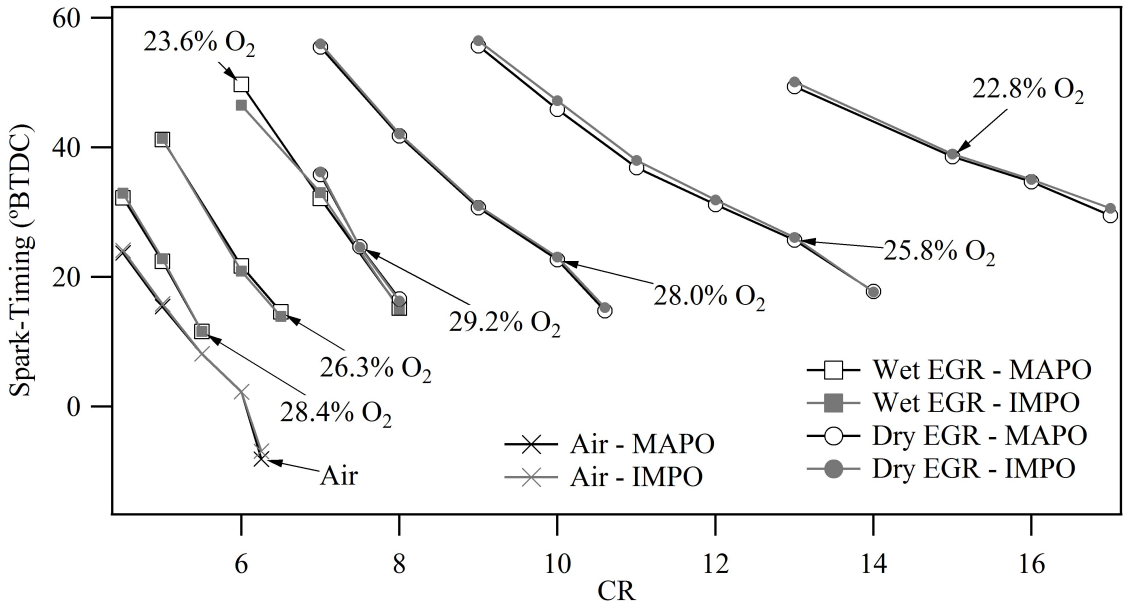

Figure 9.4: Spark-timings corresponding to the knock limit for MAPO and IMPO thresholds.

operating on heptanes (peak of 26.0%) than when running on methane (peak of 25.0%)! This higher efficiency is not seen in air cases, and must be attributed to a different combustion phenomenon occurring, allowing greater power extraction at the same, and even lower, CRs. The topic is discussed in detail in chapter 10.

Similarly to the methane cases, wet EGR produces the lowest thermal efficiencies, which is not unexpected due to the very minor increase in CR it was able to achieve relative to air. Unlike the methane cases, which produced a local thermal efficiency maximum as the O_2 concentration was altered, for a given working fluid (wet or dry EGR) the maximum thermal efficiency continues to increase as the O_2 concentration is reduced. However, the continued increase of thermal efficiency through the reduction of O_2 is ultimately limited by increasing CoV IMEP levels.

IMEP values corresponding to the knock threshold for each test point are shown in Fig. 9.6. As with the methane cases, dry EGR produces the highest IMEP of all cases, even at its lowest O_2 concentrations, however, all cases fail to reach the IMEP levels achieve with methane combustion. Wet EGR produces the lowest IMEP, despite having cases with significantly higher O_2 concentration than air. The low IMEP is an effect of both large wall heat loses and poor knock resistance due to the high intake temperature. Interestingly, for both wet and dry EGR cases the power loss associated with decreasing the O_2 concentration can be compensated for by increasing the CR.

The ability of increased CR to compensate for reduced O_2 concentration results in a system whose peak thermal efficiency does not have a local maximum with respect to O_2

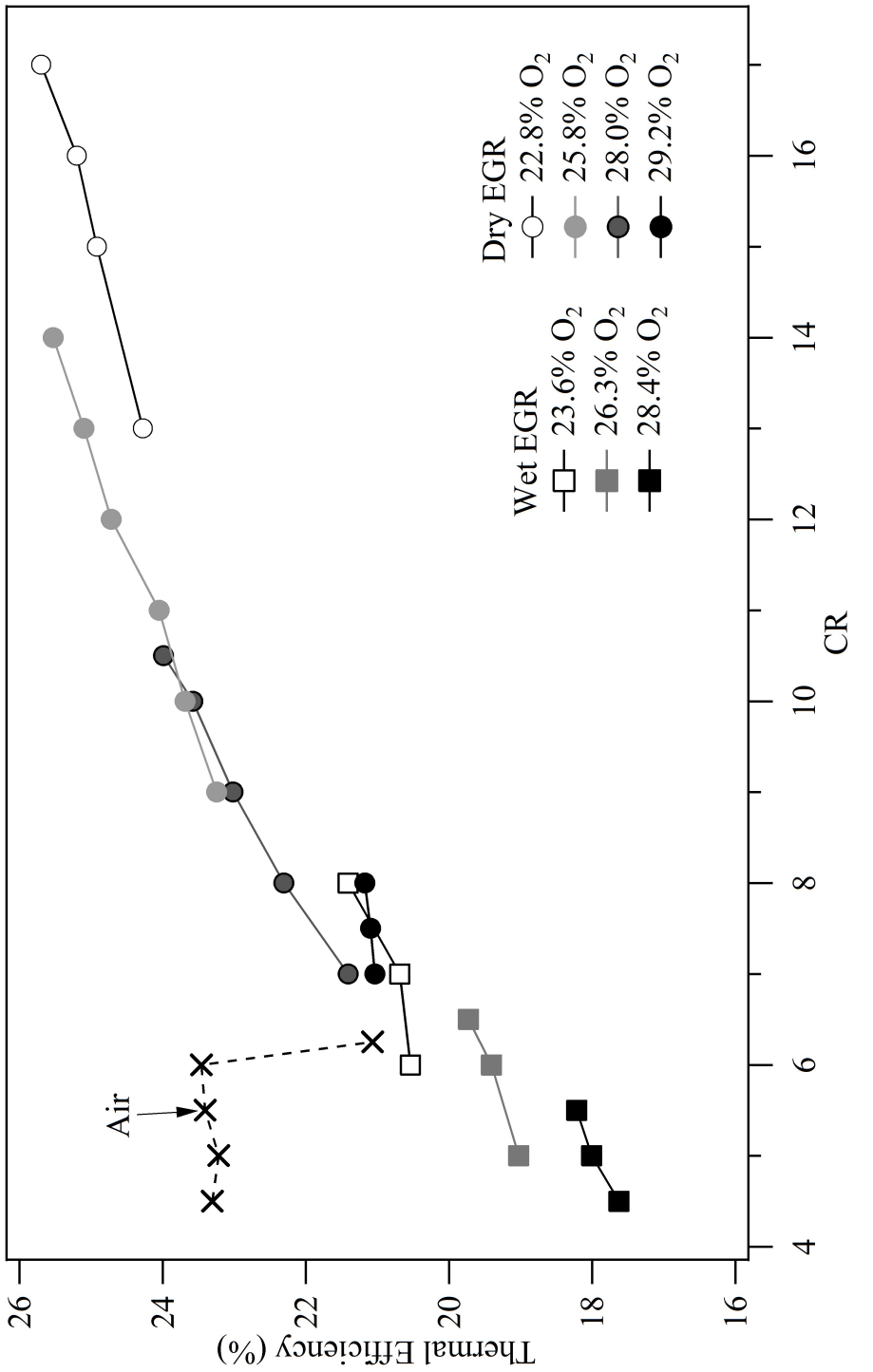

Figure 9.5: Thermal efficiency at 5% knock, determined based on MAPO values.

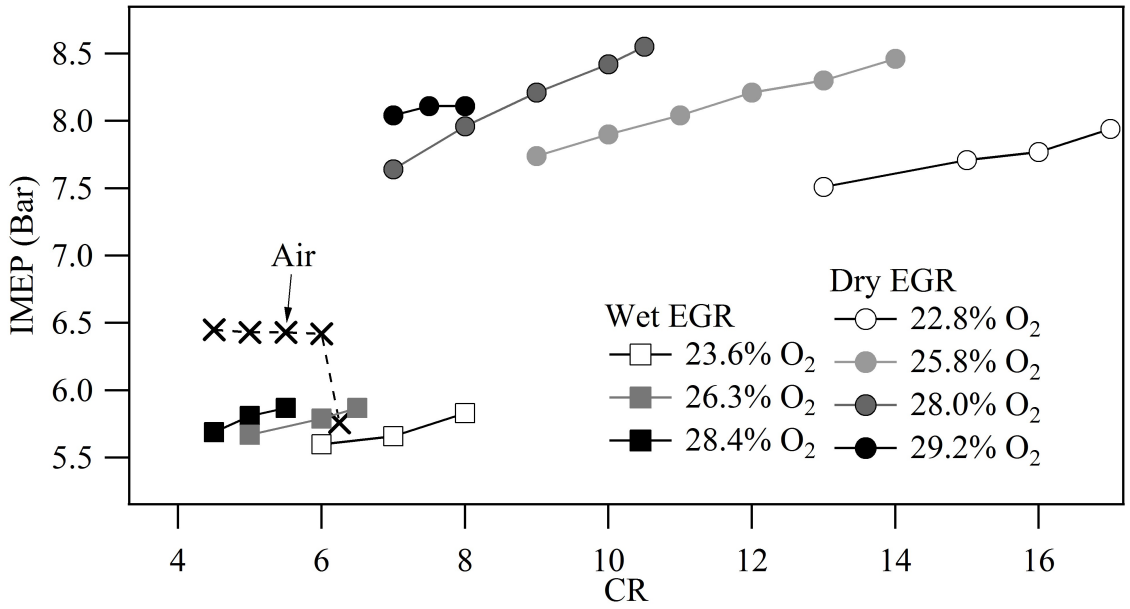

Figure 9.6: IMEP values for all cases corresponding to the knock threshold at each point for both MAPO and IMPO limits.

concentrations, rather the efficiency continues to increase with decreasing O_2 concentration. Ultimately what constrains the operating points is the CoV IMEP, which eventually rises to unacceptable levels, as shown in Fig. 9.7. Cases with higher flames speeds (such as air and EGR cases with high O_2 concentrations, such as wet EGR 3 and dry EGR 4) show significant increases CoV IMEP values as the CR increases. As the flame speed decreased (the O_2 concentrations decrease) the CoV IMEP initially increases with CR, but then decreases. The effect can be easily seen in the cases wet EGR with 23.6% O_2 and dry EGR with 25.8% O_2. As the O_2 concentration is decreased even further, the CoV IMEP shows only a decreasing trend as CR is increased, as seen in the dry EGR with 22.8% O_2 curve. The reversal of trends, where increasing CR increases CoV IMEP for high flame speed cases and decreases CoV IMEP for low flame speed cases indicates that controlled and stable autoignition begins to occur at higher CRs. Based on these trends it is feasible that the dry EGR case with 22.8% O_2 could reach a reasonable CoV IMEP and even higher thermal efficiency if it was possible to further increase the CR beyond the engines limit of 17.

The combustion efficiency of all cases was found to be quite poor across all tests, as shown in Fig. 9.8. Air produces the highest combustion efficiency at 97-98%. Unlike the methane study, wet EGR does not produce better combustion efficiency than dry EGR does. There is a clear reduction in combustion efficiency as the O_2 concentration is decreased. In addition, the majority of cases show decreasing combustion efficiency as the CR is increased. The CR influence is likely the result of increased mass in the crevices at higher CRs due to the increased cylinder pressure at the point of flame extinction.

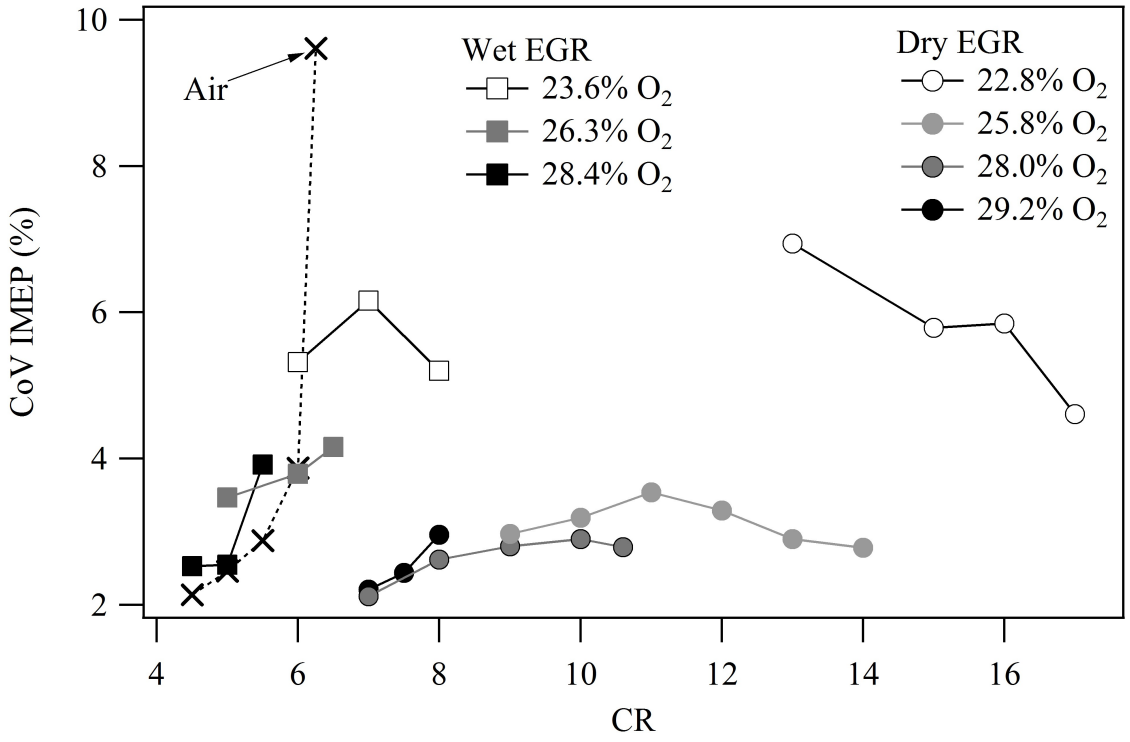

Figure 9.7: CoV IMEP values for all cases corresponding to the knock threshold at each point.

Interestingly the combustion efficiency follows trends almost inversely related to the thermal efficiency shown in Fig. 9.5. The fact that dry EGR with 22.8% O_2 had only around 90% combustion efficiency and yet was able to achieve higher thermal efficiency than air is even more surprising. Clearly the advantages associated with dry EGR are very significant, resulting in a high enough thermal efficiency that even a loss of 10% of the fuel energy does not reduce the thermal efficiency below air combustion.

Theoretical Thermal Efficiency

In chapter 7 it was found that the differences in thermal efficiency when combustion methane in air, wet EGR, and dry EGR working fluids could be largely explained by the shift of the ratio of specific heats γ. For each test case the average γ value was determined and used to determine the corresponding theoretical thermal efficiency (Eqn. 7.1). Values were computed based on the tested spark-timing which corresponded most closely to the spark-timing knock limit. Table 9.5 lists the computed values for the minimum and maximum CRs tested for each O_2 concentration tested.

Note that the values of γ show very little variation based on O_2 concentration or CR, with

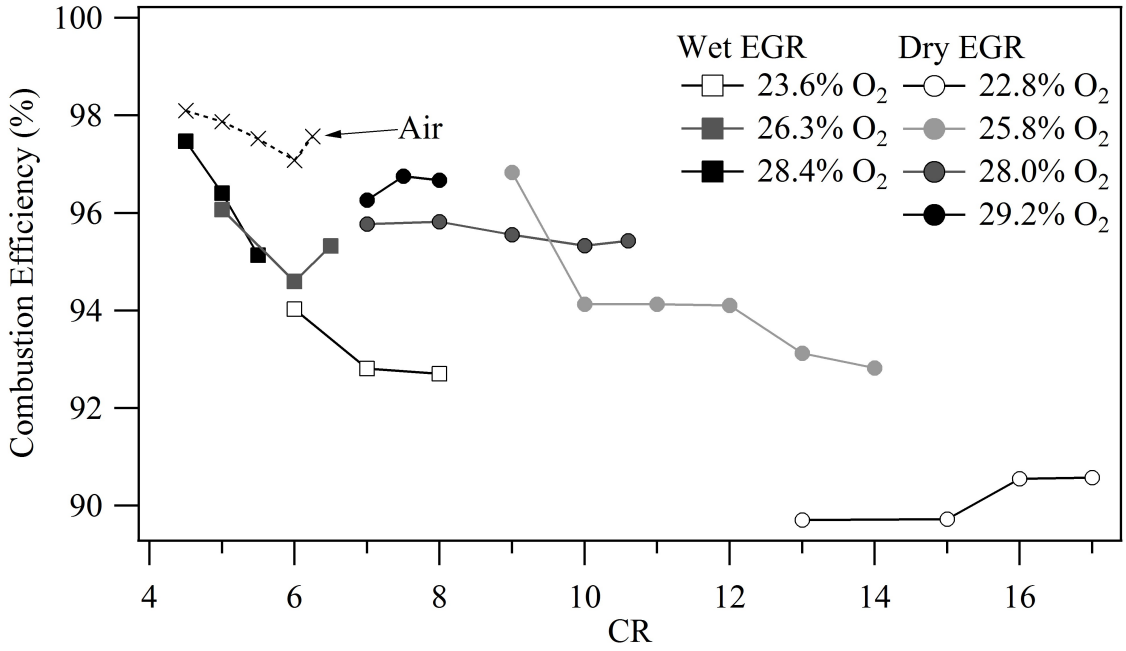

Figure 9.8: Combustion efficiency for all cases corresponding to the knock threshold at each point.

Table 9.5: γ values for minimum and maximum CRs tested and corresponding spark-timings at each test point.

	Air		*Wet EGR*					
			28.4% O_2		26.3% O_2		23.6% O_2	
CR	6		4.5	5.5	5	6.5	6	8
ST (°BTDC)	-1		33	6	30	14	50	14
γ	1.294		1.207	1.212	1.211	1.214	1.212	1.216
	Dry EGR							
	29.2% O_2		28.0% O_2		25.8% O_2		22.8% O_2	
CR	7	8	7	10.6	9	14	13	17
ST (°BTDC)	35	20	55	15	55	20	50	31
γ	1.200	1.203	1.198	1.202	1.201	1.204	1.206	1.208

less than 1% variation between the various wet and dry EGR cases. Using these values, as well as computed values for the remaining CRs, the theoretical maximum thermal efficiencies were computed and are shown in figure 9.9.

Comparing Figs. 9.9 and 9.5 overall there is relatively good agreement between the theoretical maximum thermal efficiency and the measured thermal efficiency. Wet EGR pro-

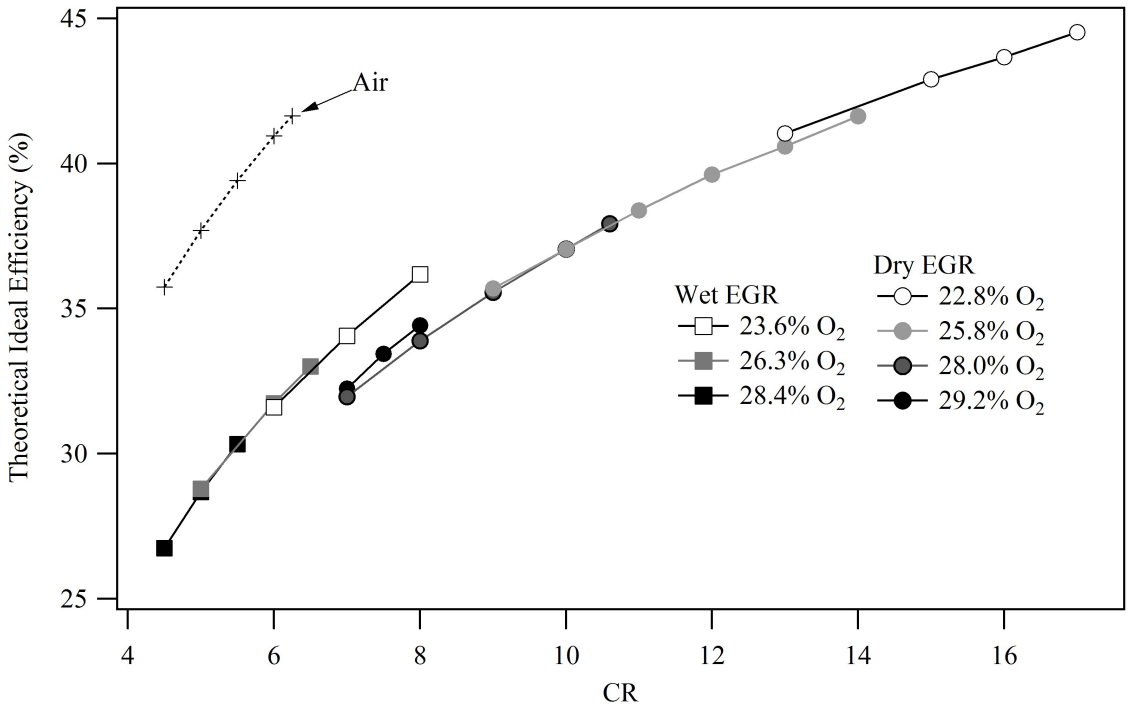

Figure 9.9: Theoretical maximum thermal efficiencies for each of the test points taken.

duced lower thermal efficiency in the experiments,as is predicted by the reduced theoretical maximum thermal efficiency due to the low γ values and low CRs. In addition, the theoretical curves predict that dry EGR should be able to surpass the thermal efficiency of air at the highest CRs. Though these general trends are in agreement, there are many additional points which require further investigation. The theoretical thermal efficiency of air increases as the CR is increased, as expected, but the measured thermal efficiency was constant across all CRs, eventually dropping off sharply at CR=6.25. This is a product of the knock limitation of air, which requires later and later spark-timing as the CR is increased to avoid excessive pressure and temperature. The combined result of increased CR, which is desired, and decreased spark-timing, which is a disadvantage, is a constant thermal efficiency. It is very interesting that this trend is not present in the EGR runs, which show increased thermal efficiency as the CR is increased. This appears to be a product of controlled autoginition events, in which small portions of the unburned gas auto-ignite, but produce a small enough ROHR that significant knock is not generated. The concept of controlled auto-ignition is discussed in depth in chapter 10.

HCCI Limit

When operating both dry and wet EGR at all O_2 concentrations it was found that at high CRs the mixture would autoignite without any spark assistance - resulting in the engine operating in an HCCI mode. For any of the higher CRs presented the engine would sustain very delayed HCCI combustion with no measurable knock production. The spark-timing could then be advanced to the point that the spark controlled the timing of the main ignition event, and it was still possible to operated below the knock threshold. Increasing the CR would advance the timing of the HCCI event, which would start to produce some measurable knock even with a spark-controlled ignition. Ultimately, it was found that the maximum possible CR was limited by an HCCI condition with significant knock. Because the engine was operating in an HCCI mode it was not possible to retard the spark (the spark could be turned off with no effect on the combustion) to reduce the knock intensity. An example is the wet EGR with 28.4% O_2 at CR=5.5 case, which showed relatively constant power, efficiency, and knock intensity across the majority of tested spark-timings, as shown in table 9.6. For these cases, the engine is operating in HCCI mode, with the spark resulting in little to no effect. However, since the HCCI does not have accompanying knocking, it is possible to increase the spark timing and return to a traditional SI state which eventually becomes knock limited.

Table 9.6: Engine properties across spark-timings for wet EGR with 28.4% O_2 at a CR of 5.5.

ST	MAPO	IMPO	IMEP	CoV IMEP	Thermal Efficiency
-15	0.7%	0.7%	5.05	16.03	15.7%
-12	1.2%	1.0%	5.11	15.27	15.9%
-9	1.4%	0.9%	5.16	13.56	16.0%
-6	1.8%	1.6%	5.21	12.35	16.3%
-3	0.9%	1.0%	5.32	10.58	16.5%
0	1.8%	1.4%	5.40	8.95	16.7%
3	0.6%	0.6%	5.47	7.27	17.0%
6	1.6%	1.2%	5.59	5.84	17.3%
9	2.6%	1.9%	5.76	4.58	17.8%
12	5.4%	5.5%	5.89	3.81	18.3%

9.3 Conclusions

The performance limits of heptanes combustion in air, dry EGR, and wet EGR have been compared. All cases were knock limited, with spark-timing used to adjust the intensity of the knock. As the CR was increased EGR cases ultimately reach a point of HCCI-type

autoignition independent of spark, which limited the upper CRs which could be tested. Dry EGR was able to operate at very high CRs, and produced a peak thermal efficiency of over 25.5%, surpassing the peak thermal efficiency of air, which managed 23.4%. Wet EGR performed the worst of all the fluids, managing to produce only 21.3% thermal efficiency which was additionally coupled with high CoV IMEP. Wet EGR was limited to less than 20% thermal efficiency when a CoV IMEP of less than 5% was required. Shockingly, dry EGR produced higher thermal efficiency when combusting heptanes than it did when combusting methane, indicating a significantly different combustion process, which is discussed in chapter 10.

Decreasing the O_2 concentration of the EGR runs permitted the engine to operate at higher CRs and reach higher thermal efficiency, however this corresponded with decreasing combustion efficiency and increasing CoV IMEP. However, at low O_2 concentrations the CoV IMEP decreased with increasing CR. Wet EGR was limited to low CRs due to its elevated intake temperatures, and without the ability to reach high CRs the CoV IMEP increased quickly as the O_2 concentration was decreased. Dry EGR was able to operate at much higher CRs than wet EGR due to its lower intake temperature and higher specific heat, and as such CoV IMEP was kept low for most cases. At the lowest O_2 concentration of 22.8% the CoV IMEP was higher than desired, but fell consistently as the CR was increased. Ultimately the engine CR limit of 17 was reached prior to reaching a point of uncontrollable knock, and thus it is theorized that reasonable CoV IMEP and higher thermal efficiency could be achieved.

Combustion efficiency was low for all cases, and decreased strongly with decreased O_2 concentration. In addition, the combustion efficiency continued to decrease as the CR was increased, representing a significant source of thermal efficiency loss and a major cleanup concern at the lowest O_2 concentrations.

Theoretical thermal efficiency largely correlates with the findings based on the ratio of specific heats for each case and the CRs which were able to be run. One point of discrepancy between the theoretical thermal efficiency trends and experimental results was that increasing CR did not improve the experimental thermal efficiency of air. In addition, theoretical thermal efficiency limits predict that for a given working fluid and CR the thermal efficiency should be constant regardless of O_2 concentration. This correlation is not present in the experimental results. A detailed investigation of the reasons for these discrepancies, and predictions for performance limits at higher CRs than could be tested are presented in chapter 10.

Chapter 10

Knocking Limits of Oxycombustion

The ability of dry EGR to produce higher thermal efficiencies when combusting heptanes than when combusting methane requires a more detailed analysis. In this section many features of the results, including point-by-point plotting of IMEP, MAPO, and peak ROHR, are examined for individual cases and across CRs, O_2 concentrations, and working fluids. Air is used as a reference of 'typical' combustion.

10.1 Cycle-by-Cycle Analysis

Plotting curve features on a point-by-point basis (i.e. every combustion cycle has a certain aspect of it quantified and plotted, such as the IMEP vs. the location of the peak ROHR) can be useful in identifying characteristics of curves which could be lost in the averaging of hundreds of cycles. Therefore, a significant number of plots in this section present point-by-point results. In some cases point-by-point does not show any uniqueness, but it is important to identify these cases with no uniqueness to confirm that the unique cases which are identified are truly capturing additional aspects of the combustion process. Individual points are gathered for each curve by analyzing each curve for its corresponding properties.

For example, Fig. 10.1 shows 5 different ROHR curves for individual cycles when operating the engine on air with a CR of 6 and a spark-timing of 4 °ATDC. From each of these curves the unique location of the maximum (peak ROHR), as well as its location (location of peak ROHR), is recorded. Additionally, the pressure trace corresponding to each curve is analyzed to determine IMEP, and MAPO values.

Location of Peak ROHR

Under normal conditions, it is expected that moving the location of peak ROHR closer to TDC will increase IMEP. Figure 10.2 (a) shows the expected trend is indeed present in the air experiments, as there is a strong correlation between the location of the peak rate of heat release and IMEP. Dry EGR also shows a strong correlation between location of peak

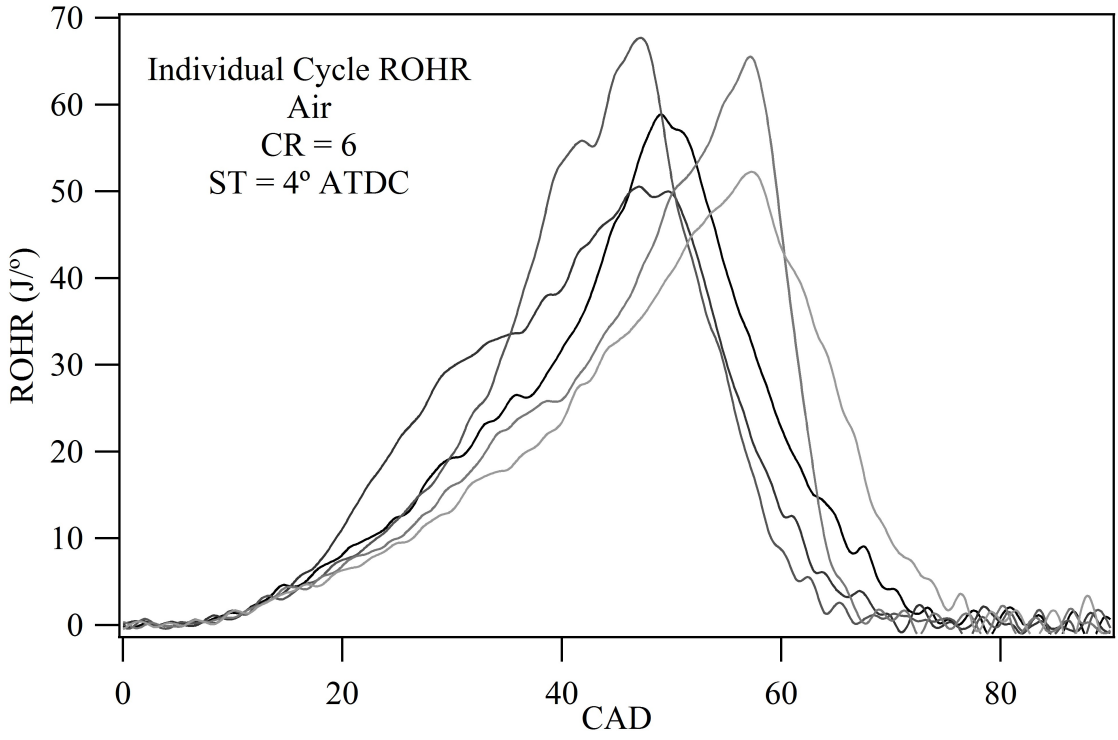

Figure 10.1: Sample individual ROHR curves from combustion with heptanes-in-air.

ROHR and IMEP as shown in Fig. 10.2 (b), though the changes due to spark-timings are less pronounced. For both cases it is clearly beneficial to achieve peak ROHR as early as possible to maximize IMEP.

Limiting the location of the peak ROHR is the correlation between MAPO and location of peak ROHR, show in Fig. 10.2(c) and (d). Air, shown in Fig. 10.2(c), has a significant amount of scatter, but apppears to reach a threshold at around 40°ATDC, where any results with earlier peak ROHR produce some level of knock, with he level of knock increasing as the location of peak ROHR is shifts closer to TDC. Dry EGR, shown in Fig. 10.2(d), does not appear to have this threshold value, rather it appears that the location of peak ROHR can be correlated to the upper limit of the MAPO, but there remains many points near, or at, zero knock. The ability of dry EGR to have cycles with such early location of peak ROHR that show little or no knock indicates is a unique and important aspect of the ability of EGR to produce high thermal efficiencies with low octane fuels.

The maximum magnitude of the ROHR (peak ROHR) is an additional aspect of the combustion cycle which is expected to be strongly correlated to both MAPO and the location of the peak ROHR. For example, since the area under the ROHR curve (net HR) is constant for all cases (same amount of fuel every cycle) it is expected that cases with very early location of peak ROHR will have large magnitudes (the curves will be narrower with a

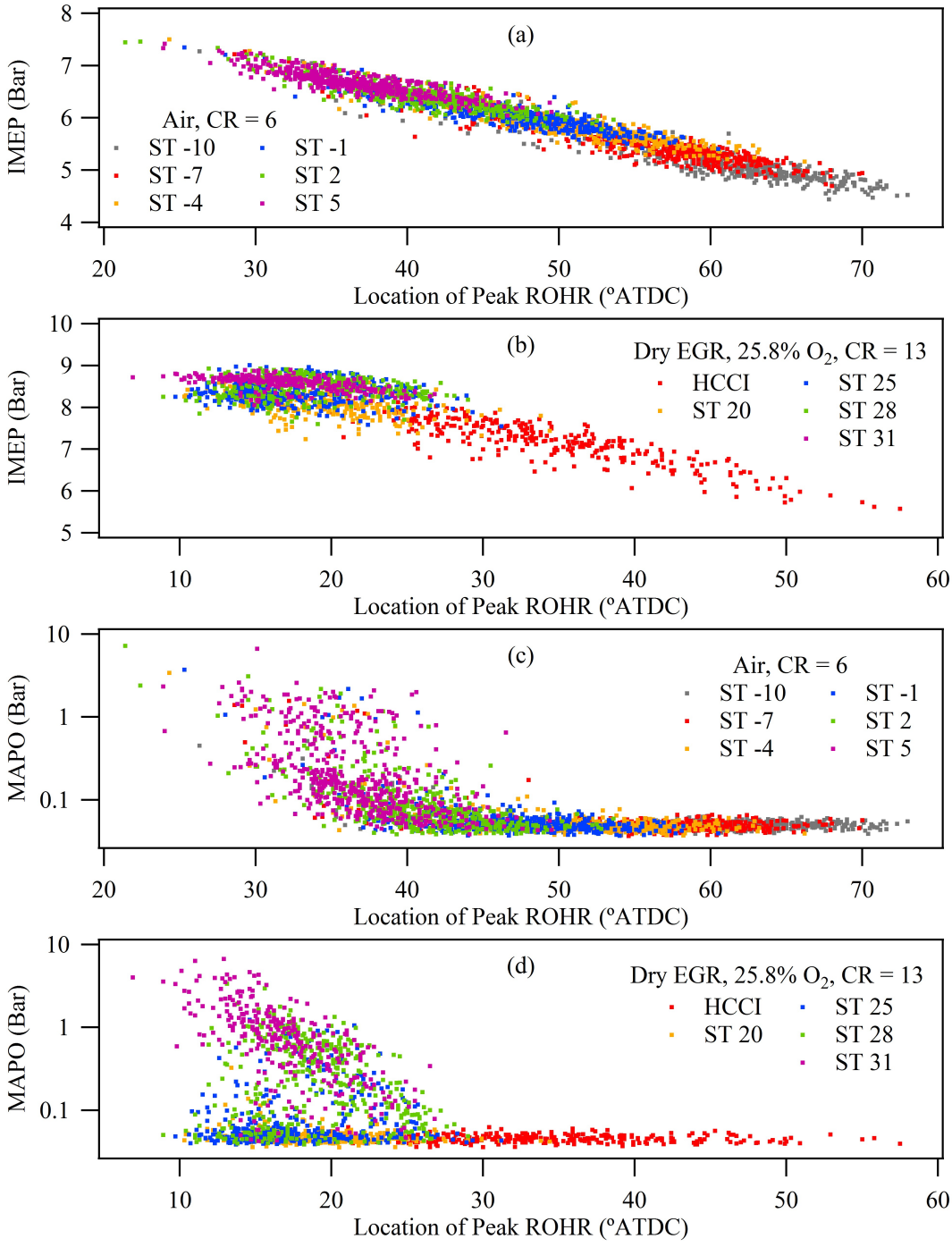

Figure 10.2: IMEP and MAPO values vs. the location of the peak ROHR for an air and dry EGR case.

higher maximum) while cases with later locations of peaks will have wider and lower curves which produce lower peaks. In addition to corresponding to early location of peak ROHR, very large ROHR is expected to be strongly associated with autoignition and knock intensity. Figure 10.3 shows the clear correlation between MAPO and peak ROHR for dry EGR.

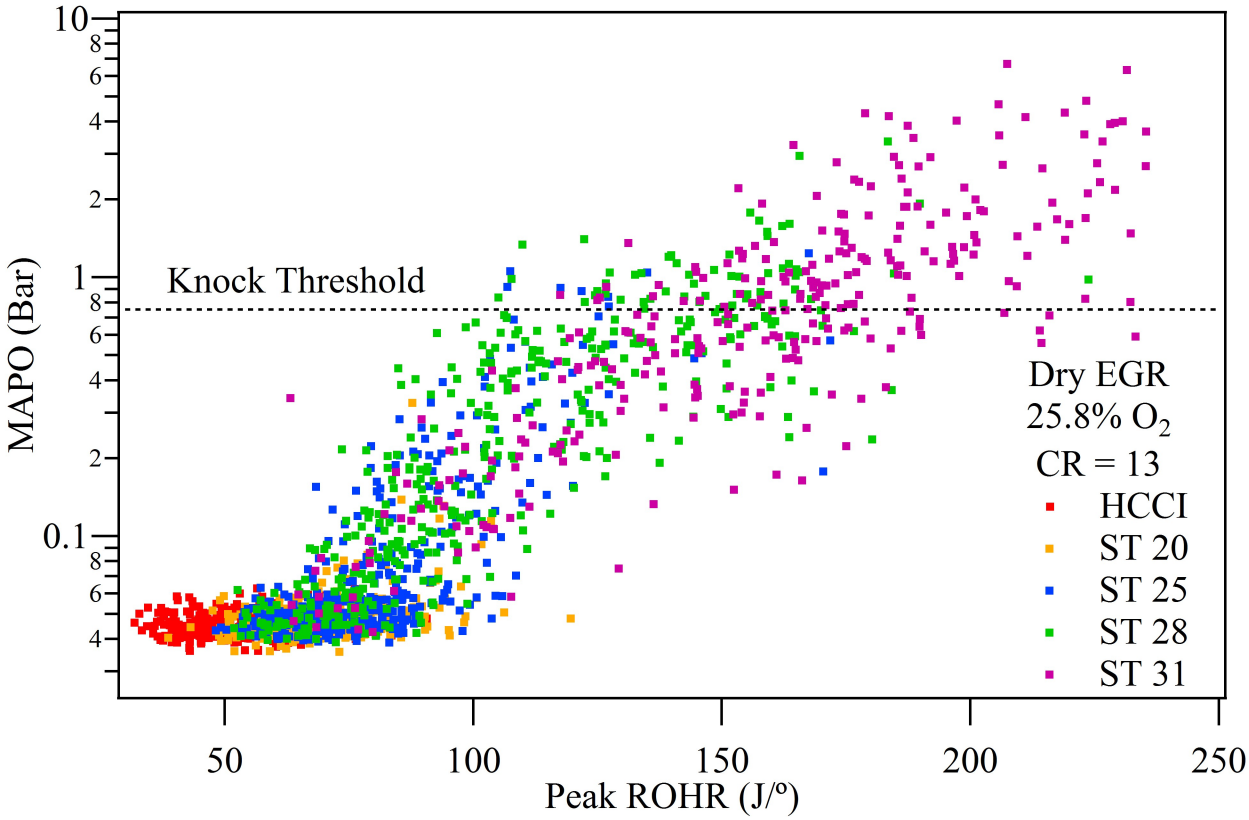

Figure 10.3: MAPO vs. peak ROHR for dry EGR. There is a clear correlation between knock intensity and the peak ROHR.

Plotting the magnitude of the peak ROHR vs. the location of the peak for air shows the expected trend, with the individual peak ROHR data points producing a $\frac{1}{x}$ function profile with earlier location of peak ROHR. However, the dry EGR case, seen in the Fig. 10.4(a) below produces two distinct curves: one which shows a similar $\frac{1}{x}$ function profile while the other remains at a nearly constant level despite the decreasing location of peak ROHR. This deviation appears to correspond to two different flame progressions: (1) the lower curve, with relatively constant peak ROHR appears to correspond to normal flame propagation, while (2) the upper curve corresponds to autoignition events which dramatically increase the ROHR, particularly early in the cycle.

It should be noted that Fig. 10.2(a) and (b) indicate that IMEP is primarily a function of location of peak ROHR, and therefore even the lower portion of the curve in Fig. 10.4(b),

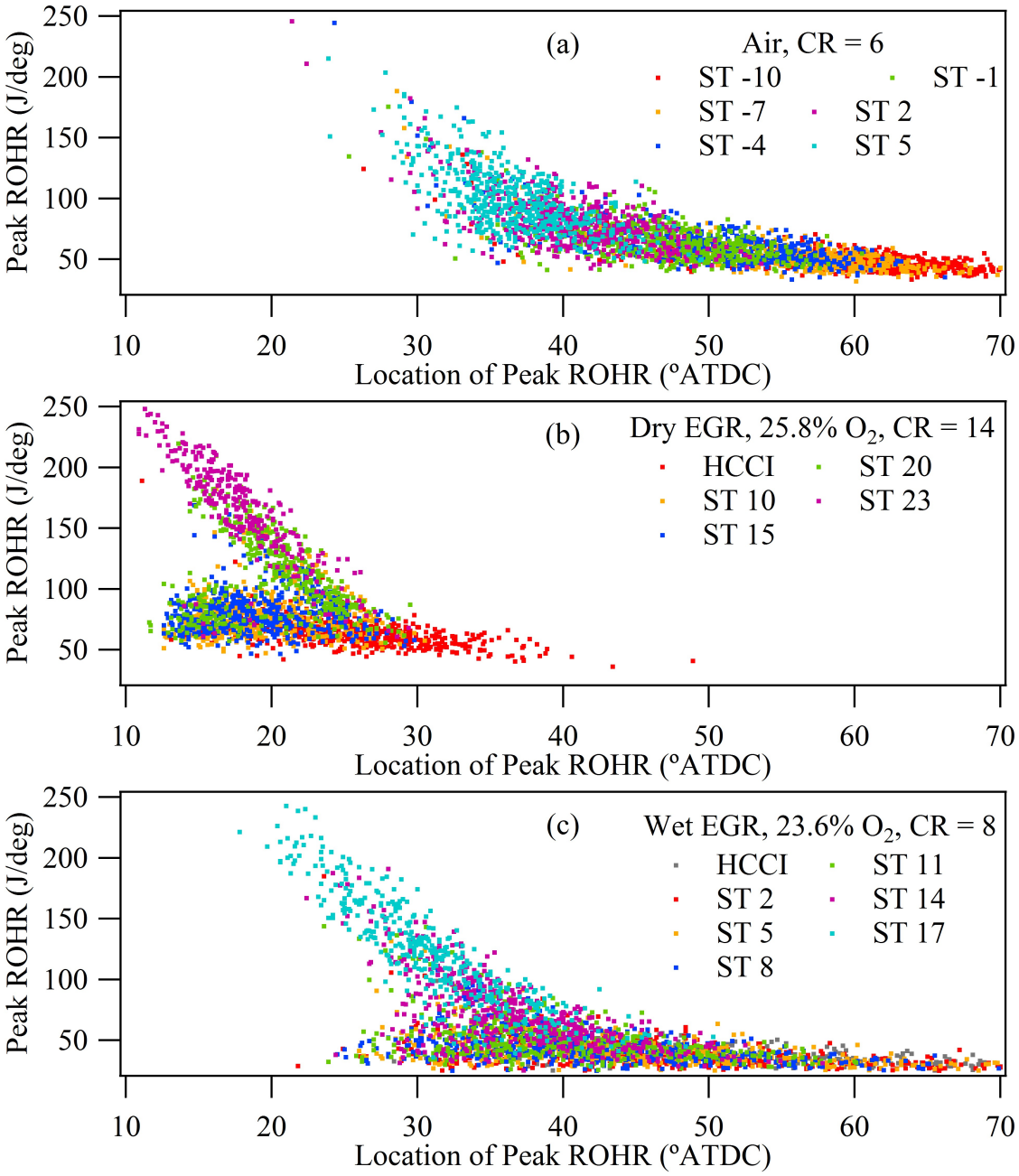

Figure 10.4: Peak ROHR values vs. the location of the peak ROHR for air, dry EGR, and wet EGR.

which produce low peak ROHR values but at an early location, correspond to good IMEP values.

The source of the early yet low peak ROHR data points seen in dry EGR can be more

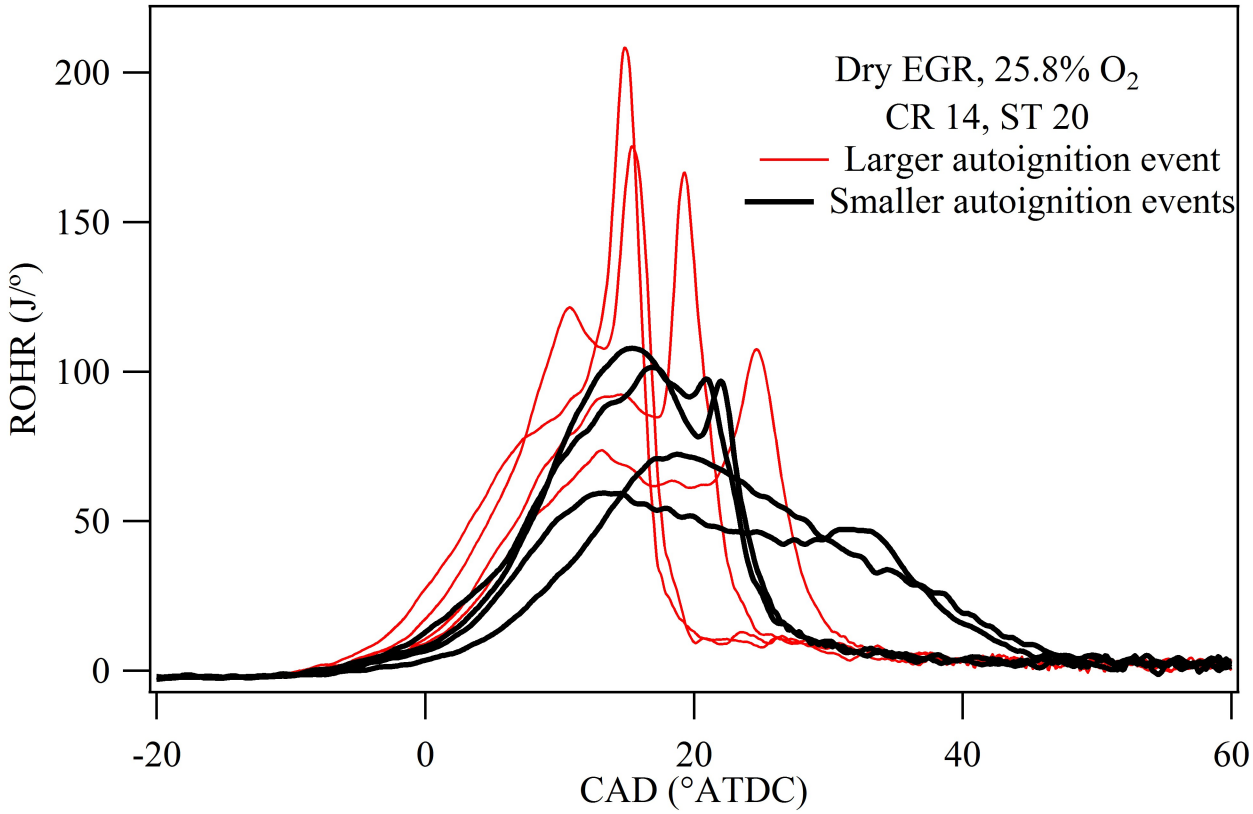

Figure 10.5: Dry EGR produces two distinct ROHR profiles: 1) large autoignition events which produce large peak ROHR, the magnitude of which are highly proportional to the location of the peak. 2) Small autoignition events which occur later in the cycle, producing local maximum in the ROHR which do not exceed the early cycle ROHR magnitude.

clearly understood by considering individual cycle characteristics. These lower peak ROHR points with corresponding early location of peak suggest a controlled autoignition event, in which the ROHR is relatively constant for an extended period of the cycle. Figure 10.5 depicts several individual ROHR curves, including curves which were present on both the higher and lower curves of Fig. 10.4 (b).

In general, the curves illustrating strong autignition events result in a large peak ROHR (often slightly later in the cycle). The magnitude of the peaks caused by these large autoignition events is strongly correlated to the time in the cycle at which the autoignition occurs, with earlier autoignition points producing the largest peaks. This is expected since large autoignition events consume the majority of unburned fuel and O_2, and earlier in the cycle these is more unburned gases available. The same characteristic is seen commonly in air cases. The smaller autoignition curves show that under certain conditions the curves reach their peak ROHR relatively quickly, and is then followed by additional minor autoignition

events (which appear as additional local maximums after the main peak). These minor autoignition events produce good IMEP without producing significant knock. Note that the curves in Fig. 10.5 do no capture all of the properties and events which occur from cycle to cycle; the purpose is to illustrate a unique property which is not noted in heptanes and air combustion.

CR Effects

Based on Fig. 10.3, 10.4, and 10.5 there is a clear association between MAPO and knock intensity. This correlation exists regardless of the location of the peak ROHR, but for most significant autoignition cases the peak ROHR and location of peak ROHR are correlated. It is expected that CR would not significantly affect this correlation. Figure 10.6 shows MAPO versus location of peak ROHR for dry EGR with 25.8% O_2 at 6 different CRs, and while the general trend does hold, it is interesting to note that the shape of the curve is not constant. Since all of the figures are the same size and have the same axis ranges, they can be compared to one another relatively easily, and it is clear that as the CR increases, the range of peak ROHR which corresponds to knocking threshold (indicated by the horizontal dashed line at MAPO = 0.75), increases. Therefore, peak ROHR values which correspond to significant knocking at CR 9 result in almost no knocking at CR 14. This is an unexpected result, since at higher CRs autoignition becomes more likely and the volume of the cylinder is reduced which should only serve to enhance the strength of any knocking produced from autoignition events.

The reason for the decreased knock intensity at a given peak ROHR as the CR is increased can be explained by examining the average ROHR and bulk temperature curves for the extreme CR cases, as shown in Fig. 10.7. What should be noted is that even though the CR 14 case has a much higher peak ROHR, the bulk temperature is lower than the CR 9 case throughout the curve, which is a result of the later spark-timing of the higher CR case. Since knock is primarily correlated with temperature this explains why as the CR is increased the peak ROHR at which significant knock begins to occur increases. The same effect is observed in air and wet EGR cases.

Air shows the same trend between MAPO and peak ROHR but there is a much greater quantity of scatter and the trend is harder to identify, as shown in Fig. 10.8. The increased scatter is a produce of the lower knock resistance of air, making any auto-ignition event more likely to produce large quantities of knock. Therefore there are almost no peak ROHR points which produces some measurable knock that do not also produce some cases with knock intensity above the threshold value. This is in contrast to dry EGR, which at higher CRs produced peak ROHR regions which clearly corresponded to some knocking, but did not have any points which exceeded the threshold value.

Based on the understand of the effect CR can have on ROHR and bulk temperature, a more thorough investigation of CR on the two distinct ROHR profiles (identified as the reason for two distinct curves in Fig. 10.4(b) and shown on a cycle by cycle case in Fig. 10.5) can be carried out. Figure 10.9 shows 6 plots of peak ROHR versus location of peak

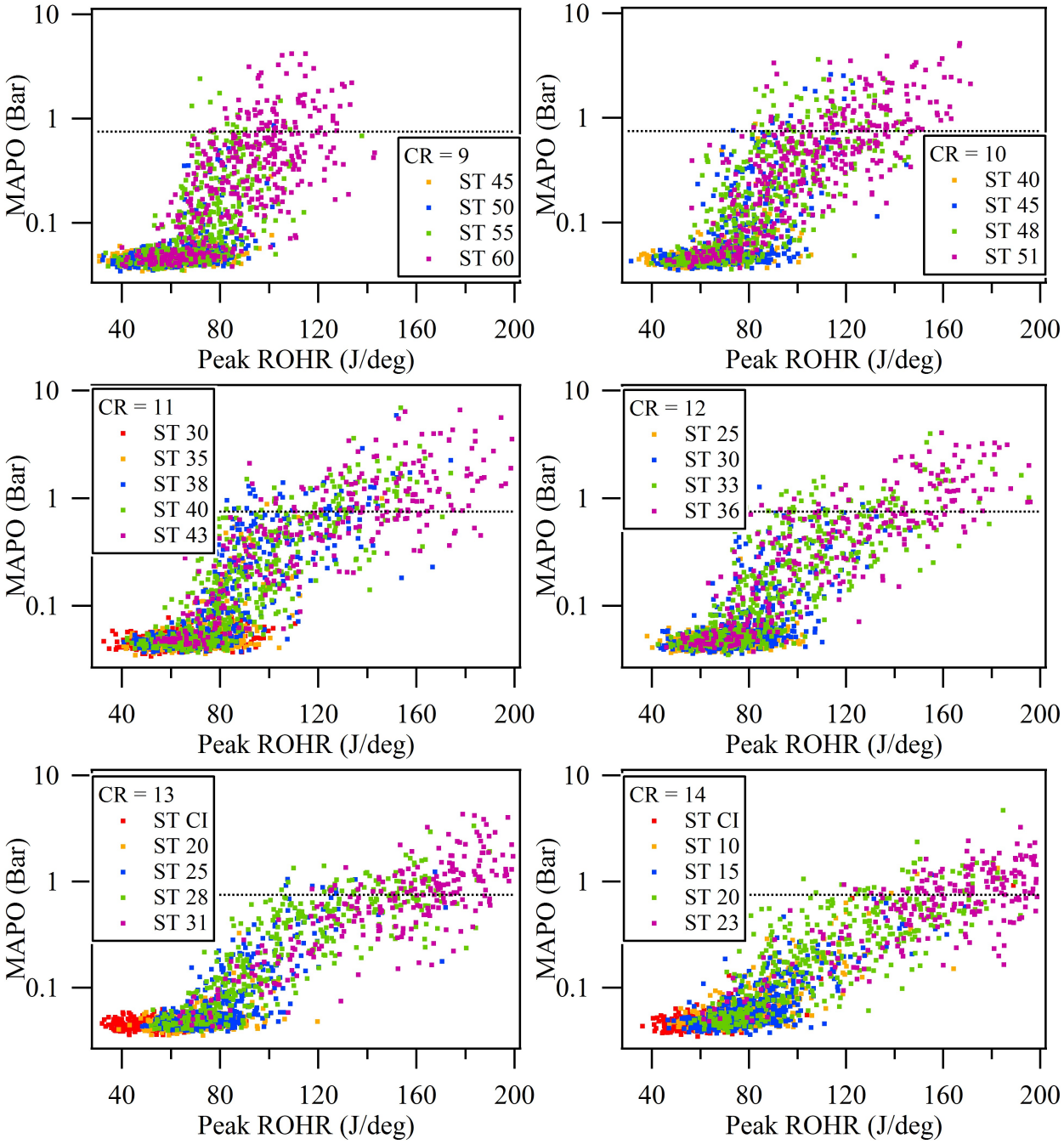

Figure 10.6: MAPO versus peak ROHR for dry EGR with 25.8% O_2 concentration across tested CRs.

ROHR at various CRs for dry EGR with 25.8% O_2. What is immediately noticed is the two

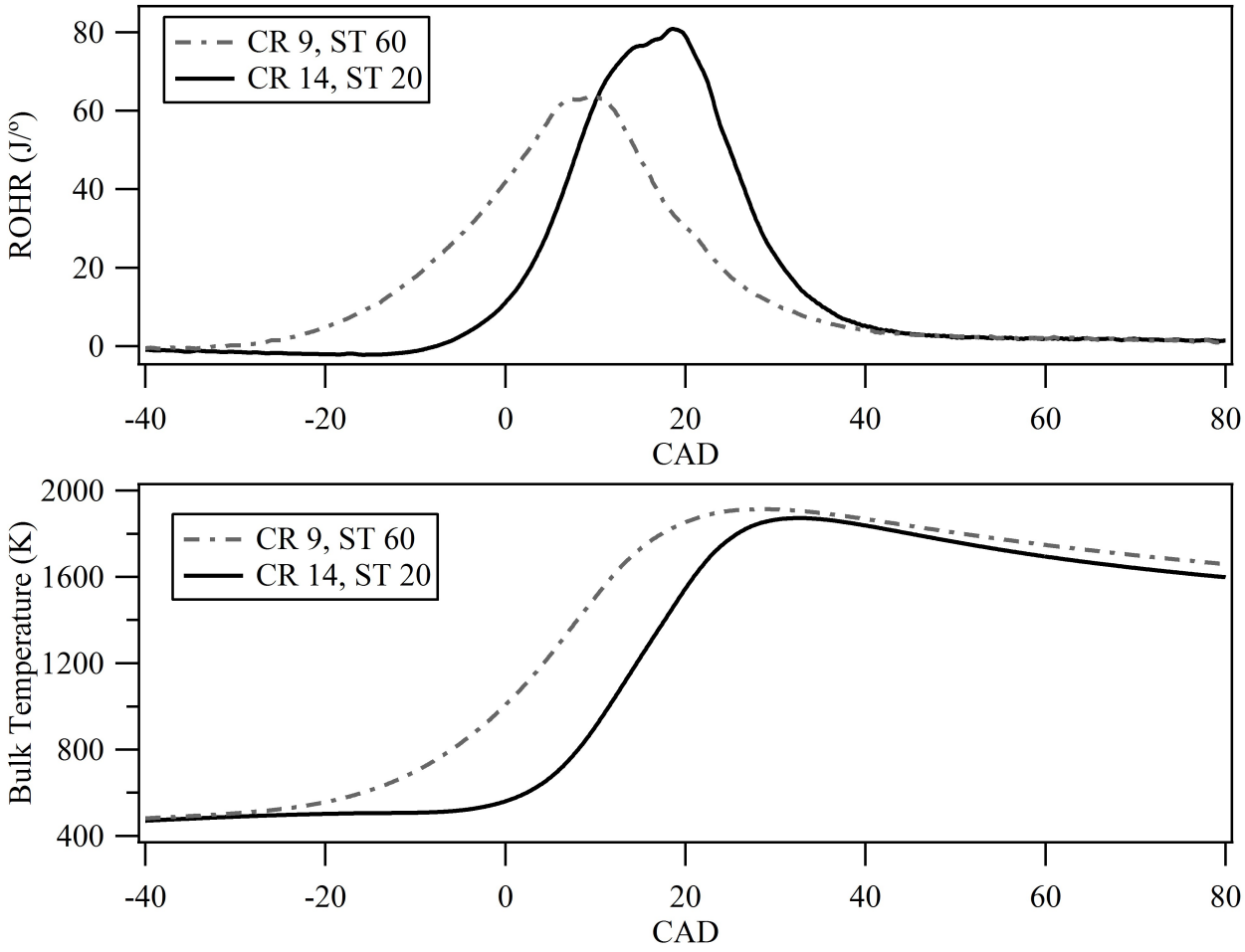

Figure 10.7: The average ROHR versus CAD and the average bulk temperature versus CAD of dry EGR with 25.8% O_2 for CR 9 and 14.

distinct curves seen at high compression ratio do not exist at low CRs, but rather slowly form as the CR in increased. This indicates that due to the higher bulk temperature, the small, controlled autoignition events identified at higher CRs are much less common at low CRs, and the result is limitations similar to heptane-in-air, as shown in Fig. 10.4(a). Higher peak ROHR, and also the small, controlled autoignition events noted at CR 14, start to develop around CR 10, and continue to become more pronounced as the CR in increased.

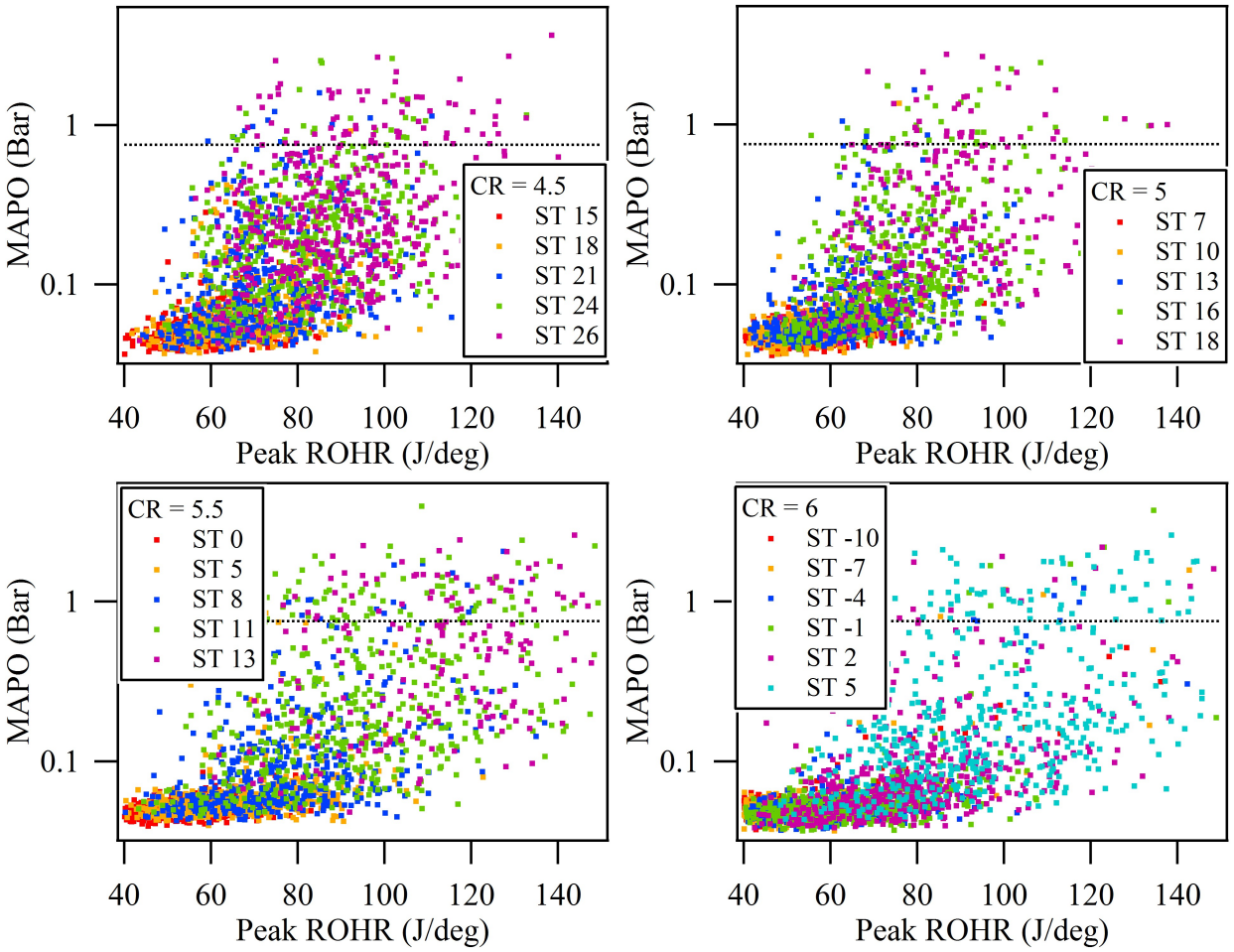

Figure 10.8: MAPO versus peak ROHR for air across tested CRs.

O_2 Concentration Effects

Comparing the maximum CRs across different O_2 concentrations results in a similar trend to that shown in Fig. 10.9. In Fig. 10.10 the maximum CRs tested at each dry EGR test point are shown, with the high O_2 cases producing curves similar to air. Based on the trends it can be concluded that the ability to avoid knock and sustain small, controlled autoignition events which correspond to good IMEP and low knock increases with increasing CRs and lower temperatures. Wet EGR is limited in its ability to operate in this ideal region of good IMEP and low knock due to its elevated intake temperature which increase the bulk temperature throughout the cycle.

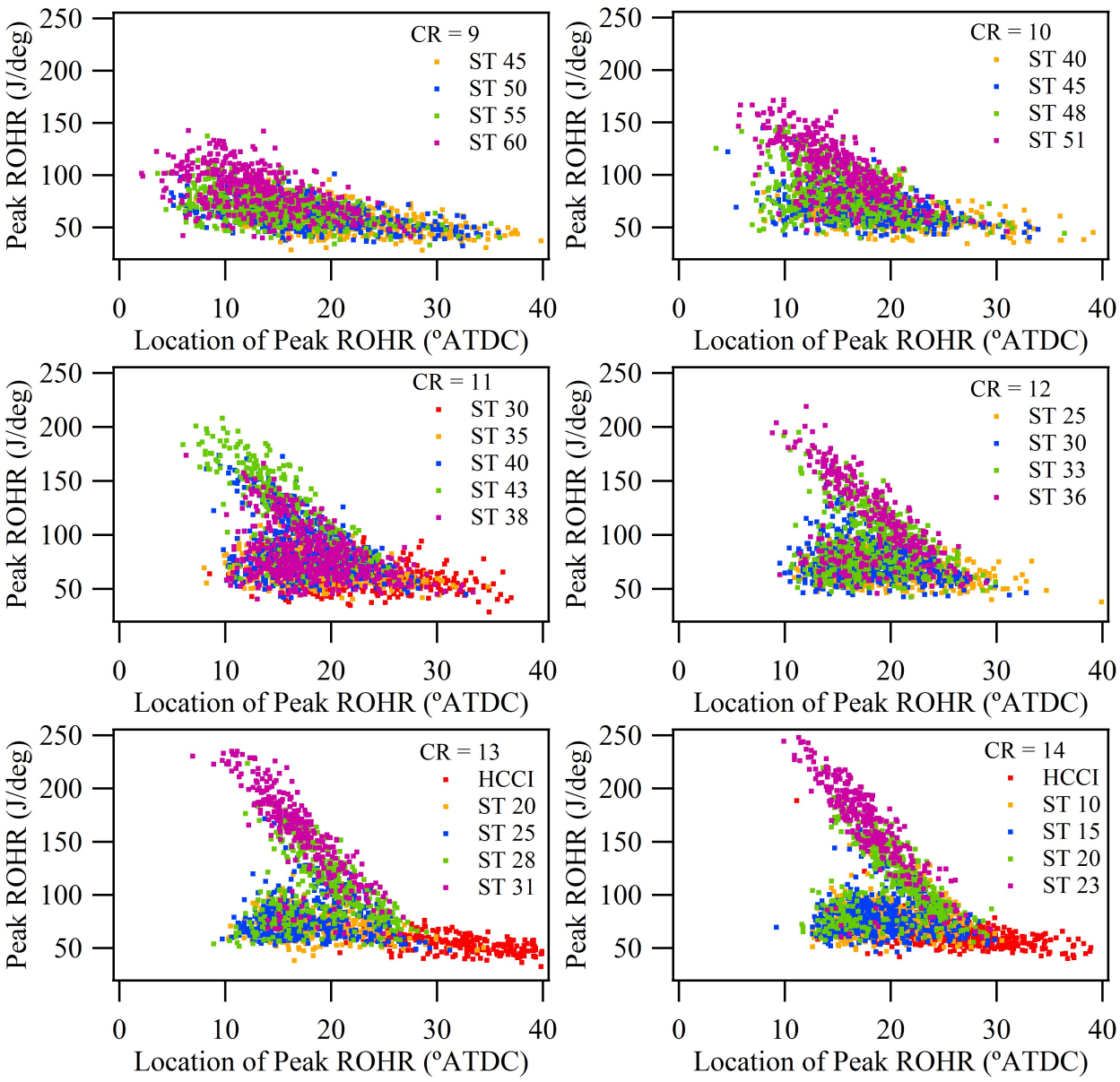

Figure 10.9: The peak ROHR versus location of the peak of dry EGR with 25.8% O_2 for CR 9 through 14.

10.2 Average Cycle Trends

Comparing cycle-by-cycle data points it was concluded that minor autoignition plays a major role in dry EGR combustion, with increasing influence at lower O_2 concentrations and higher CRs. Th effects are significant enough that they are easily identified in the average cycle

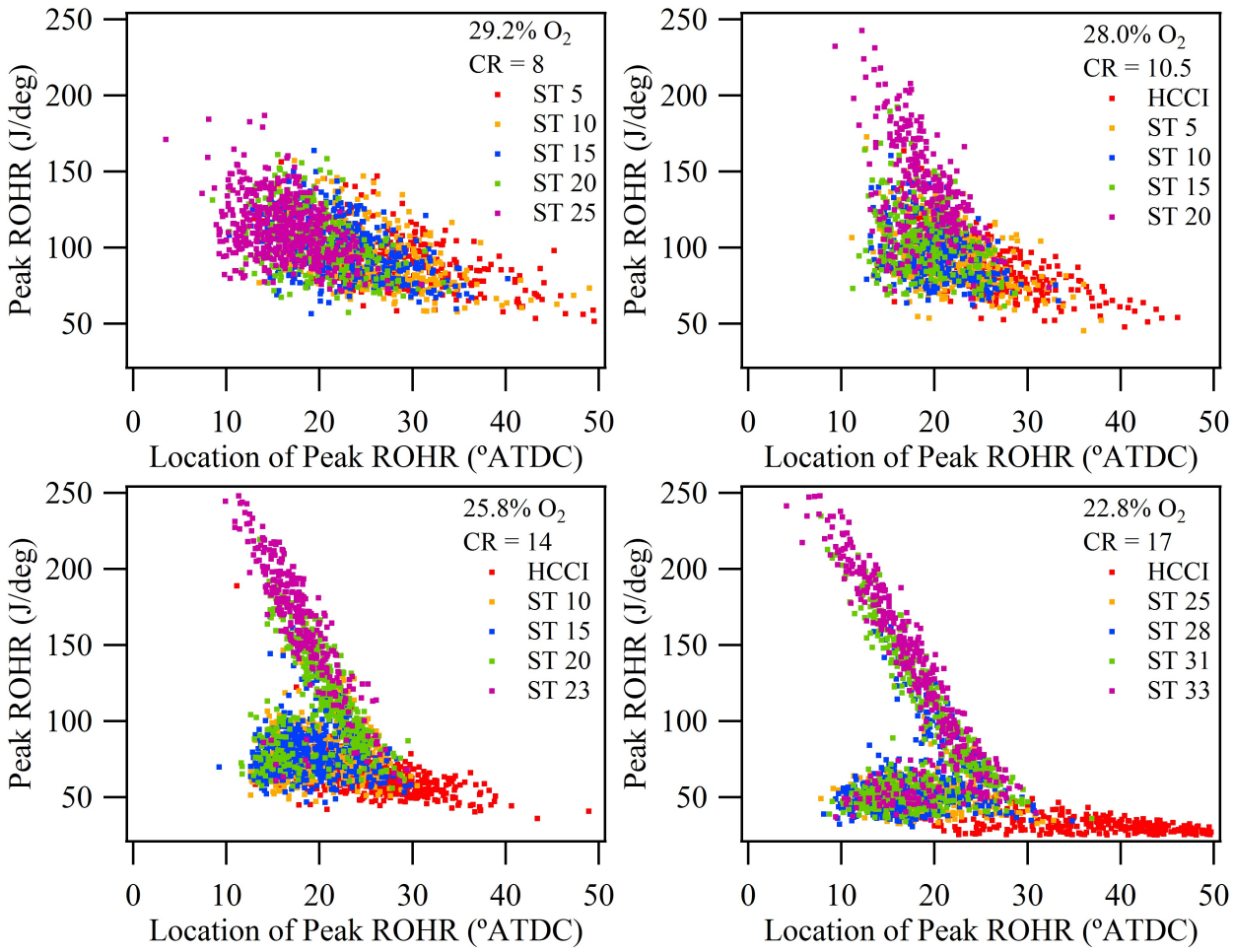

Figure 10.10: The peak ROHR versus location of the peak of dry EGR at maximum tested CR points for each of the 4 tested O_2 concentrations.

curves as well.

Figure 10.11 displays the average normalized ROHR curves (normalized by the net HR of each case) for each CR for air, dry EGR with 25.8% O_2, and wet EGR with 23.6% O_2. It is immediately apparent that wet and dry EGR display very different trends with increasing CR than air does.

As the compression ratio increases for the air cases the ROHR curves broaden, lower, and shift to later in the cycle. This is in contrast with the wet and dry EGR cases which show increasing peak height and narrower distribution as the CR is increased. This increased peak height and narrower profile more closely matches an ideal cycle, in which the fuel energy is released instantly, and is the reason for the increased thermal efficiency and power seen as the CR of EGR cases is increased. Air does not follow this trend, but rather the peak height

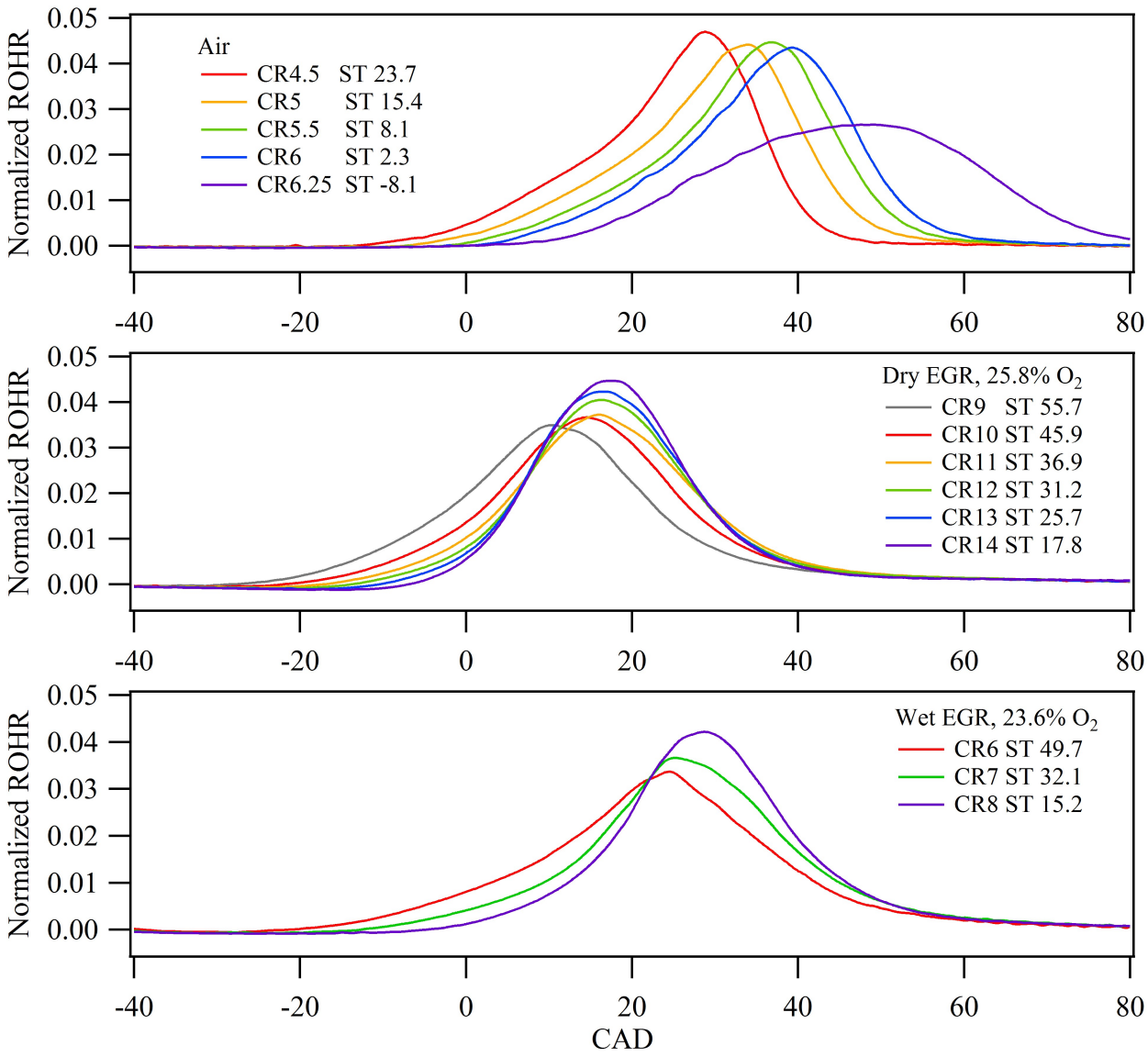

Figure 10.11: Normalized average ROHR curves versus CAD for all CRs tested with air, dry EGR with 25.8% O_2, and wet EGR with 23.6% O_2.

decreases and the profile becomes wider resulting in no increased in thermal efficiency and power as the CR is increased.

The reason for the unexpected shift in trends between the air case and the EGR cases could be due to increased turbulent flame speed, but it seems unlikely since any increase in turbulence should also be present in the air cases and result in similar trends. More likely is that auto-ignition events, as identified in the previous section, become more prevalent in the

EGR cases as the CR is increased, leading to a more rapid overall heat release. This same effect is not present in the air cases, as auto ignition events are much more likely to result in knock, and therefore must be avoided. This can be noted Fig. 10.6 and 10.8 above which plot MAPO vs. peak ROHR. The air cases show a much larger spread in MAPO values than do the EGR cases, indicating that it is not feasible to operate at a point with any significant level of autoignition without also producing a significant number of knocking cycles. In contrast, looking at the dry EGR cases you can see that there exists peak ROHR values which clearly correspond to some autoignition (identified by the elevated MAPO values) for virtually every cycle, but rarely, if ever, is the knock limit exceeded. Not surprisingly, the points which fall in these regions of the curve have spark timings very close to the threshold spark timings.

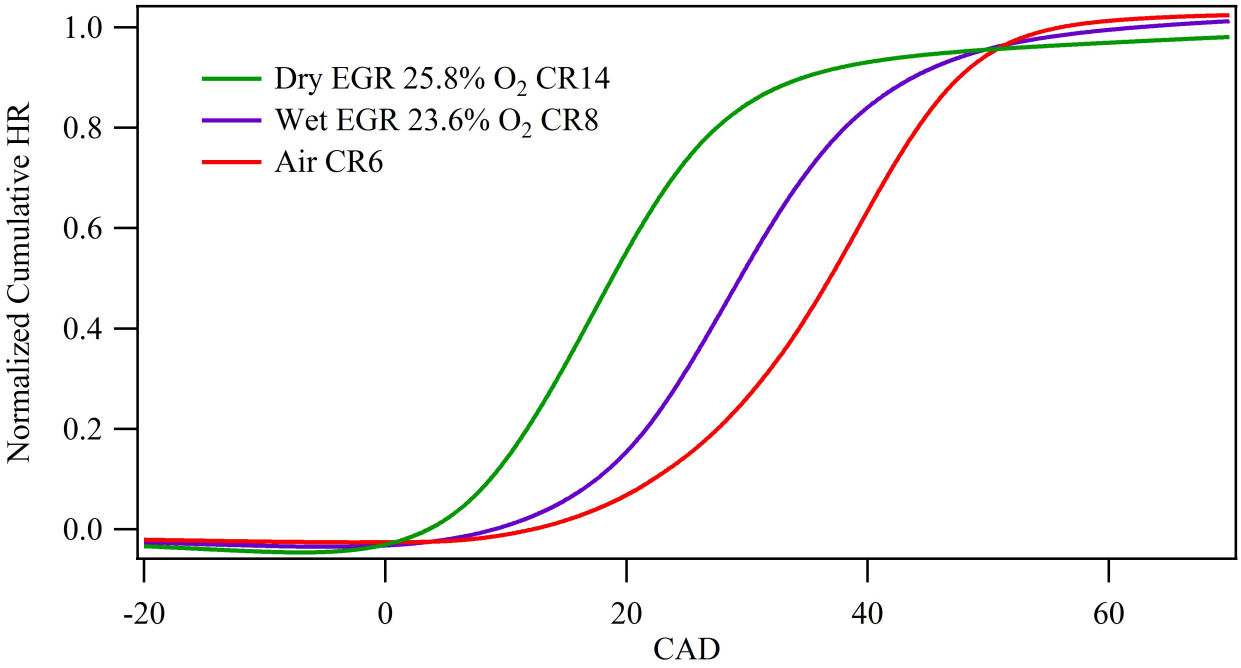

Figure 10.12: Normalized Cumulative HR curves versus CAD compared across working fluids.

Figure 10.12 shows the normalized cumulative heat release (HR) versus the CAD across the three working fluids tested. All three fluids produce curves with similar slopes and profiles, with the primary difference being the location of the curves relative to CAD. The similarity of slopes despite the greatly reduced flame speeds at these low O_2 concentrations (as determined in chapter 5) confirms that autoignition events are accelerating the average HR for the EGR cases. In addition to equaling the curvature of air, dry EGR is able to produce its heat release much closer to TDC than either wet EGR or air, which is desired for maximum power extraction.

Compression ratio effects are illustrated in Fig. 10.13 for air and dry EGR with 25.8% O_2. As the CR is increased with air the curve maintains its profile and shifts later in the cycle. Dry EGR shows a substantially different trend, as the increasing CR first shifts the trend to the right at low CRs, but then the end of heat release timing and profiles are virtually identical across all high CRs. Even after this convergence of the end of combustion is reached, increasing the CR continues to shift the start of combustion later in the cycle, producing a steeper cumulative HR curve, which is desired. The changing of the cumulative HR profiles with dry EGR, while air shows the same profile but a shift in location, helps to further explain why thermal efficiency increases as the CR of EGR is increased, but remains constant with respect to CR for air.

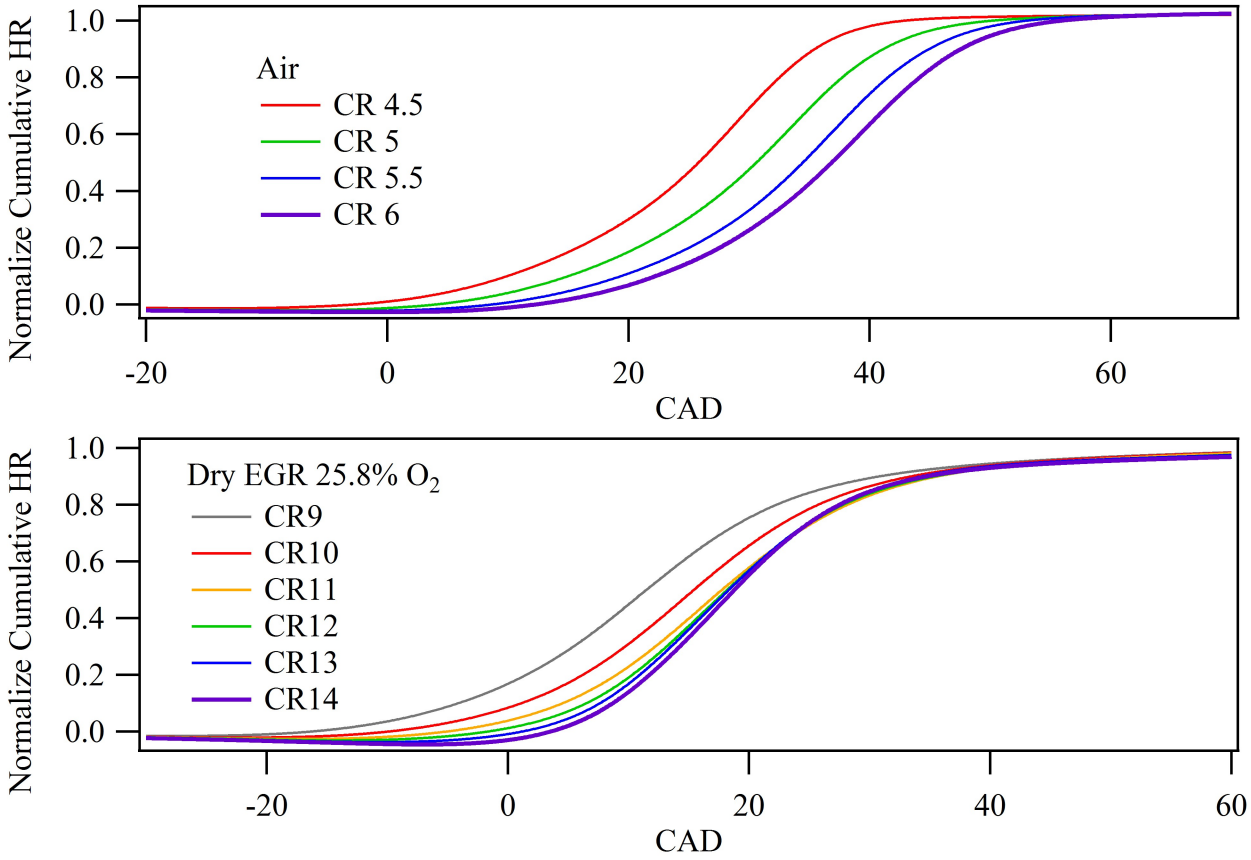

Figure 10.13: Normalized Cumulative HR curves versus CAD compared across CRs for Air and dry EGR with 25.8% O_2.

The trends in ROHR correspond to similar discrepancies in the trends of the in-cylinder temperature profiles, as shown in Fig. 10.14. For air, as the CR is increased the peak temperature occurs later in the cycle, corresponding to a decreasing peak temperature. For

wet and dry EGR the peak temperature shifts similarly for the first one to two increases in CR, but then the location of the peaks converge for all remaining CRs.

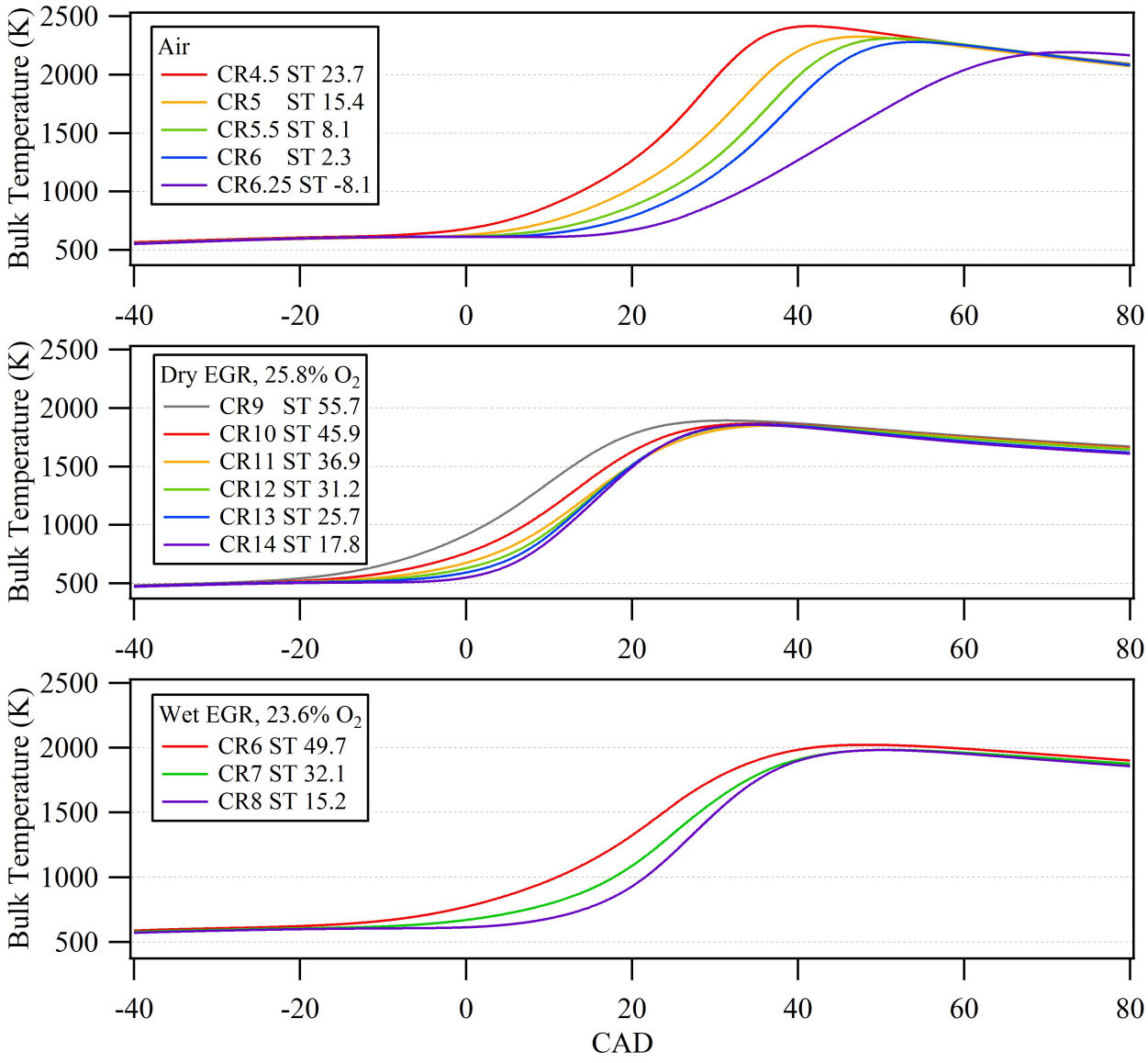

Figure 10.14: Average bulk temperature curves versus CAD for all CRs tested with air, dry EGR with 25.8% O_2, and wet EGR with 23.6% O_2.

The convergence of the end of combustion portion of the cumulative HR curves at high CRs has additional implications. Figure 10.15 displays the normalized cumulative HR curves for the peak CRs of all 4 dry EGR O_2 concentrations tested. The two highest O_2 concentration cases produce nearly identical curves, with the 29.2% O_2 case being shifted to a

slightly later CAD, similar to the effects seen in air as the CR was increased. The behavior is expected at the high O_2 concentrations, where laminar flame speeds and temperatures approach those of air. However, as the O_2 concentration decreases to 25.8%, and then to 22.8%, there is a developing trend towards a more rounded end of combustion profile. This is not a desired effect, as is lengths the overall HR duration. Additionally, based on the convergence of the end of combustion profiles noted for dry EGR in Fig. 10.13, this is not an effect which can be counter-acted by increasing the CR.

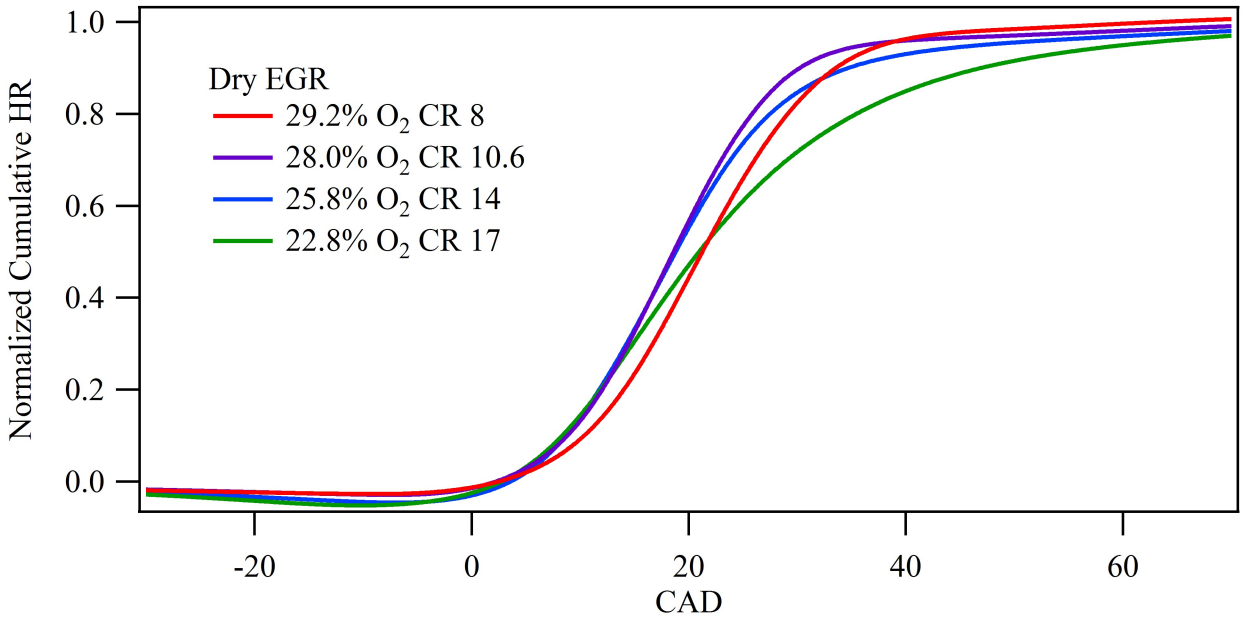

Figure 10.15: Normalized Cumulative HR curves versus CAD of dry EGR at the maximum CR tested at each O_2 concentration.

The rounding of the end of combustion profile as the O_2 concentration is increased also helps to explain 2 additional phenomenon which were noted in the heptanes performance section: (1) the decreasing combustion efficiency noted as the O_2 concentration was decreased, and (2) the effect of O_2 concentration on thermal efficiency at equivalent CRs. The end of combustion is largely responsible for the combustion efficiency in an engine. If the flame propagation is strong the cumulative HR will flatten off quickly and little fuel with be left unconsumed. Fuel in crevices are the exception to this rule, as crevices produce some unburned hydrocarbons regardless of flame propagation strength. Observing Fig. 10.15, the increased rounding of the end of combustion profile indicates that the flame propagation becomes very weak as the O_2 concentration is reduced. This weak combustion can result in pockets of fuel remaining uncombusted, as well as larger unburned regions near the walls and cylinder. It is therefore understandable that the combustion efficeincy dropped so strongly as the O_2 concentration was decreased, as seen in Fig. 9.8.

Examining the thermal efficiency of dry EGR, shown in Fig. 9.5, it can be seen that as the O_2 concentration is reduced from 29.2% to 28.0% the thermal efficiency at equivalent CRs increases. Conversely, the overlapping CR points between 28.0% O_2 and 25.8% O_2 show almost identical thermal efficiency, while the decrease to 22.8% O_2 from 25.8% O_2 produces a significant decrease in thermal efficiency at equivalent CRs. These effects can be attributed to the end of combustion cumulative HR profiles, compared in Fig. 10.16 (a), (b), and (c).

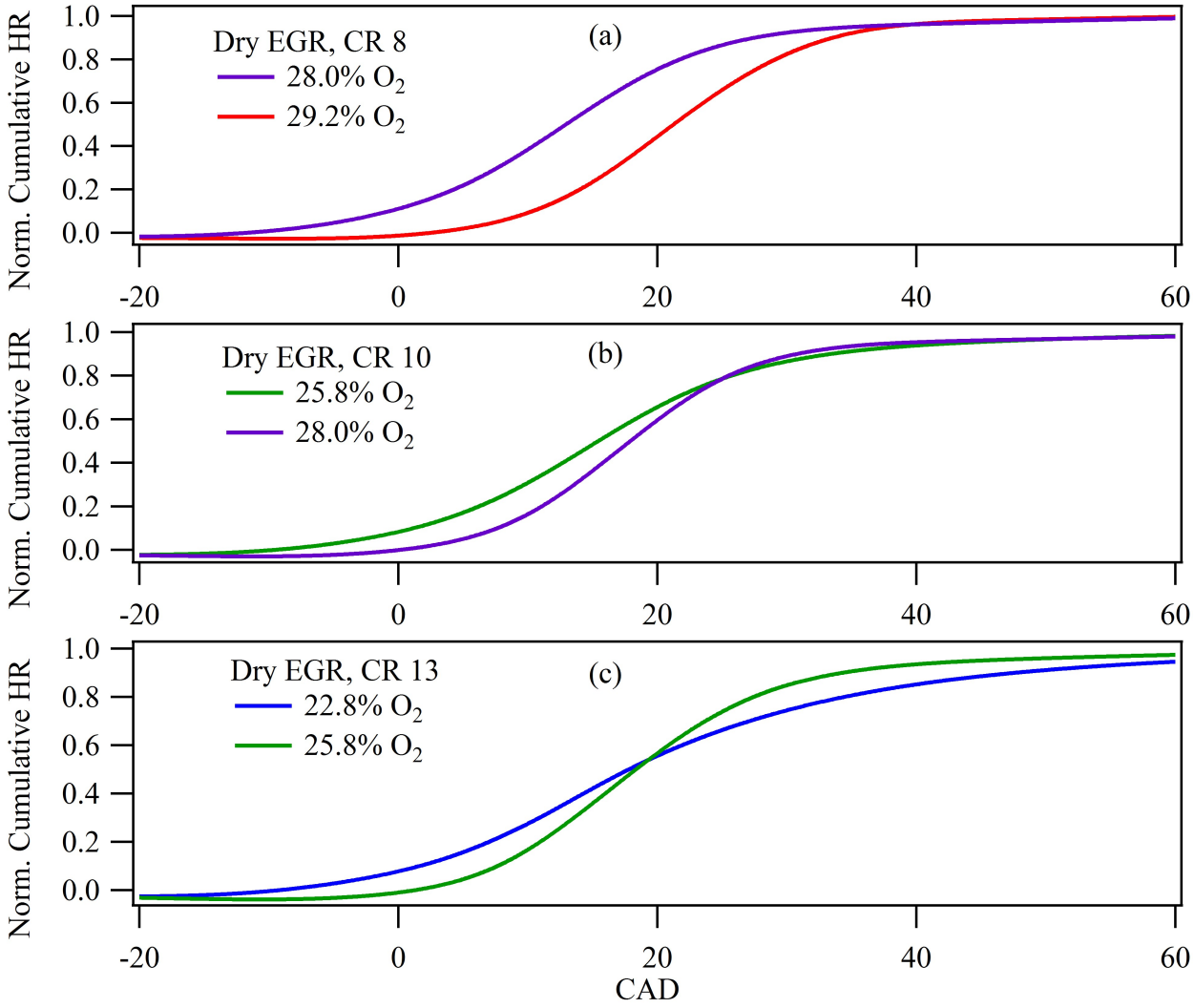

Figure 10.16: Normalized Cumulative HR curves versus CAD comparing equal CRs at different O_2 concentrations.

At the highest O_2 concentrations, where the profiles are almost identical, the decrease in O_2 results in a very similar normalized cumulative HR curve profile shifted closer to TDC. Thus, power generation is similar, but the heat losses are reduced due to the lower

temperatures which the reduced O_2 and fuel fractions produce, resulting in higher thermal efficiency. As the O_2 concentration is decreased from 28.0% to 25.8%, shown in Fig. 10.16 (b) the rounding of the end of combustion profile results in a clear difference in profile slopes. However, the difference in the slope is small enough that the losses are offset by the reduced heat losses, and the result is nearly identical thermal efficiency. Finally, reducing the O_2 concentration from 25.8% to 22.8%, shown in if Fig. 10.16 (c), produces such significant rounding of the end of combustion that it far outweighs the reduced heat loss, resulting in a significant decrease in thermal efficiency.

When dry EGR was tested with 22.8% O_2 it was found that it could operate at CR 17 easily, indicating that further increases in CR could be sustained before knocking intensity could no longer be controlled with spark-timing. However, based on the convergence of the end of combustion profiles shown in Fig. 10.13, the system may be limited. Indeed, Fig. 10.17 illustrates that increasing the CR only serves to modify the start and middle of combustion profile, and the end of the profile is largely fixed. Increasing the CR further could continue to improve the start and middle of combustion profile, but the ability to produce low CoV IMEP and high combustion efficiency will be limited. This provides strong evidence that continuing to decrease the O_2 concentration will ultimately lead to the reduction of all major engine performance parameters regardless of the CR.

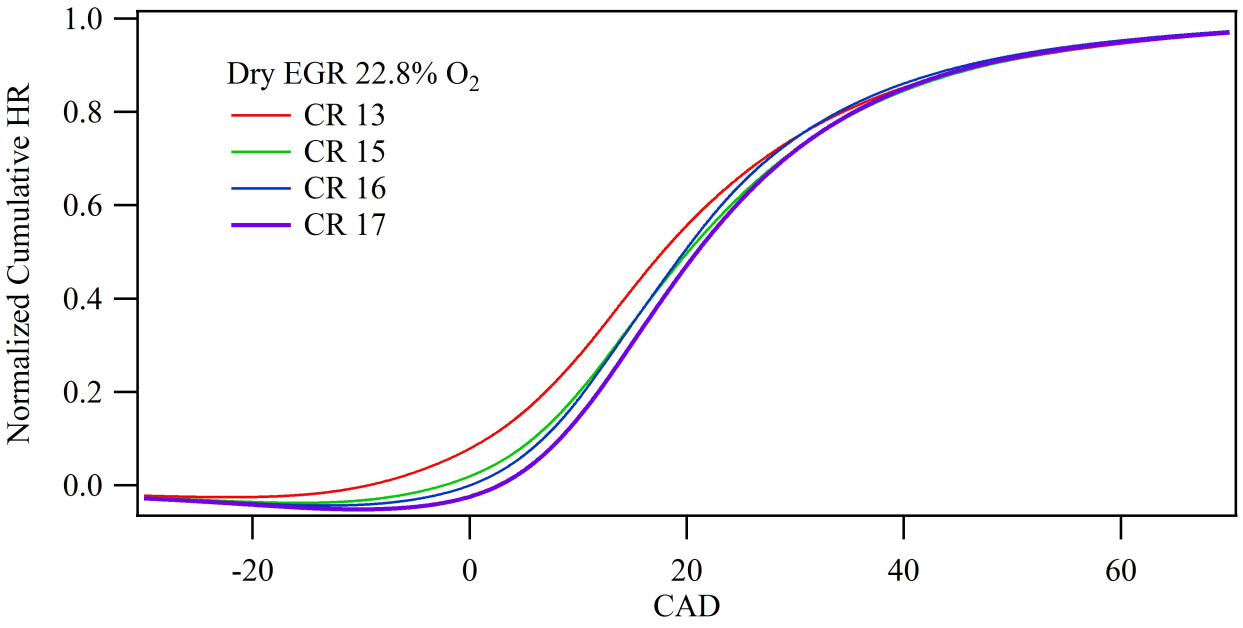

Figure 10.17: Normalized Cumulative HR curves versus CAD of dry EGR with 22.8% O_2 at tested CRs.

10.3 Conclusions

Detailed point-by-point and cycle average analysis have been carried out. A clear difference in the behavior of dry EGR runs at high CRs and low O_2 concentrations and air runs has been identified. The source of the discrepancy has been identified as minor autoignition events in the dry EGR which substantially decrease the burn duration without producing significant knock. The autoignition events are not present at high O_2 concentrations, or at low CRs, where dry EGR combustion behaves very similarly to air. The development of a significant number of cycle with minor autoignition events is identified as the reason the thermal efficiency of dry EGR increases as the CR is increased while air maintains constant thermal efficiency across CRs, as well as the reason for the decreasing CoV IMEP with increasing CR. It was determined that these autoignition events only significantly influence the start and middle of the combustion process, and not the end of combustion. The inability of CR and autoignition events to alter the end of combustion HR profile creates a limit to how far the O_2 can be reduced while continuing to improve thermal efficiency and maintain low CoV IMEP.

Wet EGR produces similar trends as dry EGR, but on a significantly reduced magnitude, partially do to the highly restricted CR range over which it was able to operate. Ultimately, despite the chemical and thermal advantages of water compared to CO_2 in regards to laminar flame speeds, wet EGR is not a reasonable choice when operating in an IC engine due to its elevated intake temperature and higher wall-heat losses.

Chapter 11

Octane Rating Effects

The fuel used for these experiments was advertised as '96% nHeptane', but testing in a GC indicated that it was less than 50% n-Heptane, and was primarily other heptanes. Testing against actual nHeptane it was found that the fuel used, referred to as 'heptanes' had a higher knock resistance than the n-Heptane fuel. A comparison was then conducted between the two fuels at equivalent intake conditions and compression ratios in air (CR = 5) and dry EGR (CR = 16). Spark timings corresponding to the knock limit are listed in table 11.1.

Table 11.1: Major engine performance parameters when running on n-Heptane versus Heptanes. Air cases have a CR of 5, Dry EGR cases have a CR of 16 and 22.8% O_2 concentration.

	Air	Air	dry	dry
Fuel	heptanes	n-heptane	heptanes	n-heptane
ST (dBTDC)	14.70	8.9	34.7	15.20
IMEP	6.38	6.2	7.77	8.11
Thermal Efficiency	23.1%	22.7%	25.2%	26.4%
CoV IMEP	2.96%	3.55%	5.85%	3.26%
Combustion Efficiency	97.7%	98.0%	90.6%	88.9%

The difference in knock resistance can be identified based on the later spark timings required for n-Heptane in both air and dry EGR cases. In addition, heptanes produced higher IMEP and thermal efficiency than the n-Heptane when operating in air, which is expected for a knock-limited condition. However, the trend is reversed for the dry EGR cases, where the n-Heptane produced significantly higher IMEP and thermal efficiency than the heptanes did. This reversal of IMEP and thermal efficiency trends confirms that controlled auto-ignition of end gases, and not an increased in turbulent flame speed, is the significant reason for the increased performance of EGR cases relative to air cases. Note that the 26.4% thermal efficiency produced when operating on n-heptane is the highest produced in any of the tests with heptanes, even surpassing dry EGR operated at CR 17. The reason for the

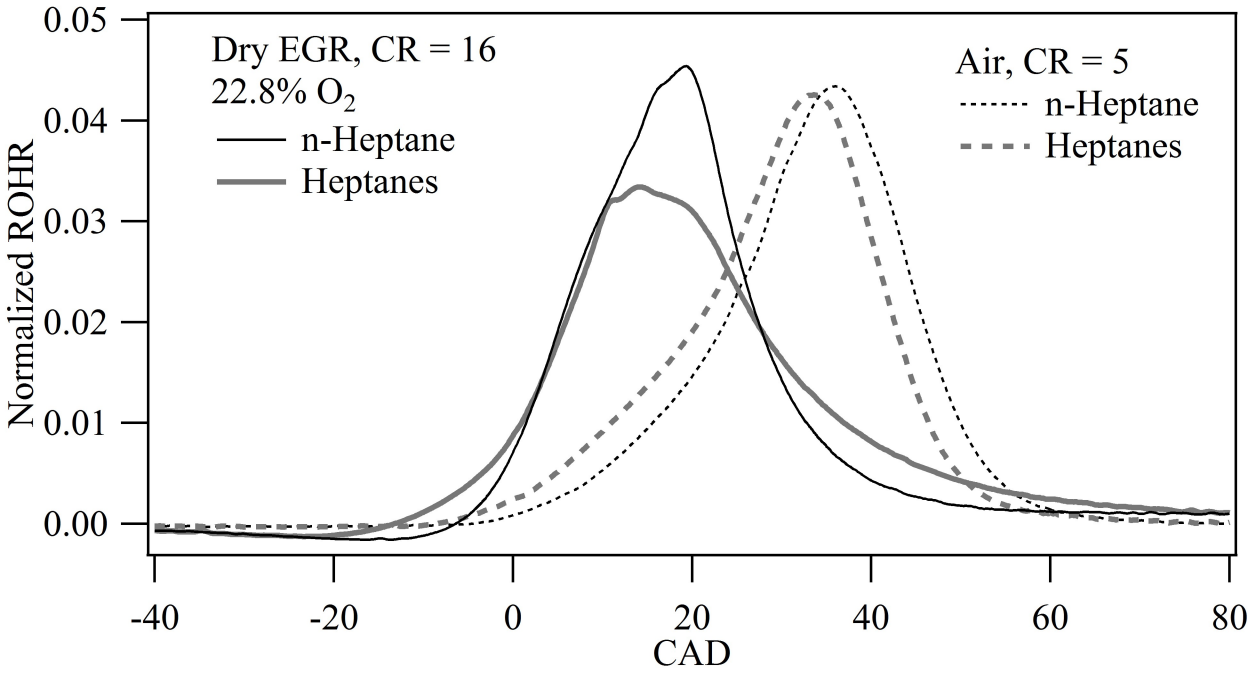

Figure 11.1: Normalized average ROHR curves versus CAD comparing heptanes and n-heptane fuels in dry EGR and air.

advantage is quite apparent in Fig. 11.1, which shows the normalized ROHR curves for the knock limit spark timings for all 4 cases.

Observing the air cases, where we do not expect to sustain autoignition while operating below the knock limit, the normalized ROHR curves are nearly identical in shape and magnitude. The only significant difference is that the n-heptane curve is shifted later in the cycle, which is expected since it has a lower knock resistance which must be overcome by delaying the combustion process. This delay in the combustion process produces the slightly higher CoV IMEP seen with n-heptane and air, but has almost no effect on combustion efficiency. In contrast, the normalized ROHR curves for Dry EGR look very dissimilar with n-heptane producing a much higher peak ROHR and a narrower overall profile; both traits which have been identified as desirable. As confirmation of the improved HR profile, the CoV IMEP is significantly decreased for n-heptane. The combustion efficiency drops very slightly, as would be expected from a larger autoignition event.

Figure 11.2 depicts the same normalized ROHR curves for dry EGR as shown in Fig. 11.1, but with the addition of the corresponding curve from dry EGR with 25.8% O_2 at CR 13. It is immediately noticed that the 25.8% O_2 case has a ROHR far more similar to that of the n-heptane curve. What can be concluded is that while lower O_2 concentrations produce increased efficiency do to reduced in-cylinder temperatures, at some O_2 concentration the temperatures become so low that the consistency of the autoignition events starts to decrease.

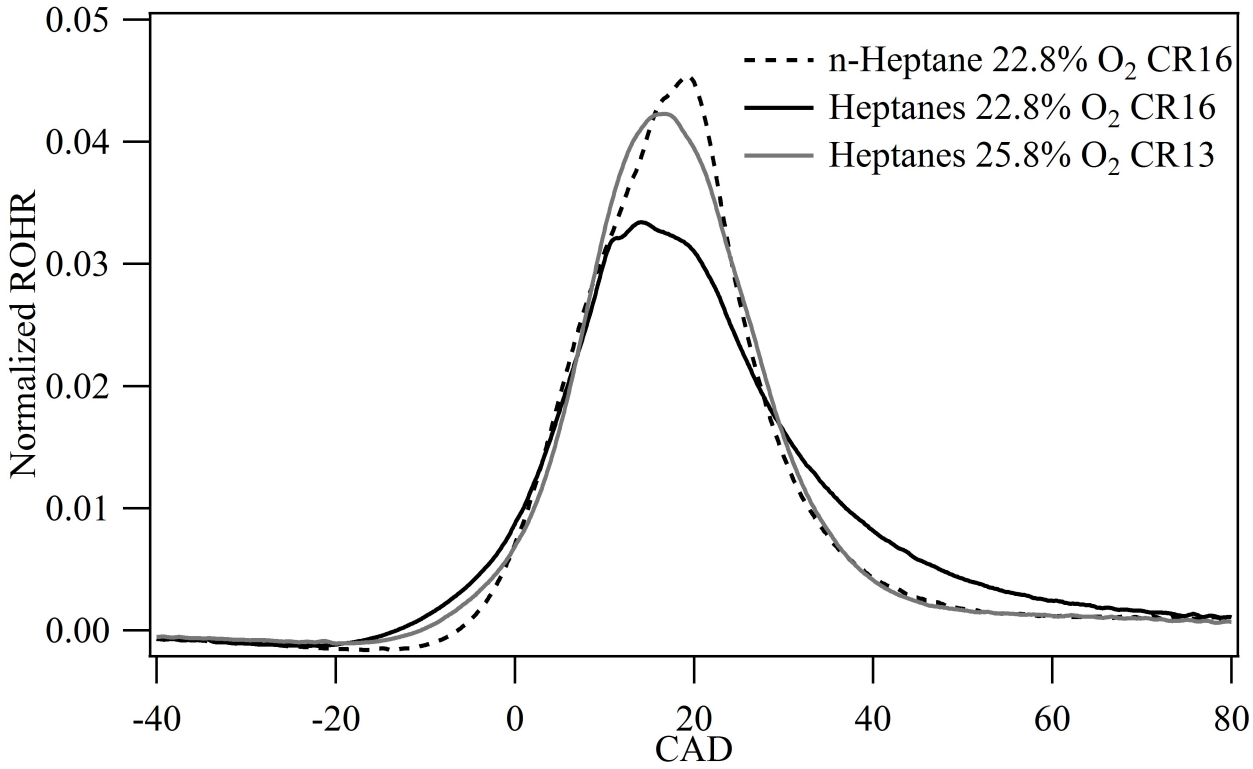

Figure 11.2: Normalized cumulative HR versus CAD comparing heptanes and n-heptane in dry EGR.

Switching to a lower octane fuel, in this case n-heptane, reduces the temperature requirement of autoignition, and thus allows the engine to perform better at the same, reduced O_2 concentration. The reduced temperature which limits the lower O_2 concentration could partially be overcome by increasing the CR, but since the engine was limited to a CR of 17 the process could not be fully explored, and based on the normalized cumulative HR curves shown in the previous section increasing CR is limited to modifying only the start and middle of the combustion process, not the end.

Figure 11.3 shows the normalized cumulative HR for the two different fuels at CR 16. It is clear that the n-heptane curve is much less rounded in the end of combustion region than the heptanes curve, leading to improved thermal efficiency and combustion efficiency. Based on the profile of the n-heptane curve it is likely an even higher thermal efficiency could be achieved by further reducing the O_2 concentration. Therefore, it can be concluded that the ideal operating O_2 concentration decreases with the octane rating.

The bulk temperature versus CAD is shown for the two different fuels in Fig. 11.4. The peak temperature of the n-heptane is actually higher than the heptanes, which is expected based on having the same quantity of fuel energy and a faster combustion process.

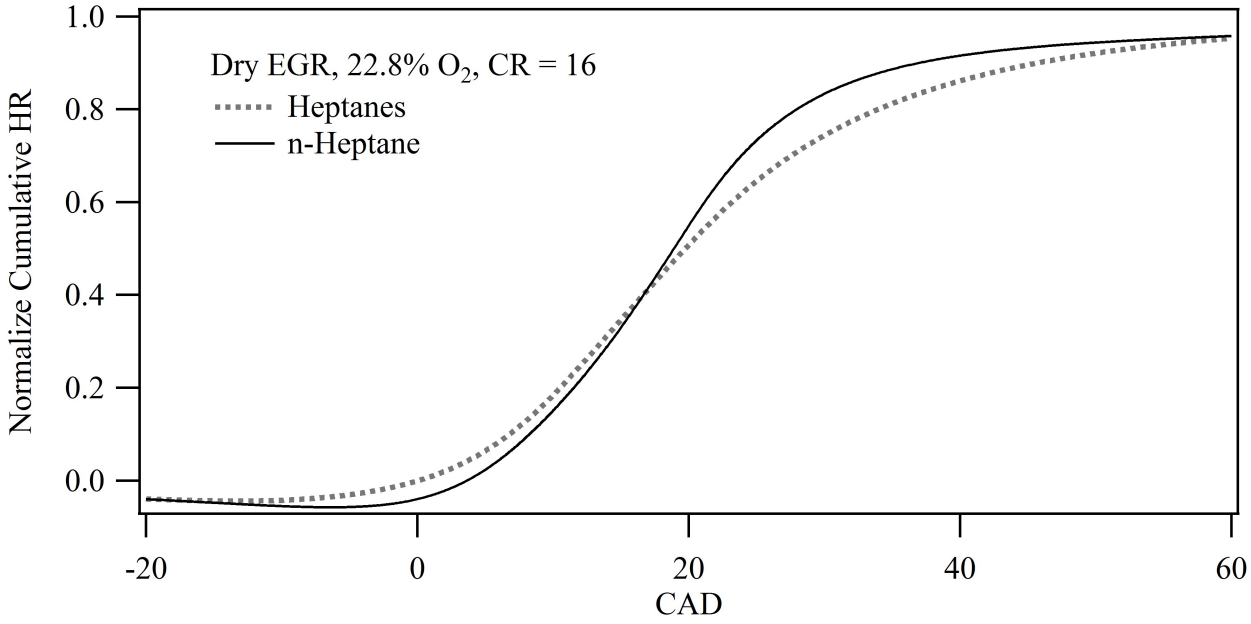

Figure 11.3: Normalized cumulative HR versus CAD comparing heptanes and n-heptane in dry EGR.

In addition, the higher temperature further helps the lower octane fuel achieve consistent autoignition, which is a critical competent of low O_2 concentration oxycombustion.

11.1 Conclusions

A higher purity n-heptane fuel with a lower octane rating was operated under equivalent intake conditions and CR as the heptanes used for the studies of chapters 9 and 10. It was found that while the lower octane fuel produced lower thermal efficiency in air, it was able to produce higher thermal efficiency and lower CoV IMEP in dry EGR with 22.8% O_2. In dry EGR n-heptane produced a thermal efficiency of over 26.4% coupled with a CoV IMEP of 3.25%, compared to heptanes which produce a thermal efficiency of 25.2% and a CoV IMEP of 5.85%. The result of increased thermal efficiency and decreased CoV IMEP strongly support the conclusion that autoignition events are the driving force behind low octane rating combustion in dry EGR.

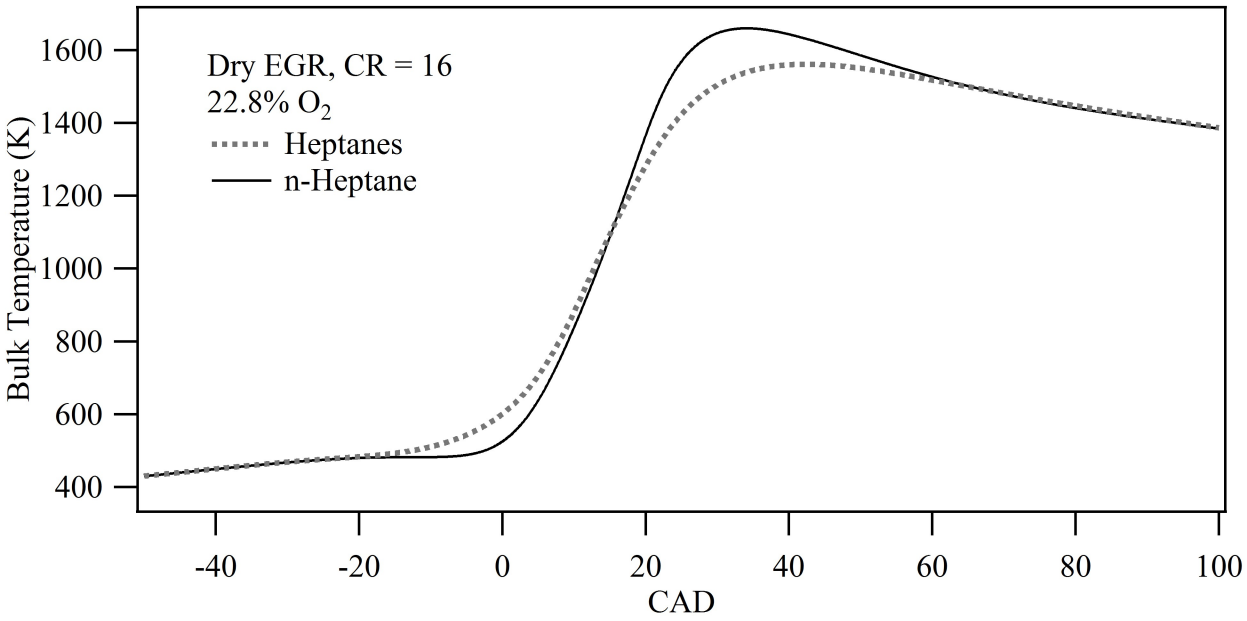

Figure 11.4: Bulk temperature versus CAD comparing heptanes and n-heptane in dry EGR.

Chapter 12

Concluding Remarks

A single cylinder, variable compression ratio (CR) CFR engine has been modified with a large, steady-state EGR system for the testing of spark-ignited oxycombustion power generation. The setup represents a pioneering effort to experimentally quantify and understand EGR working fluids in a full-scale engine. Performance has been extensively studied over a range of CRs and spark-timings when operating with methane, which has very good knock resistance, and heptanes, which has very poor knock resistance. It was found that dry EGR out-performed wet EGR, producing higher thermal efficiency in both tests as a result of high wall heat transfer and high intake temperatures when running with wet EGR. Most significantly, it was found that dry EGR produced higher thermal efficiency when operating with heptanes than when operating with methane. The result is possible due to the excellent knock resistance of the CO_2 working fluid, which allows regularly occurring minor autoigntion events when operating with heptanes without producing significant knock. Wet EGR produced similar autoignition events, but the elevated intake temperatures required to prevent condensation of the EGR water vapor resulted in engine operating being limited to much lower CRs and thermal efficiencies due to knock limitations.

Methane Results

Methane oxycombustion has been studied using both wet and dry EGR and compared to methane-in-are combustion in the same engine. Predicted laminar flame speeds dropped by a factor of 2 in wet EGR while dry EGR showed a decrease by more than a factor of 4 relative to methane-in-air. The significantly higher laminar flame speeds in wet EGR were found to be the product of water displacing CO_2 from a chemical standpoint, since CO_2 has significant negative chemical iterations where as water is relatively inter, and a thermal standpoint, since water has significantly higher thermal diffusivity than CO_2.

The advantage of the flame speeds produced significantly superior performance in wet EGR relative to dry EGR when intake pressure and temperature, oxygen concentration, CR and spark-timing were held constant. However, when dry EGR was operated at room temperature (as opposed to the 100°C intake temperature of wet EGR), and CR and spark-

timing were adjusted to maximize thermal efficiency, dry EGR produced superior results due to the high wall heat losses of wet EGR. Various oxygen concentrations were tested for each working fluid which spanned the concentration which corresponded to maximum thermal efficiency. It was found that the oxygen concentration for each fluid which corresponded to the maximum thermal efficiency produced normalized cumulative HR curves with nearly identical profiles to the peak methane-in-air thermal efficiency point.

Due to the limited range of CRs (upper limit of 17) which can be tested on the CFR engine it was not possible to produce knock in any of the methane tests, resulting in any advantages due to the knock resistance of the tri-atomic EGR working fluids not being realized in these studies. As a result of being restricted to operating at the same CR, despite producing nearly identical normalized HR curves, the peak thermal efficiency of wet and dry EGR were far below that of methane-in-air. The decreased thermal efficiency was largely due to the larger specific heat capacity of the tri-atomic working fluid, which results in greatly increased thermal losses to the exhaust. The experimental results where is consistent with the predicted theoretical maximum thermal efficiency, which were greatly reduced due to the much lower ratio of specific heat of EGR.

NO_x production was studied, and found to be negatively correlated with power, thermal efficiency, and CoV IMEP. Under normal combustion with 2-4% N_2 it was possible to reduce NO_x levels to near regulation levels by using low oxygen concentrations but this was at the cost of sacrificing performance. A linear correlation between N_2 concentrations and NO_x production was found. Based on the observed trends, to operate below regulation NO_x levels with the amount of N_2 used in these tests (roughly 2% for wet EGR and 3-4% for dry EGR) would require taking unacceptable reductions in thermal efficiency and CoV IMEP.

Heptane Results

Heptane fueled oxycombustion was studied to quantify any superior knock-resistance of EGR working fluids relative to air. All cases were knock limited, with spark-timing used to adjust the intensity of the knock. As the CR was increased EGR cases ultimately reach a point of HCCI-type autoignition independent of spark, which limited the upper CRs which could be tested. Dry EGR was able to operate at very high CRs, and produced a peak thermal efficiency of over 25.5%, surpassing the peak thermal efficiency of air, which managed 23.4%. Wet EGR performed the worst of all the fluids, managing to produce only 21.3% thermal efficiency which was additionally coupled with high CoV IMEP. Wet EGR was limited to less than 20% thermal efficiency when a CoV IMEP of less than 5% was required.

Theoretical thermal efficiency largely correlates with the experimental findings based on the ratio of specific heats for each case and the CRs which were able to be run. One point of discrepancy between the theoretical thermal efficiency trends and experimental results was that increasing CR did not improve the experimental thermal efficiency of air. In addition, theoretical thermal efficiency limits predict that for a given working fluid and CR the thermal efficiency should be constant regardless of oxygen concentration. This correlation is not present in the experimental results.

Detailed point-by-point and cycle average analysis were used to identify the autoignition events. A clear difference in the behavior of dry EGR runs at high CRs and low oxygen concentrations and air runs was been identified, with the source of the discrepancy being identified as minor autoignition events in the dry EGR which substantially decrease the burn duration without producing significant knock. The autoignition events are not present at high oxygen concentrations, or at low CRs, where flame speeds and temperatures are higher and dry EGR combustion behaves very similarly to air. The development of a significant number of cycle with minor autoignition events is identified as the reason the thermal efficiency of dry EGR increases as the CR is increased while air maintains constant thermal efficiency across CRs, as well as the reason for the decreasing CoV IMEP with increasing CR. It was determined that these autoignition events only significantly influence the start and middle of the combustion process, and not the end of combustion. The inability of CR and autoignition events to alter the end of combustion HR profile creates a limit to how far the oxygen can be reduced while continuing to improve thermal efficiency and maintain low CoV IMEP.

A higher purity n-heptane fuel with a lower octane rating was operated under equivalent intake conditions and CR as the heptanes used for the main studies to help isolate the autoignition events. It was found that while the lower octane fuel produced lower thermal efficiency in air, it was able to produce higher thermal efficiency and lower CoV IMEP in dry EGR with 22.8% O_2. In dry EGR n-heptane produced a thermal efficiency of over 26.4% coupled with a CoV IMEP of 3.25%, compared to heptanes which produce a thermal efficiency of 25.2% and a CoV IMEP of 5.85%. The result of increased thermal efficiency and decreased CoV IMEP strongly support the conclusion that autoignition events are the driving force behind low octane rating combustion in dry EGR.

Decreasing the oxygen concentration of the EGR runs permitted the engine to operate at higher CRs, produce a higher number of autoignition events, and reach higher thermal efficiency. Conversely, the reduced oxygen concentration corresponded with decreasing combustion efficiency and increasing CoV IMEP, but at low oxygen concentrations the CoV IMEP decreased with increasing CR. Wet EGR was limited to low CRs due to its elevated intake temperatures, and without the ability to reach high CRs the CoV IMEP increased quickly as the oxygen concentration was decreased. Dry EGR was able to operate at much higher CRs than wet EGR due to its lower intake temperature and higher specific heat, and as such CoV IMEP was kept low for most cases. At the lowest oxygen concentration of 22.8% the CoV IMEP was higher than desired, but fell consistently as the CR was increased. Ultimately the engine CR limit of 17 was reached prior to reaching a point of uncontrollable knock, and thus it is theorized that reasonable CoV IMEP and higher thermal efficiency could be achieved.

Combustion efficiency was low for all cases, and decreased strongly with decreased O_2 concentration. In addition, the combustion efficiency continued to decrease as the CR was increased, representing a significant source of thermal efficiency loss and a major cleanup concern at the lowest oxygen concentrations.

12.1 Conclusions

In this thesis, it has been shown that dry EGR does have significantly higher knock resistance than air, allowing operation at higher CRs which can ultimately produce higher thermal efficiencies than air operation. When operation is limited by engine configuration rather than knocking the performance of dry EGR is very low relative to air, roughly proportional to the decrease in theoretical thermal efficiency due to the decrease in the ratio of specific heats. Therefore, in order to take advantage of the improved knock resistance it is necessary to operate in a region with a high enough CR and low enough oxygen concentration that minor autoignition events are common. It is easy to reach this operating range with a low octane fuel, and, with high enough CR, such combustion could be possible with fuels such as methane, allowing dry EGR to produce higher thermal efficeincy than methane-in-air. However, the very high autoignition temperature of methane would require very high in-cylinder temperatures which would produce significant wall heat losses. The minimum oxygen concentration is limited by the end of combustion HR profile, which becomes increasingly elongated as the oxygen concentration is reduced. Therefore, it is likely that if a high enough CR could be reached a local maximum thermal efficiency with respect to oxygen concentration would exist regardless of the fuel.

Wet EGR produces similar trends as dry EGR, but cannot attain the high CRs which dry EGR operated at due to the elevated intake temperature required to prevent water condensation. Ultimately, despite the chemical and thermal advantages of water compared to CO_2 in regards to laminar flame speeds, wet EGR is not a reasonable choice when operating in an IC engine. Despite its limitations in an IC engine, wet EGR has several advantages which should be carefully considered in applications where high initial temperatures are not propagated negatively.

The work presented in this thesis has demonstrated that under proper operating conditions the disadvantage of a triatomic working fluid can be overcome. The ability of dry EGR to produce higher thermal efficiency than air when combusting low octane fuel makes it clear that under certain circumstances (i.e. carbon capture is necessary and low-grade fuel is plentiful), oxycombustion in an SI engine is a competitive technology. The advantages were clearly demonstrated when operating with low octane fuel, but more research is needed to determine if a similar gain could be made with high octane fuel. In conclusion, this thesis has discovered many interesting aspects and limitations of oxycombustion in an SI engine, and provided a foundation upon which future research can be based.

Chapter 13

Division of Labor

This thesis represents a great deal of labor, ideas, discussion, and dedication. The work would not have been possible without the guidance and assistance of many individuals all working towards a common goal.

The vision and proposal which originated the experiment came from Professor Robert Cattolica and Dr. Reinhard Seiser of UC San Diego. They successfully applied for and were awarded an EISG grant as part of the PIER program which funded the assembly and initial testing of the experimental setup in Professor Robert Dibble's lab in UC Berkeley. Dr. Seiser and I designed and built the entire EGR loop from intake valves to exhaust valves, going through several iterations. The CFR engine, around which the experiment was based, was installed in Hesse Hall on the UC Berkeley campus around 1960, long before any of the current staff members became employed.

Similarly, the Horiba emissions analyzer has been part of the work group for many years, and was not constructed as part of this experiment. All piping and dilution systems related to the testing of the EGR intake and exhaust streams were designed and built by myself with the assistance of Dr. Seiser.

All data acquisition, controls, and data recording systems relating to the EGR system and emissions testing were designed and built in labview by me. The acquisition and recording of in-cylinder and intake-manifold pressures was achieved using a labview program written by Dr. Nick Killingsworth for a previous experiment. Real-time predictions of knock-intensity were built into the pressure acquisition system, and were designed and coded by former international visiting students Wolfgang Hable and Philipp Tschann.

Engine runs required a minimum of two operators at all times. I was always one of the operators, with Dr. Seiser being heavily involved during the first year of running and always being present for wet EGR testing, and Dr. Kozarac being present for the majority of the final year of testing.

I performed all of the data analysis from all experiments. A modified version of Dr. Darko Kozarac's heat release code written in Matlab was used to determine heat release rates as well as IMEP and CoV IMEP values for all run cases. In addition, I wrote codes in the Fortran based software Igor Pro which similarly analyzed heat release, IMEP and CoV

IMEP for individual test points and traces. I also wrote a code to determine knock intensity in Igor Pro which was based on the knock theory presented in the thesis' of Wolfgang Hable and Philipp Tschann. Dr. Kozarac similarly produced a Matlab code to determine knock-intensity, and the two could be used interchangeably.

Based on the measured intake compositions and EGR fractions, Professor J.Y. Chen computed the predicted flame speed and modeling results.

Bibliography

Andreas Wimmer, Josef Glaser (2002). *Indizieren am Verbrennungsmotor : Anwenderhandbuch*. Austria: AVL List Gmbh.

Bilger, Robert W. and Zhijun Wu (2009). "Carbon Capture for Automobiles Using Internal Combustion Rankine Cycle Engines". In: *Journal of Engineering for Gas Turbines and Power* 131.3, 034502, p. 034502. DOI: 10.1115/1.3077657.

Boer, P.C.T. de and J.-F. Hulet (1980). "Performance of a hydrogen-oxygen-noble gas engine". In: *International Journal of Hydrogen Energy* 5.4, pp. 439 –452. ISSN: 0360-3199. DOI: 10.1016/0360-3199(80)90024-5.

Brecq, Guillaume, Jrme Bellettre, and Mohand Tazerout (2003). "A new indicator for knock detection in gas SI engines". In: *International Journal of Thermal Sciences* 42.5, pp. 523 –532. ISSN: 1290-0729. DOI: 10.1016/S1290-0729(02)00052-2.

Correa, Sanjay M. (1993). "A Review of NOx Formation Under Gas-Turbine Combustion Conditions". In: *Combustion Science and Technology* 87.1-6, pp. 329–362. DOI: 10.1080/00102209208947221. eprint: http://www.tandfonline.com/doi/pdf/10.1080/00102209208947221.

Damen, Kay et al. (2006). "A Comparison of Electricity and Hydrogen Production Systems with CO_2 Capture and Storage. Part A: Review and Selection of Promising Conversion and Capture Technologies". In: *Progress in Energy and Combustion Science* 32.2, pp. 215 –246. ISSN: 0360-1285. DOI: 10.1016/j.pecs.2005.11.005.

Das, Apurba K., Kamal Kumar, and Chih-Jen Sung (2011). "Laminar Flame Speeds of Moist Syngas Mixtures". In: *Combustion and Flame* 158.2, pp. 345 –353. ISSN: 0010-2180. DOI: 10.1016/j.combustflame.2010.09.004.

Davis, Scott G. et al. (2005). "An optimized kinetic model of H2/CO combustion". In: *Proceedings of the Combustion Institute* 30.1, pp. 1283 –1292. ISSN: 1540-7489. DOI: 10.1016/j.proci.2004.08.252.

Flower, David and Jay Sanjayan (2007). "Green House Gas Emissions Due to Concrete Manufacture". In: *The International Journal of Life Cycle Assessment* 12 (5). 10.1065/lca2007.05.327, pp. 282–288. ISSN: 0948-3349.

Gielen, Dolf (2003). "CO_2 Removal in the Iron and Steel Industry". In: *Energy Conversion and Management* 44.7, pp. 1027 –1037. ISSN: 0196-8904. DOI: 10.1016/S0196-8904(02)00111-5.

Grunwald, Reinhard (2009). *GREENHOUSE GAS BURY IT INTO OBLIVION: OPTIONS AND RISKS OF CO2 CAPTURE AND STORAGE*. Tech. rep. 2. http://www.tab.fzk.de/. Berlin, Germany: Institute for Technology Assessment and Systems Analysis.

Heddle, Gemma, Howard Herzog, and Michael Klett (2003). *The Economics of CO_2 Storage*. Report MIT LFEE 2003-003 RP. Cambridge, MA: MIT Laboratory for Energy and the Environmnet.

Herbst, Julia et al. (2011). *Kinetic Characterization of Combustion in CO2 Atmosphere*. Poster. Part of the BIGCO2 project.

Heywood, John B. (1988). *Internal Combustion Engine Fundamentals*. New York, NY: McGraw-Hill.

IEA (2008). *World Energy Outlook*. International Energy Association.

Ikegami, M, K Miwa, and M Shioji (1982). "A study of hydrogen fuelled compression ignition engines". In: *International Journal of Hydrogen Energy* 7.4, pp. 341 –353. ISSN: 0360-3199. DOI: 10.1016/0360-3199(82)90127-6.

Kanniche, Mohamed et al. (2010). "Pre-Combustion, Post-Combustion and Oxy-Combustion in Thermal Power Plant for CO_2 Capture". In: *Applied Thermal Engineering* 30.1, pp. 53 –62. ISSN: 1359-4311. DOI: 10.1016/j.applthermaleng.2009.05.005.

Killingsworth, Nick J. et al. (2011). "Increased Efficiency in SI Engine with Air Replaced by Oxygen in Argon Mixture". In: *Proceedings of the Combustion Institute* 33.2, pp. 3141 –3149. ISSN: 1540-7489. DOI: 10.1016/j.proci.2010.07.035.

Konnov, A.A. (2009). "Implementation of the NCN pathway of prompt-NO formation in the detailed reaction mechanism". In: *Combustion and Flame* 156.11, pp. 2093 –2105. ISSN: 0010-2180. DOI: 10.1016/j.combustflame.2009.03.016.

Laumann, E. A. and R. K. Reynolds (1978). "Hydrogen-fueled Engine". Patent US 4,112,875 (US).

Liu, Fengsham, Hongsheng Guo, and Gregory J. Smallwood (2003). "The Chemical Effect of CO_2 Replacement of N_2 in Air on the Burning Velocity of CH_4 and H_2 Premixed Flames". In: *Combustion and Flame* 133.4, pp. 495 –497. ISSN: 0010-2180. DOI: 10.1016/S0010-2180(03)00019-1.

Mahalec, Ivan, Zoran Lulic, and Klaudio Skok (2001). "Mechanical Efficiency of Reciprocating Internal Combustion Engines". In: *Innovative Automotive Technology* IAT'01.

Matthews, H.D. and K. Caldeira (2008). "Stabilizing climate requires near-zero emissions". In: *GEOPHYSICAL RESEARCH LETTERS* 35.4, p. L04705. DOI: DOI10.1029/2007GL032388.

Mazas, A. N., D. A. Lacoste, and T. Schuller (2010). "Experimental and Numerical Investigation on the Laminar Flame Speed of CH_4/O_2 Mixtures Diluted with CO_2 and H_2O". In: *ASME Turbo Expo 2010* 30.GT2010-22512.

Metz, Ben et al. (2005). *Carbon Dioxide Capture and Storage*. Special report 1. Cambridge, MA: Intergovernmental Panel on Climate Change.

Miller, James A. and Craig T. Bowman (1989). "Mechanism and modeling of nitrogen chemistry in combustion". In: *Progress in Energy and Combustion Science* 15.4, pp. 287 –338. ISSN: 0360-1285. DOI: 10.1016/0360-1285(89)90017-8.

Quintella, Cristina M. et al. (2011). "CO2 capture technologies: An overview with technology assessment based on patents and articles". In: *Energy Procedia* 4.0. ¡ce:title¿10th International Conference on Greenhouse Gas Control Technologies¡/ce:title¿, pp. 2050 –2057. ISSN: 1876-6102. DOI: 10.1016/j.egypro.2011.02.087.

Revelle, Roger and Hans E. Suess (1957). "Carbon Dioxide Exchange Between Atmosphere and Ocean and the Question of an Increase of Atmospheric CO2 during the Past Decades". In: *Tellus* 9.1, pp. 18–27. ISSN: 2153-3490. DOI: 10.1111/j.2153-3490.1957.tb01849.x.

Richards, G. A., K. H. Casleton, and B. T. Chorpening (2005). "CO_2 and H_2O Diluted Oxy-Fuel Combustion for Zero-Emission Power". In: *Proceedings of the Institution of Mechanical Engineers, Part A: Journal of Power and Energy* 219.2, pp. 121–126. DOI: 10.1243/095765005X5990. eprint: http://pia.sagepub.com/content/219/2/121.full.pdf+html.

Salt, T., D. R. Tree, and C. Kim (2012). "Oxygen Enhanced Exhaust Gas Recirculation for Compression Ignition Engines". In: *Journal of Engineering for Gas Turbines and Power* 134.3, 032801, p. 032801. DOI: 10.1115/1.4005114.

Sanz, Wolfgang et al. (2008). "Qualitative and Quantitative Comparison of Two Promising Oxy-Fuel Power Cycles for CO_2 Capture". In: *Journal of Engineering for Gas Turbines and Power* 130.3, 031702, p. 031702. DOI: 10.1115/1.2800350.

Savitzky, Abraham. and Marcel J. E. Golay (1964). "Smoothing and Differentiation of Data by Simplified Least Squares Procedures." In: *Analytical Chemistry* 36.8, pp. 1627–1639. DOI: 10.1021/ac60214a047. eprint: http://pubs.acs.org/doi/pdf/10.1021/ac60214a047.

Scheffknecht, Gnter et al. (2011). "Oxy-Fuel Coal Combustion–A Review of the Current State-of-the-Art". In: *International Journal of Greenhouse Gas Control* 5, Supplement 1.0, S16 –S35. ISSN: 1750-5836. DOI: 10.1016/j.ijggc.2011.05.020.

Schmittner, Andreas et al. (2008). "Future changes in climate, ocean circulation, ecosystems, and biogeochemical cycling simulated for a business-as-usual CO2 emission scenario until year 4000 AD". In: *Global Biogeochem* 22.GB1013. DOI: doi:10.1029/2007GB002953.

Scholl, D. et al. (1998). "The Volume Acoustic Modes of Spark-Ignited Internal Combustion Chambers". In: *SAE Technical Paper* 980893. DOI: 10.4271/980893.

Seiser, R. and K. Seshadri (2005). "The Influence of Water on Extinction and Ignition of Hydrogen and Methane Flames". In: *Proceedings of the Combustion Institute* 30.1, pp. 407 –414. ISSN: 1540-7489. DOI: 10.1016/j.proci.2004.08.220.

Solomon, Susan et al. (2009). "Irreversible climate change due to carbon dioxide emissions". In: *Proceedings of the National Academy of Sciences* 106.6, pp. 1704–1709. DOI: 10.1073/pnas.0812721106. eprint: http://www.pnas.org/content/106/6/1704.full.pdf+html.

Tschann, Philipp (2009). "Emission and Performance Studies of Alternative Fuels". MS Thesis. Austria: Graz University of Technology.

Walton, S.M. et al. (2007). "An Experimental Investigation of the Ignition Properties of Hydrogen and Carbon Monoxide Mixtures for Syngas Turbine Applications". In: *Pro-*

ceedings of the Combustion Institute 31.2, pp. 3147 –3154. ISSN: 1540-7489. DOI: 10.1016/j.proci.2006.08.059.

Warnatz, J., U. Maas, and R. W. Dibble (2006). *Combustion - Physical and Chemical Fundamentals, Modeling and Simulation, Experiments, Pollutant Formation*. Springer.

Wei, Haiqiao et al. (2012). "Gasoline engine exhaust gas recirculation A review". In: *Applied Energy* 99.0, pp. 534 –544. ISSN: 0306-2619. DOI: 10.1016/j.apenergy.2012.05.011.

Woschni, G. (1967). "A Universally Applicable Equation for the Instantaneous Heat Transfer Coefficient in the Internal Combustion Engine". In: *SAE* 76.670931, p. 176. DOI: 10.4271/670931.

Yossefi, D. et al. (1995). "Combustion of Methane and Ethane with CO_2 Replacing N_2 as a Diluent. Modelling of Combined Effects of Detailed Chemical Kinetics and Thermal Properties on the Early Stages of Combustion". In: *Fuel* 74.7, pp. 1061 –1071. ISSN: 0016-2361. DOI: 10.1016/0016-2361(95)00048-A.

Zhu, D.L., F.N. Egolfopoulos, and C.K. Law (1989). "Experimental and Numerical Determination of Laminar Flame Speeds of Methane/(Ar, N_2, CO_2)-Air Mixtures as Function of Stoichiometry, Pressure, and Flame Temperature". In: *Symposium (International) on Combustion* 22.1, pp. 1537 –1545. ISSN: 0082-0784. DOI: 10.1016/S0082-0784(89)80164-X.

Appendix A

Heat Release Computation

```
function HRR(Pressure, ST, CR)

wave Pressure
variable CR, ST
variable O2,N2,CO2,H2O,CH4,HEP,OCT,H2,CO


// enter volume fraction of intake
O2 = 0.21
N2 = 0.79
CO2 = 0.00
H2O = 0
// enter flow rate of fuel in kg/s
CH4 = 0
HEP = 0.00018884
OCT = 0
H2 = 0
CO = 0

variable frac_blow_by
frac_blow_by = 0.05

make/O/N=9 compo_in

compo_in[x2pnt(compo_in,0)] = O2
compo_in[x2pnt(compo_in,1)] = N2
compo_in[x2pnt(compo_in,2)] = CO2
```

```
compo_in[x2pnt(compo_in,3)] = H2O
compo_in[x2pnt(compo_in,4)] = CH4
compo_in[x2pnt(compo_in,5)] = HEP
compo_in[x2pnt(compo_in,6)] = OCT
compo_in[x2pnt(compo_in,7)] = H2
compo_in[x2pnt(compo_in,8)] = CO

//print compo_in

init_vol_and_liq_fuel(compo_in)

variable/G cylinder_mass, M, M_resid, R, R_resid
//print cylinder_mass

variable thetaIVC,thetaIVO,thetaEVC,thetaEVO,thetaBBstart,
        thetaBBend, thetaSOC, thetaEOC, jj
thetaIVC = -128          // CAD corresponding to intake valve closure
thetaEVO = 180-50        // CAD corresponding to exhaust valve opening
thetaIVO = 360-15        // CAD corresponding to intake valve opening
thetaEVC = -360+15       // CAD corresponding to exhaust valve closure
thetaBBstart=-75;        // CAD corresponding to start of blow-by
thetaBBend=75;           // CAD corresponding to end of blow-by
thetaSOC = ST            // CAD corresponding to start of combustion
                         (defined by spark-timing)
thetaEOC = ST +90        // CAD corresponding to engine of combustion
                         (defined as 90 degrees after SOC)
jj = 0

variable idxIVC, idxEVO,idxIVO,idxEVC,idxBBstart,
        idxBBend, idxSOC, idxEOC

findvalue/T=0.06 /V=(thetaIVC) CAD
if (v_value == -1)
print ("Out of range 1")
else
idxIVC = v_value
endif
findvalue/T=0.06 /V=(thetaEVO) CAD
if (v_value == -1)
print ("Out of range 2")
else
idxEVO = v_value
```

```
endif
findvalue/T=0.06 /V=(thetaIVO) CAD
if (v_value == -1)
print ("Out of range 3")
else
idxIVO = v_value
endif
findvalue/T=0.06 /V=(thetaEVC) CAD
if (v_value == -1)
//print ("Out of range 4")
//print thetaEVC
else
idxEVC = v_value
endif
findvalue/T=0.06 /V=(thetaBBstart) CAD
if (v_value == -1)
print ("Out of range 5")
else
idxBBstart = v_value
endif
findvalue/T=0.06 /V=(thetaBBend) CAD
if (v_value == -1)
print ("Out of range 6")
else
idxBBend = v_value
endif
findvalue/T=0.06 /V=(thetaSOC) CAD
if (v_value == -1)
print ("Out of range 7")
else
idxSOC = v_value
endif
findvalue/T=0.06 /V=(thetaEOC) CAD
if (v_value == -1)
print ("Out of range 8")
else
idxEOC = v_value
endif

//

do
```

```
// create a wave of the mass in the cylinder throughout the charge,
        including blow-by losses
make/O/N=((idxEVO-idxIVC)+1) Mass, MassFrcBrnd,
        Charge_Mass_Frac, CAD_cycle, P_cycle

//print "a"

variable i
wave CAD, compo_mass_IVC, compo_mass_r
Mass = cylinder_mass
for (i=idxIVC;i<=idxEVO;i+=1)
        CAD_cycle[x2pnt(CAD_cycle,i-idxIVC)] = CAD(i)
        P_cycle[x2pnt(P_cycle,i-idxIVC)] = Pressure(i)*1e5
endfor

for (i=idxBBstart;i<=idxBBend;i+=1)
        Mass[x2pnt(Mass,i)] = cylinder_mass - cylinder_mass*
           frac_blow_by*((i-idxBBstart)/(idxBBend-idxBBstart))
endfor

for (i=idxBBend;i<=idxEVO;i+=1)
        Mass[x2pnt(Mass,i)] = cylinder_mass -
        cylinder_mass*frac_blow_by
endfor

Vol(CAD_cycle,CR)
dVdtheta(CAD_cycle, CR)
make/O/N=((thetaEVO-thetaIVC)*10+1) xO2, xN2, xCO2,
        xH2O, xCH4, xHEP, xOCT, xH2, xCO, M_combus, R_combus

//print "b"


xO2 = compo_mass_IVC(0)
xN2 = compo_mass_IVC(1)
xCO2 = compo_mass_IVC(2)
xH2O = compo_mass_IVC(3)
xCH4 = compo_mass_IVC(4)
xHEP = compo_mass_IVC(5)
xOCT = compo_mass_IVC(6)
xH2 = compo_mass_IVC(7)
```

```
xCO = compo_mass_IVC(8)
M_combus = M
R_combus = R
//////  Burn fraction from Wiebe function m=3
for (i=idxSOC;i<=idxEOC;i+=1)
        MassFrcBrnd[x2pnt(MassFrcBrnd,i)] = 1- exp(-6.9*((CAD(i)-
                        CAD(idxSOC))/(CAD(idxEOC)-CAD(idxSOC)))^3)
        M_combus[x2pnt(M_combus,i)] = M*(1-MassFrcBrnd(i)) +
                                        M_resid*(MassFrcBrnd(i))
        R_combus[x2pnt(R_combus,i)] = R*(1-MassFrcBrnd(i)) +
                                        R_resid*(MassFrcBrnd(i))
        xO2[x2pnt(xO2,i)] = compo_mass_IVC(0)*(1-MassFrcBrnd(i)) +
                                compo_mass_r(0)*(MassFrcBrnd(i))
        xN2[x2pnt(xN2,i)] = compo_mass_IVC(1)*(1-MassFrcBrnd(i)) +
                                compo_mass_r(1)*(MassFrcBrnd(i))
        xCO2[x2pnt(xCO2,i)] = compo_mass_IVC(2)*(1-MassFrcBrnd(i)) +
                                compo_mass_r(2)*(MassFrcBrnd(i))
        xH2O[x2pnt(xH2O,i)] = compo_mass_IVC(3)*(1-MassFrcBrnd(i)) +
                                compo_mass_r(3)*(MassFrcBrnd(i))
        xHEP[x2pnt(xHEP,i)] = compo_mass_IVC(5)*(1-MassFrcBrnd(i)) +
                                compo_mass_r(5)*(MassFrcBrnd(i))
endfor
//print "c"
for (i=idxEOC;i<=idxEVO;i+=1)
        MassFrcBrnd[x2pnt(MassFrcBrnd,i)] = 1
        M_combus[x2pnt(M_combus,i)] = M_resid
        R_combus[x2pnt(R_combus,i)] = R_resid
        xO2[x2pnt(xO2,i)] = compo_mass_r(0)
        xN2[x2pnt(xN2,i)] = compo_mass_r(1)
        xCO2[x2pnt(xCO2,i)] = compo_mass_r(2)
        xH2O[x2pnt(xH2O,i)] = compo_mass_r(3)
        xHEP[x2pnt(xHEP,i)] = compo_mass_r(5)
endfor

//print "d"


make/O/N=((thetaEVO-thetaIVC)*10+1) Temp_Cyl, dT_dtheta_raw,
                dT_dtheta_smth, dMass_dtheta, dP_dtheta
wave Volume_Proc

Temp_Cyl = P_cycle*Volume_Proc/(R_combus*Mass);
```

```
variable dtheta
dtheta = CAD(111)-CAD(110)
for (i=1;i<=numpnts(Temp_Cyl);i+=1)
        dT_dtheta_raw[x2pnt(dT_dtheta_raw,i)] =
                        (Temp_Cyl(i)-Temp_Cyl(i-1))/dtheta
        dMass_dtheta[x2pnt(dMass_dtheta,i)] =
                        (Mass(i)-Mass(i-1))/dtheta
        dP_dtheta[x2pnt(dP_dtheta,i)] =
                        (P_cycle(i)-P_cycle(i-1))/dtheta
endfor

//print "e"


Duplicate/O dT_dtheta_raw,dT_dtheta_smth;DelayUpdate
Smooth/S=2 51, dT_dtheta_smth
Smooth/S=2 51, dT_dtheta_smth

Duplicate/O dP_dtheta,dP_dtheta_smth;DelayUpdate
Smooth/S=2 51, dP_dtheta_smth
Smooth/S=2 51, dP_dtheta_smth

//print "f"

//print numpnts(Temp_Cyl)
//print numpnts(xO2)
variable/G Cp_var,Cv_var,gamma_mix_var
variable ii
make/O/N=(numpnts(Temp_Cyl)) Cp,Cv, gamma_mix

for (ii=0;ii<=numpnts(Temp_Cyl);ii+=1)
        cp_cv_gamma(Temp_Cyl(ii),xO2(ii),xN2(ii),xCO2(ii),xH2O(ii),
                        xCH4(ii),xHEP(ii),xOCT(ii),xH2(ii),xCO(ii))

        Cp[x2pnt(Cp,ii)] = Cp_var
        Cv[x2pnt(Cv,ii)] = Cv_var*100
        gamma_mix[x2pnt(gamma_mix,ii)] = gamma_mix_var
endfor

//print "g"
```

```
make/O/N=(numpnts(Mass)) ROHR, SpecificVolume
wave dV_dTheta

for (i=0;i<=numpnts(ROHR);i+=1)
        SpecificVolume[x2pnt(SpecificVolume,i)] = Volume_Proc(i)/Mass(i)
//      ROHR[x2pnt(ROHR,i)]   = dMass_dtheta(i)
//      ROHR[x2pnt(ROHR,i)]   = dT_dtheta_smth(i)
        ROHR[x2pnt(ROHR,i)]   = Mass(i)*Cv(i)*dT_dtheta_smth(i) +
          P_cycle(i)*dV_dTheta(i) + SpecificVolume(i)*
          P_cycle(i)*dMass_dtheta(i)
 //         + devWallHeatDeg(idxIVC:idxEVO)'...
endfor

Duplicate/O ROHR,ROHR_smth
Smooth/S=2 51, ROHR_smth
//Smooth/S=2 51, dP_dtheta_smth

//print "h"

////print idxIVC


make/O/N=(numpnts(ROHR)) CumROHR
CumROHR = 0
for (i=1;i<=numpnts(ROHR);i+=1)
        CumROHR[x2pnt(CumROHR,i)] =CumROHR(i-1)+
                (ROHR_smth(i)+ROHR_smth(i-1))*(dtheta)/2;
endfor



wavestats/Q CumROHR

//CumROHR_min = wavemin(CumROHR)
variable idxEOC_old, idxSOC_old
idxEOC_old =  idxEOC
idxSOC_old = idxSOC

for (i=V_minloc;i<=V_maxloc;i+=1)
        if (CumROHR(i) >= v_max*0.99)
                idxEOC=i;
//              print "update1"
```

```
                    break
            endif
endfor
//print idxEOC
//print V_maxloc

//print "IVC"
for (i=V_minloc;i<=V_maxloc;i+=1)
            if (CumROHR(i) < v_min*1.01^(abs(v_min)/v_min))
                    idxSOC=i;
//                  print "update"
                    //break
            endif
endfor


jj=jj+1;
print jj
//print (idxEOC - idxEOC_old)
while (abs(idxEOC - idxEOC_old) > 5 && jj<=5)
print "done"
print CAD_cycle(idxSOC)
print CAD_cycle(idxEOC)


//display Temp_cyl
//Display ROHR vs CAD_cycle
//Display CumROHR vs CAD_cycle
end
```